Ultrafast Photoexcited Carrier Dynamics in Two-Dimensional Molybdenum Disulfide

Ву

Durga Prasad Khatua PHYS03201704013

Raja Ramanna Centre for Advanced Technology, Indore

A thesis submitted to the

Board of Studies in Physical Sciences

In partial fulfillment of requirements

for the Degree of

DOCTOR OF PHILOSOPHY

of

HOMI BHABHA NATIONAL INSTITUTE



April, 2022

Homi Bhabha National Institute*

Recommendations of the Viva Voce Committee

As members of the viva voce Committee, we certify that we have read the dissertation prepared by Durga Prasad Khatua entitled "Ultrafast Photoexcited Carrier Dynamics in Two-Dimensional Molybdenum Disulfide" and recommend that it may be accepted as fulfilling the thesis requirement for the award of Degree of Doctor of Philosophy.

Chairman: Prof. Tarun Kumar Sharma	TE Dt. 12.08.2022
Guide/Convener: Dr J. Jayabalan	1 Jyu Dt. 12.08.2022
Examiner: Dr Rajeev N Kini	Dt. 12.08.2022
Member 1: Dr. S. M. Gupta	Dt. 12.08.2022
Member 2: Dr. Pankaj Misra	Microin. Dt. 12.08.2022
Member 3: Dr. S. Satapathy	Dt. 12.08.2022
External Expert Member: Dr. Rajesh Kumar	Dt. 12.08.2022

Final approval and acceptance of this thesis is contingent upon the candidate's submission of the final copies of the thesis to HBNI.

I hereby certify that I have read this thesis prepared under my direction and recommend that it may be accepted as fulfilling the thesis requirement.

Date: 12-08-2022

Place: Indore, INDIA

Janature

Guide

^{*}This page is to be included only for final submission after successful completion of viva voce.

STATEMENT BY AUTHOR

This dissertation has been submitted in partial fulfillment of requirements for an advanced degree at Homi Bhabha National Institute (HBNI) and is deposited in the library to be made available to borrowers under the rules of the HBNI.

Brief quotations from this dissertation are allowable without special permission, provided that accurate acknowledgment of the source is made. Requests for permission for extended quotation from or reproduction of this manuscript in whole or in part may be granted by the Competent Authority of HBNI when in his or her judgment, the proposed use of the material is in the interests of scholarship. In all other instances, however, permission must be obtained from the author.

DURGA PRAJAD KHATUA.

Name & Signature of the student

DECLARATION

I, hereby declare that the investigation presented in the thesis has been carried out by me. The work is original and has not been submitted earlier as a whole or in part for a degree/diploma at this or any other Institution/University.

DURGA PRASAD KHATUA.

Name & Signature of the student

List of Publications Arising from the Thesis

Journals

- 1. "Filtering noise in time and frequency domain for ultrafast pump–probe performed using low repetition rate lasers", **Durga Prasad Khatua**, Sabina Gurung, Asha Singh, Salahuddin Khan, Tarun Kumar Sharma, and J. Jayabalan, Review of Scientific Instruments, 91, 103901 (2020).
- 2. "Ultrafast carrier dynamics in a monolayer MoS₂ at carrier densities well above Mott density", **Durga Prasad Khatua**, Asha Singh, Sabina Gurung, Salahuddin Khan, Manushree Tanwar, Rajesh Kumar, and J. Jayabalan, Journal of Physics Condensed Matter, 34, 155401 (2022).
- 3. "A Comparative study of ultrafast carrier dynamics near A, B, and C-excitons in a monolayer MoS₂ at high excitation densities", **Durga Prasad Khatua**, Asha Singh, Sabina Gurung, Manushree Tanwar, Rajesh Kumar, and J. Jayabalan, Optical Materials, 126, 112224 (2022).
- 4. "Excitation density dependent carrier dynamics in a monolayer MoS₂: exciton dissociation, formation and bottlenecking", **Durga Prasad Khatua**, Asha Singh, Sabina Gurung, and J. Jayabalan, Micro and Nanostructures, 165, 207205 (2022).
- 5. "Pump fluence dependent carrier dynamics at the A-exciton of MoS₂: monolayer vs bulk", **Durga Prasad Khatua**, Asha Singh, Sabina Gurung, and J. Jayabalan, (To be submitted).

Conferences

- 1. "Carrier dynamics measurement on MoS₂ monolayers using ultrafast pump-probe spectroscopy", **Durga Prasad Khatua**, Asha Singh, Sabina Gurung, and J. Jayabalan, Ultrafast Sciences, IIT Bombay, November 7-9, 2019 (Poster presentation).
- 2. "Ultrafast carrier dynamics in a single MoS₂ monolayer flake at high excitation densities", **Durga Prasad Khatua**, Sabina Gurung, Asha Singh, Salahuddin Khan, and J. Jayabalan, 7th Theme Meeting on Ultrafast Science, UM-DAE Centre for Excellence in Basic Sciences, Mumbai, November 12-14, 2021 (Poster Presentation).
- 3. "A comparison of transient optical response of a monolayer MoS₂ near to its A, B, and C excitons", **Durga Prasad Khatua**, Sabina Gurung, Asha Singh, Salahuddin Khan, and J. Jayabalan, 65th DAE Solid State Physics Symposium, Bhabha Atomic Research Centre, Mumbai, India, December 15-19, 2021 (Poster Presentation) (Best poster award).

DURGA PRAJAD KHATUA. Name & Signature

of the student

To, my beloved parents,

Thank you for your endless love, sacrifices, prayers, and support.

This thesis is proudly dedicated to my parents.

Durga prasad Khatua

ACKNOWLEDGEMENTS

This thesis is a dream of my life that may not possible without the help of many people. It gives me tremendous pleasure to express my gratitude to each and every one of them.

First and foremost, I would like to express my gratitude to my guide Dr. J. Jayabalan who is always there for me for any type of help during my Ph.D. He provided me a great research environment in lab along with his passion for the science which motivated me a lot. His encouragement, advice, and support have been provided me a path for my personal and professional developments. I hope that I have grabbed some of his qualities for doing better science in future.

I am also very much grateful to Dr. P. D. Naik, Dean-HBNI for giving me the opportunity to work under the guidance of Dr. J. Jayabalan even after his voluntary retirement. I am deeply grateful to Ms. Asha Singh for her guidance, help, and suggestions during my Ph.D. work. Her guidance is very helpful during the development of setups, data analysis, and paper writing. I am extremely thankful to Dr. Salahuddin Khan and Mr. Saleem Khan for their help and suggestions during my Ph.D. work. I am also thankful to Mr. Vijay Singh Dawar for his support during the experimental works, specifically helping me in running the lasers and other instruments smoothly. I thank my senior Dr. Sabina Gurung for her constant support during my Ph.D. work even while she was busy at her post-Doctorate work abroad.

I am grateful to my section head Dr. Tarun Kumar Sharma for his constant support and suggestions in academic and administrative work. I am also very much thankful to the old and new doctoral committee members, Dr. Aparna Chakrabarty, Dr. A. K. Sinha, Dr. T. K. Sharma, Dr. M. K. Chattopadhyay, Dr. S. M. Gupta, Dr. S. Satapathy, Dr. P. Misra, and my external member Dr. Rajesh Kumar for their valuable suggestions throughout the annual progress report meetings. I am thankful to the old and new dean academic of HBNI-RRCAT and dean students

affair Dr. Arup Banerjee, Dr. S. R. Mishra, and Dr. C. P. Paul for their help. I acknowledge the support given by the Directors of RRCAT and also the financial support from RRCAT under the HBNI Ph.D. program. This acknowledgment would not be complete without mentioning my friends, juniors, and seniors in the hostel who gave me a collection of memories in this journey.

I express my deepest regards to my parents Mrs. Nandini Khatua and Mr. Balunkeswar Khatua for their unconditional love and support. I also thank my uncle Mr. Ramesh Chandra Khatua for his support while I am away from home. I thank to my aunty Mrs. Rama Khatua, my sisters Pramodini Khatua, Sarojini Khatua, Saudamini Khatua and my brothers, Bishnu Prasad Khatua and Swapneswar Khatua for their love and supports.

Durga Prasad Khatua

SUMMARY

Monolayer (ML) and bulk Molybdenum Disulfide (MoS₂) are very interesting materials for applications in valleytronics, spintronics, transistor, optoelectronics, and memory devices. Hence, it is important to study carrier dynamics in all the exciton states in ML and bulk MoS₂ to understand the carrier behaviors at different excitation conditions such as excitation and probing energy, excitation density, band structure, etc. Since A-exciton is the lowest excitonic transition energy, it has been studied rigorously to understand the carrier dynamics at this resonance energy for its application in future technologies. So, in this thesis work, carrier dynamics at the A-exciton transition energy is studied at the pump fluences where it is not understood well. For better understanding of the physical processes that happen in the material, pump fluence studies have been performed. Besides this, since ML MoS₂ possesses three excitons in the visible regime named A, B, and C, it is important to study the carrier behaviors at all these excitonic transition energies. Hence, pump fluence dependent carrier dynamics measurements at these exciton resonance energies are studied in the same excitation density range where it is not well studied. These carrier dynamics measurements are compared with each other and explanation for the different behaviors are given. Further, pump fluence dependent carrier dynamics of a bulk MoS₂ sample is studied at the A-exciton transition energy in the same pump fluence range. The findings from these studies are compared with that of the ML MoS₂ sample. All these measurements are performed in the pump fluence range 1.2 mJcm $^{-2}$ to 12.2 mJcm $^{-2}$ which corresponding to 6.6 imes 10^{13} cm $^{-2}$ to 6.7 imes 10^{14} cm^{-2} .

Moreover, since all these experiments are performed using a 35 fs Oscillator-Amplifier-OPA system operating at 1 kHz, the standard detection schemes that are used for a high-repetition rate laser will not work. Hence, a highly sensitive detection scheme is developed using the combination of boxcar and lock-in amplifier and demonstrated. A theoretical model also developed which gives same result as that

of the experimental results. Further, chopper frequency dependent measurements are carried out to find out the best chopping frequency for the transient measurements while working in a low-repetition rate laser.

Contents

L1	st of	Publica	ations	1V
A	cknov	wledgn	nents	vi
Sι	ımma	ary		viii
C	onten	ts		x
Li	st of	Figures	5	xii
Li	st of	Tables		xvii
A l	bbrev	iations	5	xviii
1	Intr	oductio	on	1
	1.1		fast Processes During Carrier Dynamics Measurements	. 5
		1.1.1	Thermalization of Photoexcited Carriers	. 8
		1.1.2	Exciton Formation	. 8
		1.1.3	Carrier Trapping into Defect States	
		1.1.4	Auger Scattering & Defect-assisted Auger Scattering	
		1.1.5	Exciton-Exciton Annihilation (EEA) and Defect-assisted EEA	
		1.1.6	Hot-Carrier Cooling	
	1.2		fast Modification of Optical Response of Materials	
		1.2.1	Band Filling and Band Bleaching	
		1.2.2	Bandgap Renormalization (BGR)	
	4.0	1.2.3	Exciton Peak Shift and it's Broadening	
	1.3		cations of Monolayer MoS_2	
	1.4	Organ	nization of the Thesis	. 19
2	Exp		tal Technique and Basic Characterization of 2D Samples	20
	2.1	-	al Characterization	
	2.2		ity Measurements	
	2.3		ion of Flakes and AFM Images	
	2.4	Sumn	nary	. 27
3	Aug	menta	tion of Experimental Setup	28

Contents xi

В	Cal	culation of Auger recombination rate	94
A	Cal	culation of Carrier Density Generated in the Sample	92
7	Cor	iclusions and Future Scope	88
	6.4	Summary	86
	6.3	Model and Explanation of the Processes	83
	6.2	Fluence Dependence of Peak $\Delta T/T$ and Time Constants	81
6	Con 6.1	nparison of Carrier Dynamics in Monolayer and Bulk MoS ₂ Transient Measurements near A-exciton	78 79
	J. T	Summary	//
	5.4	Summary	7 4 77
	5.2	Fluence Dependent Transient Transmission	74
	5.15.2	Photoexcitation Density	70 72
5	Two	nparison of Ultrafast Carrier Dynamics near A, B, and C-excitons in p-Dimensional MoS ₂	69
	4.2	Summary	68
		4.1.2 Transient Transmission of ML MoS ₂ in Full-Time Scale	62
		4.1.1 Transient Transmission of ML MoS ₂ within First 5 ps	56
	A-e : 4.1	xciton Transient Transmission near A-exciton	53 55
4		rafast Carrier Dynamics in a Two-Dimensional MoS ₂ Monolayer near	5 0
	3.5	Summary	51
	3.4	Pump-Probe Setup Developed for Transient Measurements in 2D MoS ₂	
		3.3.1 Experimental Details	38
	3.3	Low-Repetition Rate Laser System: Noises and High Sensitive Detection Technique	37
		Repetition Rate Laser	33
	3.2	Phase-Sensitive Detection Technique	31
	3.1	Transient Pump-Probe Setup	29

List of Figures

1.1	(a) Unit cell of ML MoS ₂ showing the prismatic structure where one	
	Mo-atom is sandwiched between two S-atoms. (<i>b</i>) Top view of a two-	
	dimensional crystal structure of ML MoS ₂ . (c) Electronic band struc-	
	ture of a ML MoS_2 near K and K' points of the Brillouin zone showing	
	band splitting. (d) Shows the hexagonal Brillouin zone of ML MoS ₂	4
1.2	Typical time line of various processes that occur in a material upon	
	photoexcitation. Note that, time line of all the processes depends on	
	excitation density and material	7
1.3	Photoexcitation density dependent ultrafast processes that happen in	
	a ML MoS ₂ that are dominant in the specific carrier density regime.	
	Note that, these processes depend on material, pump fluence, and	
	pump wavelengths	7
1.4	Exciton formation in (a) bulk semiconductor and (b) 2D semiconductor.	9
1.5	(a) The thermalization of carriers upon excitation by an ultrashort	
	pulse, (b) fast trapping of holes and electrons by fast-defect states,	
	and (c) slow capture of carriers by slow-defect states	10
1.6	(a) An electron or (b) a hole is captured by the defect states. In each,	
	three different capture processes are shown	11
1.7	Exciton-exciton annihilation in a ML MoS ₂ showing two excitons par-	
	ticipating in the recombination process. One exciton will recombine	
	and transfer its energy to another exciton taking the electron and hole	
	to higher excited states	12
1.8	(a) Band filling effect at the edge of the conduction band and valence	
	band due to photoexcitation. In this case, the original bandgap (E_g)	
	is lower than the new bandgap (E_g^{BF}). (b) The BGR effect at the band	
	edge when excitation density is high. In this case, $E_g > E_g^{BGR}$	14
2.1	(a) Absorbance spectrum of ML MoS ₂ sample recorded using a UV-	
2.1	Vis spectrometer and fitted with four Lorentzian peaks corresponding	
	to transition energy of A, B, C-excitons, and a higher energy transi-	
	tion peak. Green line represents the best fit to the absorbance spec-	
	trum and the magenta lines represent individual contributions. (b)	
		21
	The measured microscopic absorption spectrum of the flake used for transient measurements	2

List of Figures xiii

 2.3 AFM topography images of few monolayer flakes after being exposed to 672 nm femtosecond laser beam at different fluences: (a) before exposure, (b) exposure to 50 mJcm⁻² and (c) 100 mJcm⁻². Dotted ellipses show the regime where structural modifications were observed. 2.4 Damage threshold measurements of the ML MoS2 flake: (a) AFM line profile of the flake before and after exposure to 50 mJcm⁻², and (b) Raman scattering of the same flake before and after exposure to 50 mJcm⁻², pump fluence. 2.5 Optical image of (a) ML MoS2 flake and (b) multilayer MoS2 flake captured in a microscopic setup developed in the pump-probe setup. 2.6 AFM topographic image of (a) ML MoS2 flake and (b) multilayer MoS2 flake. These AFM scans are taken at one corner of the flakes. 2.7 (a) AFM line profile of the ML flake at one edge for the thickness measurement with the AFM topography of the flake in the inset and (b) Raman spectrum of the ML MoS2 flake used in the transient transmission measurement. 2.8 AFM line profile of the bulk MoS2 flake used in carrier dynamics studies for thickness measurement. 2.6 Schematic of a typical transient pump-probe setup. BS: Beam splitter, M: Mirror, P: Polarizer, L: Lens, S: Sample, PD: Photodetector, WP: Wave plate, and PC: Personal Computer. 3.2 Schematic of the detection portion of a typical transient reflectivity setup. 3.3 Schematic of a typical transient absorption setup with phase-sensitive detection scheme. BS: Beam splitter, M: Mirror, P: Polarizer, L: Lens, S: Sample, PD: Photodetector, WP: Wave plate, C: Chopper, LIA: Lockin amplifier, and PC: Personal Computer. 3.3 (a) Output voltage of a photodetector when only the probe beam is transmitting through the sample and under no pump condition. (b) Output voltage of a photodetector when both pump and probe are transmitting through the sample and under no pump condition. (b) Output voltage of a photodetector when both pump and probe are transmitt	2.2	Schematic of the microscopic absorption spectrometer setup developed for the measurement on samples smaller than 100 μ m. BS: Beam Splitter, C: CCD camera, L: Lens, M: Mirror, O: Objective, SM: Spec-	
to 672 nm femtosecond laser beam at different fluences: (a) before exposure, (b) exposure to 50 mJcm ⁻² and (c) 100 mJcm ⁻² . Dotted ellipses show the regime where structural modifications were observed. 23 2.4 Damage threshold measurements of the ML MoS ₂ flake: (a) AFM line profile of the flake before and after exposure to 50 mJcm ⁻² , and (b) Raman scattering of the same flake before and after exposure to 50 mJcm ⁻² pump fluence. 23 2.5 Optical image of (a) ML MoS ₂ flake and (b) multilayer MoS ₂ flake captured in a microscopic setup developed in the pump-probe setup. 25 flake. These AFM scans are taken at one corner of the flakes. 25 flake. These AFM scans are taken at one edge for the thickness measurement with the AFM topography of the flake in the inset and (b) Raman spectrum of the ML MoS ₂ flake used in the transient transmission measurement. 26 2.8 AFM line profile of the bulk MoS ₂ flakes used in carrier dynamics studies for thickness measurement. 26 3.1 Schematic of a typical transient pump-probe setup. BS: Beam splitter, M: Mirror, P: Polarizer, L: Lens, S: Sample, PD: Photodetector, WP: Wave plate, and PC: Personal Computer. 29 3.2 Schematic of the detection portion of a typical transient reflectivity setup. 30 3.3 Schematic of a typical transient absorption setup with phase-sensitive detection scheme. BS: Beam splitter, M: Mirror, P: Polarizer, L: Lens, S: Sample, PD: Photodetector, WP: Wave plate, C: Chopper, LIA: Lockin amplifier, and PC: Personal Computer. 33 3.4 (a) Output voltage of a photodetector when only the probe beam is transmitting through the sample. (c) Output voltage of a 1 kHz pulsed laser system and triggering of the boxcar showing the gate voltage where the transient signal will be measured. 34 3.5 Schematic of the pump-probe setup along with the high sensitive detection system which combines the advantages both of boxcar and lock-in amplifier. M: Mirror, BS: Beam Splitter, BBO:Beta Barium Bo-		trometer	22
 2.4 Damage threshold measurements of the ML MoS₂ flake: (a) AFM line profile of the flake before and after exposure to 50 mJcm⁻², and (b) Raman scattering of the same flake before and after exposure to 50 mJcm⁻² pump fluence. 2.5 Optical image of (a) ML MoS₂ flake and (b) multilayer MoS₂ flake captured in a microscopic setup developed in the pump-probe setup. 2.6 AFM topographic image of (a) ML MoS₂ flake and (b) multilayer MoS₂ flake. These AFM scans are taken at one corner of the flakes. 2.7 (a) AFM line profile of the ML flake at one edge for the thickness measurement with the AFM topography of the flake in the inset and (b) Raman spectrum of the ML MoS₂ flake used in the transient transmission measurement. 2.8 AFM line profile of the bulk MoS₂ flakes used in carrier dynamics studies for thickness measurement. 2.6 Schematic of a typical transient pump-probe setup. BS: Beam splitter, M: Mirror, P: Polarizer, L: Lens, S: Sample, PD: Photodetector, WP: Wave plate, and PC: Personal Computer. 2.9 Schematic of the detection portion of a typical transient reflectivity setup. 3.1 Schematic of a typical transient absorption setup with phase-sensitive detection scheme. BS: Beam splitter, M: Mirror, P: Polarizer, L: Lens, S: Sample, PD: Photodetector, WP: Wave plate, C: Chopper, LIA: Lockin amplifier, and PC: Personal Computer. 3.3 God profile of the sample and under no pump condition. (b) Output voltage of a photodetector when only the probe beam is transmitting through the sample and under no pump condition. (b) Output voltage of a photodetector when both pump and probe are transmitting through the sample. (c) Output voltage of a 1 kHz pulsed laser system and triggering of the boxcar showing the gate voltage where the transient signal will be measured. 3.5 Schematic of the pump-probe setup along with the high sensitive detection system which combines the advantages both of boxcar and lock-in amplifier. M: Mirror, BS: Beam Sp	2.3	to 672 nm femtosecond laser beam at different fluences: (a) before exposure, (b) exposure to 50 mJcm ⁻² and (c) 100 mJcm ⁻² . Dotted	23
 2.5 Optical image of (a) ML MoS2 flake and (b) multilayer MoS2 flake captured in a microscopic setup developed in the pump-probe setup. 2.6 AFM topographic image of (a) ML MoS2 flake and (b) multilayer MoS2 flake. These AFM scans are taken at one corner of the flakes. 2.7 (a) AFM line profile of the ML flake at one edge for the thickness measurement with the AFM topography of the flake in the inset and (b) Raman spectrum of the ML MoS2 flake used in the transient transmission measurement. 2.8 AFM line profile of the bulk MoS2 flakes used in carrier dynamics studies for thickness measurement. 2.8 AFM line profile of the bulk MoS2 flakes used in carrier dynamics studies for thickness measurement. 2.8 Schematic of a typical transient pump-probe setup. BS: Beam splitter, M: Mirror, P: Polarizer, L: Lens, S: Sample, PD: Photodetector, WP: Wave plate, and PC: Personal Computer. 2.9 Schematic of the detection portion of a typical transient reflectivity setup. 3.0 Schematic of a typical transient absorption setup with phase-sensitive detection scheme. BS: Beam splitter, M: Mirror, P: Polarizer, L: Lens, S: Sample, PD: Photodetector, WP: Wave plate, C: Chopper, LIA: Lockin amplifier, and PC: Personal Computer. 3.4 (a) Output voltage of a photodetector when only the probe beam is transmitting through the sample and under no pump condition. (b) Output voltage of a photodetector when both pump and probe are transmitting through the sample. (c) Output voltage of a 1 kHz pulsed laser system and triggering of the boxcar showing the gate voltage where the transient signal will be measured. 3.5 Schematic of the pump-probe setup along with the high sensitive detection system which combines the advantages both of boxcar and lock-in amplifier. M: Mirror, BS: Beam Splitter, BBO:Beta Barium Bo 	2.4	Damage threshold measurements of the ML MoS ₂ flake: (a) AFM line profile of the flake before and after exposure to 50 mJcm ⁻² , and (b) Raman scattering of the same flake before and after exposure to 50	23
 2.6 AFM topographic image of (a) ML MoS₂ flake and (b) multilayer MoS₂ flake. These AFM scans are taken at one corner of the flakes. 2.7 (a) AFM line profile of the ML flake at one edge for the thickness measurement with the AFM topography of the flake in the inset and (b) Raman spectrum of the ML MoS₂ flake used in the transient transmission measurement. 2.8 AFM line profile of the bulk MoS₂ flakes used in carrier dynamics studies for thickness measurement. 2.6 3.1 Schematic of a typical transient pump-probe setup. BS: Beam splitter, M: Mirror, P: Polarizer, L: Lens, S: Sample, PD: Photodetector, WP: Wave plate, and PC: Personal Computer. 2.9 Schematic of the detection portion of a typical transient reflectivity setup. 3.1 Schematic of a typical transient absorption setup with phase-sensitive detection scheme. BS: Beam splitter, M: Mirror, P: Polarizer, L: Lens, S: Sample, PD: Photodetector, WP: Wave plate, C: Chopper, LIA: Lockin amplifier, and PC: Personal Computer. 3.3 (a) Output voltage of a photodetector when only the probe beam is transmitting through the sample and under no pump condition. (b) Output voltage of a photodetector when both pump and probe are transmitting through the sample. (c) Output voltage of a 1 kHz pulsed laser system and triggering of the boxcar showing the gate voltage where the transient signal will be measured. 3.4 Schematic of the pump-probe setup along with the high sensitive detection system which combines the advantages both of boxcar and lock-in amplifier. M: Mirror, BS: Beam Splitter, BBO:Beta Barium Bo- 	2.5	Optical image of (a) ML MoS ₂ flake and (b) multilayer MoS ₂ flake	25
surement with the AFM topography of the flake in the inset and (b) Raman spectrum of the ML MoS₂ flake used in the transient transmission measurement	2.6		25
 2.8 AFM line profile of the bulk MoS2 flakes used in carrier dynamics studies for thickness measurement. 26 3.1 Schematic of a typical transient pump-probe setup. BS: Beam splitter, M: Mirror, P: Polarizer, L: Lens, S: Sample, PD: Photodetector, WP: Wave plate, and PC: Personal Computer. 3.2 Schematic of the detection portion of a typical transient reflectivity setup. 3.3 Schematic of a typical transient absorption setup with phase-sensitive detection scheme. BS: Beam splitter, M: Mirror, P: Polarizer, L: Lens, S: Sample, PD: Photodetector, WP: Wave plate, C: Chopper, LIA: Lockin amplifier, and PC: Personal Computer. 3.4 (a) Output voltage of a photodetector when only the probe beam is transmitting through the sample and under no pump condition. (b) Output voltage of a photodetector when both pump and probe are transmitting through the sample. (c) Output voltage of a 1 kHz pulsed laser system and triggering of the boxcar showing the gate voltage where the transient signal will be measured. 3.5 Schematic of the pump-probe setup along with the high sensitive detection system which combines the advantages both of boxcar and lock-in amplifier. M: Mirror, BS: Beam Splitter, BBO:Beta Barium Bo- 	2.7	surement with the AFM topography of the flake in the inset and (<i>b</i>) Raman spectrum of the ML MoS ₂ flake used in the transient transmis-	26
M: Mirror, P: Polarizer, L: Lens, S: Sample, PD: Photodetector, WP: Wave plate, and PC: Personal Computer	2.8	AFM line profile of the bulk MoS ₂ flakes used in carrier dynamics	26
 3.2 Schematic of the detection portion of a typical transient reflectivity setup	3.1	M: Mirror, P: Polarizer, L: Lens, S: Sample, PD: Photodetector, WP:	29
 3.3 Schematic of a typical transient absorption setup with phase-sensitive detection scheme. BS: Beam splitter, M: Mirror, P: Polarizer, L: Lens, S: Sample, PD: Photodetector, WP: Wave plate, C: Chopper, LIA: Lockin amplifier, and PC: Personal Computer. 3.4 (a) Output voltage of a photodetector when only the probe beam is transmitting through the sample and under no pump condition. (b) Output voltage of a photodetector when both pump and probe are transmitting through the sample. (c) Output voltage of a 1 kHz pulsed laser system and triggering of the boxcar showing the gate voltage where the transient signal will be measured. 3.5 Schematic of the pump-probe setup along with the high sensitive detection system which combines the advantages both of boxcar and lock-in amplifier. M: Mirror, BS: Beam Splitter, BBO:Beta Barium Bo- 	3.2	Schematic of the detection portion of a typical transient reflectivity	
 3.4 (a) Output voltage of a photodetector when only the probe beam is transmitting through the sample and under no pump condition. (b) Output voltage of a photodetector when both pump and probe are transmitting through the sample. (c) Output voltage of a 1 kHz pulsed laser system and triggering of the boxcar showing the gate voltage where the transient signal will be measured	3.3	Schematic of a typical transient absorption setup with phase-sensitive detection scheme. BS: Beam splitter, M: Mirror, P: Polarizer, L: Lens, S: Sample, PD: Photodetector, WP: Wave plate, C: Chopper, LIA: Lock-	
tection system which combines the advantages both of boxcar and lock-in amplifier. M: Mirror, BS: Beam Splitter, BBO:Beta Barium Bo-	3.4	(a) Output voltage of a photodetector when only the probe beam is transmitting through the sample and under no pump condition. (b) Output voltage of a photodetector when both pump and probe are transmitting through the sample. (c) Output voltage of a 1 kHz pulsed laser system and triggering of the boxcar showing the gate voltage	
	3.5	Schematic of the pump-probe setup along with the high sensitive detection system which combines the advantages both of boxcar and lock-in amplifier. M: Mirror, BS: Beam Splitter, BBO:Beta Barium Bo-	38

List of Figures xiv

3.6	Measured transient transmission signal of a Ag thin particulate film. (a) The output of PD_1 is detected by boxcar and the output of boxcar is then sensed with lock-in amplifier at chopper frequency, 405 Hz and (b) similar to (a) except that the fluctuation in the signal is further reduced by subtracting a reference probe signal (see the text for details).	40
3.7 3.8	Output voltage of boxcar when the gated laser pulse is measured The dependence of the fluctuations in the normalized signal measured at peak position in A-B configuration on the chopping frequencies around 333 Hz. The height of the rectangular box represents the S_D and the maximum and minimum signal values in the data set are	40 42
3.9	also shown as bar	45
	cies close to 333 Hz. The time in the horizontal axis at each chopper frequency is chosen such that there are 30 chopping cycles in view	46
3.10	Output voltage of the boxcar measured at chopper frequencies which are harmonics of 1 kHz. The time in the horizontal axis at each chopper frequency is chosen such that there are 30 chopping cycles in view.	47
3.11	The dependence of the fluctuations in the normalized signal measured at peak position in A-B configuration on the chopping frequencies which are factors of 1 kHz. The height of the rectangular box represents the S_D and the maximum and minimum signal values in	17
	the data set are also shown as bar	48
3.12	A typical transient absorption signal measured with 333 Hz chopping. Inset shows the same curve in log-log scale.	49
3.13	Schematic of the pump-probe setup developed for the transient measurements in the 2D MoS ₂ samples. BS: Beam Splitter, C: CCD camera, L: Lens, M: Mirror, O: Objective, PD: Photodiode, PM: Parabolic Mirror, and VF: Variable Filter.	50
4.1	Fluence dependent transient transmission signal of the selected ML MoS ₂ flake at A-exciton peak (note the negative sign of the y-axis). Inset shows the same plot zoomed over the first few picosecond time scale. The corresponding solid color lines are the best fit to the data	
4.2	using Eq.4.2	56
	first one picosecond delay regime.	57

List of Figures xv

4.3	(a) Variation of the peak change in the magnitude of $\Delta T/T$ with pump fluence extracted from the 2D plot shown in Fig.4.2(a). The linear fit	
	to the experimental points is also shown as a solid line. (<i>b</i>) Shows the fluence dependence of the initial fast decay time. The average decay time is shown as a dotted line	58
4.4	Schematic of the proposed processes: (<i>a</i>) Exciton dissociation leads to BGR and creation of hot-carrier by Auger and defect-assisted Auger scattering. (<i>b</i>) Cooling of hot carriers leading to formation of exciton and relaxation of carries to defect states which causes the relaxation of the measured $\Delta T/T$. (<i>c</i>) Filling of A-excitonic state leading to bleaching.	60
4.5	Fluence dependence of the magnitude of the initial negative peak (Blue dots) with best linear fit to the data represented as a blue solid line. Pump fluence dependency of the positive peak which occurs near three picoseconds delay (Red dots) with a quadratic best fit represented as a red solid line in the time dependence of $\Delta T/T$ with fluence (Fig.4.1) (see text for details)	61
4.6	(a) The fluence dependence of the estimated τ_s (decay time of the initial negative signal) and τ_r (the rise time of the later positive signal). (b) The fluence dependence of the decay time of the positive amplitude, τ_L . The solid line is the linear fit to the $1/\tau_L$ data	63
4.7	Schematic of the proposed processes: (<i>a</i>) Excitation of A-excitons (A-ex) by pump, exciton dissociation leads to BGR, and creation of hot-carrier by Auger scattering (CB-Conduction band and VB-Valance band). (<i>b</i>) Cooling of hot carriers leading to the formation of exciton and relaxation of carries to the defect states (DS)	65
4.8	Degenerate transient transmission signal measured on the same ML MoS_2 flake at its A-exciton (A-Ex) and B-exciton (B-Ex) peaks. Only the measurement at A-excitonic wavelength shows bleaching effect	67
5.1	Transient transmission signal measured on a ML MoS ₂ by exciting at 1.83 eV , 1.98 eV , and 3.09 eV which are within the peaks of (a) A-exciton, (b) B-exciton, and (c) C-exciton, respectively. Normalized signals of the same transient transmission signals are shown in the corresponding inset.	71
5.2	Pump fluence dependent transient transmission signal measured on ML MoS ₂ near (<i>a</i>) A-exciton, (<i>b</i>) B-exciton, and (<i>c</i>) C-exciton. Normalized signals of the same transient transmission signals are shown in the corresponding insets. Legends show the pump fluences used for these measurements.	73
5.3	Schematic of the proposed processes that happen at each exciton photon energy: (<i>a</i>) Processes at A-exciton where exciton dissociation and Auger scattering dominate. (<i>b</i>) Processes at B-exciton, here also exciton dissociation and Auger scattering dominate. (<i>c</i>) Processes at C-exciton where upon excitation carriers move in the opposite direction to achieve minimum energy states. At this excitation energy level, hot	
	phonon reabsorption dominates	75

List of Figures xvi

6.1	Pump fluence dependent transient transmission signal recorded by	
	pumping and probing at 672 nm pulsed laser: (a) Bulk MoS ₂ flake.	
	In the inset, the $ \Delta T/T $ is shown in a short time scale with y-axis	
	in natural log scale. (b) ML MoS ₂ flake. Inset shows the normalized	
	$ \Delta T/T $ in short time scale. In both these cases, the legend shows the	
	pump fluence which is in mJcm $^{-2}$	79
6.2	Pump fluence dependent variation of magnitude of the initial nega-	
	tive peak of $\Delta T/T$ of bulk MoS ₂ (red dots) and ML MoS ₂ (blue dots).	
	The solid red line is the best fit to the $ \Delta T/T _{Peak}$ of bulk MoS ₂ with	
	Eq.6.1 and the solid blue line is the linear fit to the $ \Delta T/T _{Peak}$ of ML	
	M_0S_2	81
6.3		
	and ML MoS ₂ (blue dots) flakes	82
6.4	Schematic of the proposed processes that follow after excitation of carriers at A-exciton transition energy in bulk MoS ₂ : (<i>a</i>) exciton disso-	
	ciation, Auger processes, (b) hot-carrier cooling, intervalley scattering.	84
R 1	Calculated time dependence of excited carrier density using Eq.B.3.	
D.1	The red line is the fit to the calculated carrier density with double	
	exponential decay function	95

List of Tables

3.1	The dependence of S_D and peak-to-peak variation in the signal at dif-	
	ferent chopper frequencies Ω_c around 333 Hz	45
3.2	The dependence of S_D and peak-to-peak variation in the signal at different chopper frequencies which are factors of 1 kHz	46
5.1	Pump fluence dependent $ \Delta T/T _{max}$ and decay time of the transient measurements performed at the excitonic peaks	74

Abbreviations

2D Two-Dimensional

TMDCs Transition Metal DiChalcogenides

ML Monolayer

CVD Chemical Vapor Deposition

MoS₂ Molybdenum Disulfide

AFM Atomic Force Microscope

OPA Optical Parametric Amplifier

BGR Band Gap Renormalization

BBO Beta Barium Borate

S/N Signal-to-Noise

Chapter 1

Introduction

The rapid growth in semiconductor industry as predicted by the Moore's Law is projected to approach its limit soon. The traditional microelectronic devices are now facing many challenges mainly in excessive energy consumption and the quantum limit. The demand for materials with distinctive physical and chemical characteristics as well as the technological requirements in semiconductor materials, have opened up new pathways in materials research. There are lots of research going on right now to create materials for new applications and to improve the efficiency of the existing devices. Materials for such applications must meet a number of conflicting conditions that are not satisfied by existing materials. Development of new materials of desired properties may be accomplished by reducing the size of the material and mixing different types of materials. Such reduction of dimensionality of the materials provide varieties of intriguing characteristics which can also be controlled by varying the size, shape, and arrangement. These nanostructured devices would be smaller, consume less power, and have a lower total cost of manufacture. These desires prompted the development of layered materials such as graphene, which has a wide range of intriguing characteristics. However, graphene is a semi-metal [1, 2] with no band gap and this issue had led scientists to look toward transition metal dichalcogenides (TMDCs) as a superior alternative.

TMDCs have risen in popularity as one of the most significant groups of materials for optoelectronic applications in recent years [3–5]. TMDCs are a group of

II-VI semiconductors having the chemical formula MX₂, where M stands for a metal atom (Mo, W, and so on) and X stands for a chalcogen atom (S, Se, or Te). These materials are made up of several layers bonded by a weak Van der Waals force between the layers [3, 4]. A single layer of TMDC material can be obtained easily from the bulk TMDC via mechanical exfoliation [6]. A monolayer (ML) can also be grown directly by the chemical vapor deposition (CVD) technique. Many of the bulk TMDCs have an indirect bandgap, but in their ML form, they change to a direct gap material with a plethora of interesting properties for various applications [3]. The shift in their electronic density of states is the most evident distinction. ML TMDCs have a semiconducting gap in the range 1-2 eV [3, 7].

Among the various TMDCs, Molybdenum Disulfide (MoS₂) has piqued the interest of the scientific community due to its stability, availability, and usage in a wide range of applications [8–10]. MoS₂ has the potential to play a key role in the development of future 2D electronics, valleytronics, spintronics, and bio-sensor applications [11–16]. The bulk MoS₂ is an indirect bandgap material of 1.29 eV bandgap energy [3, 4]. The bulk MoS₂ possesses its valence band maximum at the Γ point and conduction band minimum between K and Γ points [3, 4]. However, in its ML form, it acquires properties that aren't present in its bulk form. The ML MoS₂ is a direct bandgap material with 1.82 eV bandgap energy. The minimum of the conduction band and maximum of the valence band is located at the K point of the Brillouin zone in a ML MoS₂ (Fig.1.1(d)) [3, 4].

The two-dimensional (2D) MoS_2 is made up of one layer of Molybdenum (M) atoms sandwiched between two layers of Sulfur (S) atoms. These atoms are stacked in a hexagonal honeycomb lattice with a trigonal prismatic unit cell with D_{3h}^1 point symmetry group and $P\bar{6}m2$ space group [17]. The unit cell and lattice structure of a ML MoS_2 are shown in Fig.1.1(a) and Fig.1.1(b), respectively. Furthermore, because it is composed of heavy Mo-atoms, the outer electronic structure of the material receives the greatest contribution from the d-orbital of Mo-atom, which lead to high spin-orbit coupling [12]. This coupling is strong enough to eliminate the spin degeneracy both in the conduction band and valence band by establishing a strong energy difference between the spin-up and spin-down states. The splitting of the

valence band and conduction band in ML MoS₂ are around 130 meV and 3 meV, respectively [18, 19]. In addition, parity symmetry is also broken in ML MoS₂. Due to this, K point in the 2D Brillouin zone is not equivalent in all directions. As a result, it has two inequivalent K valleys in momentum space, namely K and K'. Fig.1.1(c) depicts the electronic band structure of a ML MoS₂. The time-reversal operator can be used to transform from one valley to another. As a result, valley-dependent optical selection rules are developed in ML MoS₂ where K valleys can be addressed individually using polarized lights. Left circularly polarized light (LCP) is used to address K' while right circularly polarized light (RCP) is used for addressing K valley [12]. This new degree of freedom opens up a new field like spintronics for information technology known as valleytronics where a specific polarized light can be used to excite carriers at a specific valley with a specific spin. Furthermore, these materials also show a significant quantum confinement effect and a strong Coulomb interaction due to its two-dimensional structure [20–22]. This leads to strong light-matter interaction in the visible region and exhibits three significant transitions owing to A, B, and C-excitons. Furthermore, strong Coulomb interaction and quantum confinement result in a high exciton binding energy of the order of 0.5 eV at ambient temperature [20-22] which resulted in greater absorption of light in the visible region, up to 20% in a ML itself [23]. The lifetime of radiative transition varies from a few hundred femtoseconds to many picoseconds. In ML MoS₂, a lot of optically prohibited states such as *p*-exciton with non-zero angular momentum, spin-forbidden intravalley exciton, exciton with a non-zero center of mass momentum beyond light cone, and intervalley excitons where electron and hole are positioned at separate symmetry locations are accessible in addition to the optically allowed bright excitons [24–26]. Apart from that, layered MoS_2 has a high degree of physical tunability like bandgap that can be changed by changing number of layers which bodes well for future optoelectronic applications.

Due to these special properties, it is reported to have many applications of MoS₂ in optoelectronic devices. Thus, it is important to understand the behavior of

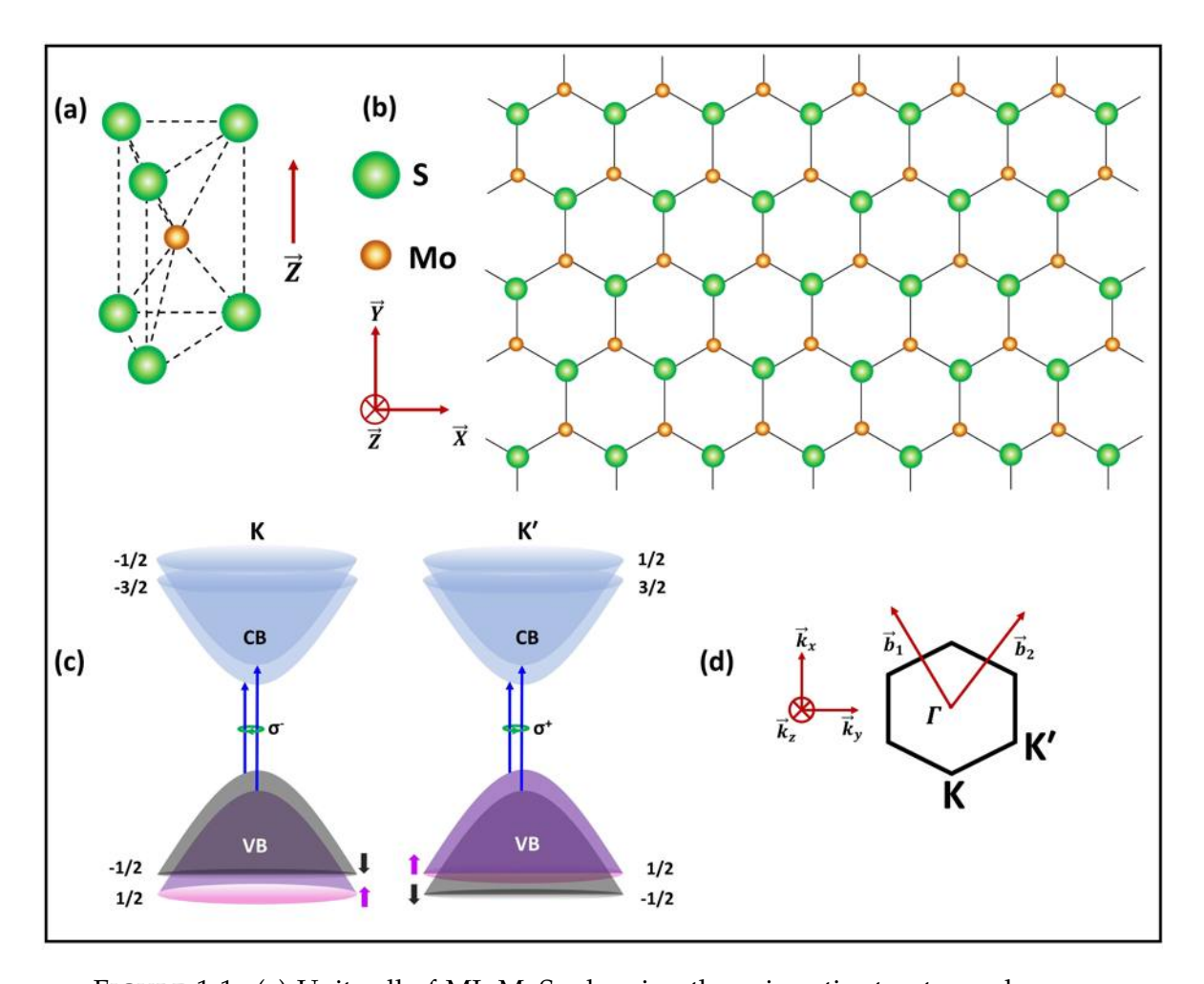


FIGURE 1.1: (a) Unit cell of ML MoS₂ showing the prismatic structure where one Mo-atom is sandwiched between two S-atoms. (b) Top view of a two-dimensional crystal structure of ML MoS₂. (c) Electronic band structure of a ML MoS₂ near K and K' points of the Brillouin zone showing band splitting. (d) Shows the hexagonal Brillouin zone of ML MoS₂.

the carriers in MoS₂ under various excitation conditions. Besides static optical properties like absorption and emission properties [3, 4], it is also important to understand the dynamics of the carriers in this material. Several groups have examined the ultrafast carrier dynamics in ML MoS₂ under various excitation conditions. Exciton relaxation via defect states [27, 28], exciton-exciton annihilation [29–33], Auger recombination, defect states assisted Auger recombination [34–37], and carrier cooling by phonon emission [38–42] are all examples of relaxation and scattering mechanisms observed in MoS₂.

The optical response of the material is strongly influenced by many given

physical processes which in turn strongly depends on the excited carrier density [27–42]. For a thorough knowledge on the material, it is necessary to measure the dependence of various time constants on excitation densities and comprehend the related physical processes. Fluence-dependent studies can also provide information about the underlining physical processes. In the case of MoS₂, such ultrafast carrier dynamics investigations at high excitation densities are relevant for its usability in devices that handle high carrier densities [43–46]. At present most of the carrier dynamics studies performed in ML MoS₂ are in the regime of low excitation density in the range $(N_x) \sim 10^{10}$ cm⁻² to $\sim 10^{14}$ cm⁻², [47–49]. However, there are relatively few studies in the regime above Mott density and all are limited to a maximum of 2×10^{14} cm⁻², [50]. Hence, it is important to know the carrier dynamics at carrier excitation densities well above the Mott density for the usability and applicability of ML MoS₂ as a component in lasers [43], compact OPAs [44], and high power detectors [45, 46] where high excitation densities are involved.

1.1 Ultrafast Processes During Carrier Dynamics Measurements

When an unperturbed material is excited by an ultrashort laser pulse, carriers are excited from the valance band to the conduction band or exciton states. Although initial carrier distribution can be non-thermal, soon various subsystems like electrons, holes, and phonons will reach an individual thermal equilibrium at their own time. In this situation, the carriers among the semiconductor subsystems may not be in thermal equilibrium with each other. Hence, from the excitation by an optical pulse, the materials will undergo several phases of relaxation and recombination overtime before reverting to a condition that is comparable to the initial thermal equilibrium state. The study of these relaxation phases and their temporal development will provide the full picture of carrier dynamics in a given material. These relaxation and recombination processes may be split into many time-overlapping

regimes: (i) coherent regime, (ii) non-thermal regime, (iii) hot-carrier regime, and (iv) isothermal regime.

During ultrafast excitation of the carriers, when a pump pulse arrives, the charge carriers in the semiconductors are driven by the electromagnetic field and are forced to oscillate with the same phase. When light interacts with electrons in a material, it creates new photon-dressed states, or Floquet states, with different energy levels than before. After excitation, an effective state is reached, resulting in a clear phase correlation between the produced polarization and the incoming light. This is called coherent regime. The quasi-particles that arise have a well-defined amplitude and energy. This is equivalent to a forced harmonic oscillation, in which the interaction energy between electrons and photons is transferred between each other on a periodic basis inside the material without any energy loss. When resonance light is absorbed, energy is lost by incoherent scattering processes, which are mediated by scattering channels. This coherent state can last up to hundreds of femtoseconds, after which various scattering mechanisms can kick in, resulting in a non-thermal state. These scattering mechanisms are carrier-carrier scattering, intervalley scattering, momentum scattering, and carrier-phonon scattering. Due to the short pulse-width of the laser, just after excitation, carrier distribution does not follow Fermi-Dirac distribution. Such non-thermal state is defined by the lack of a fixed temperature that may be used to characterize the carrier distribution. Over time various scattering processes will redistribute the energy among the carriers. Individual subsystems will attain a thermalized condition after the extra energy is dispersed among the carriers. The temperature of the individual subsystems, however, may differ. A hot-carrier regime usually refers to a thermalized condition inside a subsystem but not a thermalization among various subsystems in the material. When compared to the initial state of the sample, which was at a considerably lower temperature, there are electrons and holes in higher excited state at the end of the hotcarrier regime. These excited hot carriers will recombine over time in the isothermal regime via radiative or non-radiative process. The excitation condition and material property will determine all of these regimes. Various ultrafast processes are likely to occur under all of these regimes.

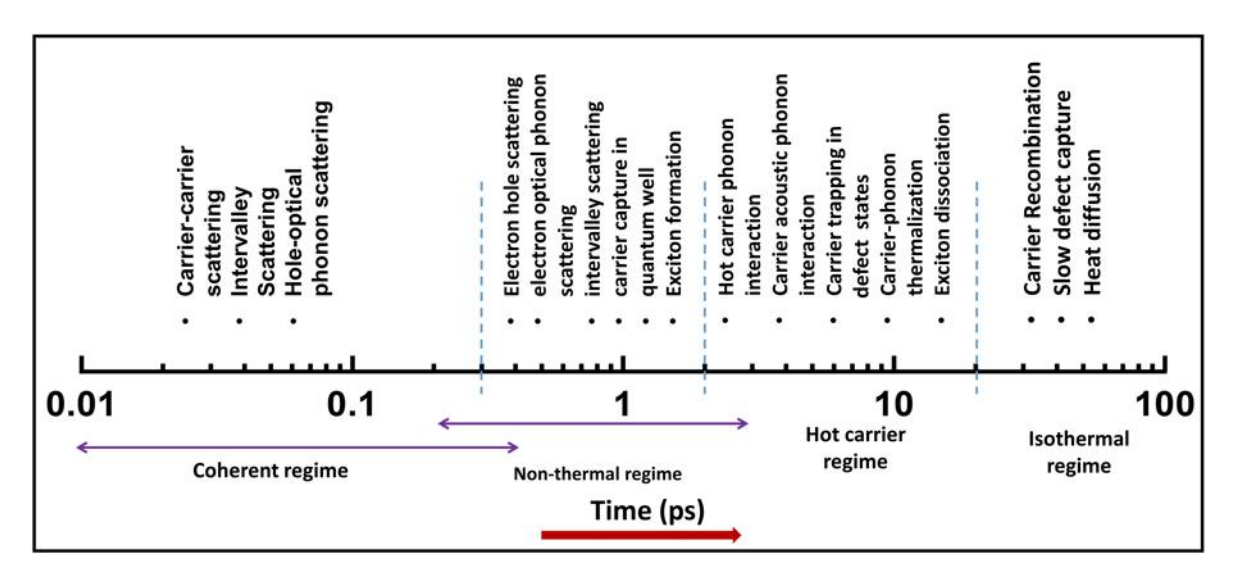


FIGURE 1.2: Typical time line of various processes that occur in a material upon photoexcitation. Note that, time line of all the processes depends on excitation density and material.

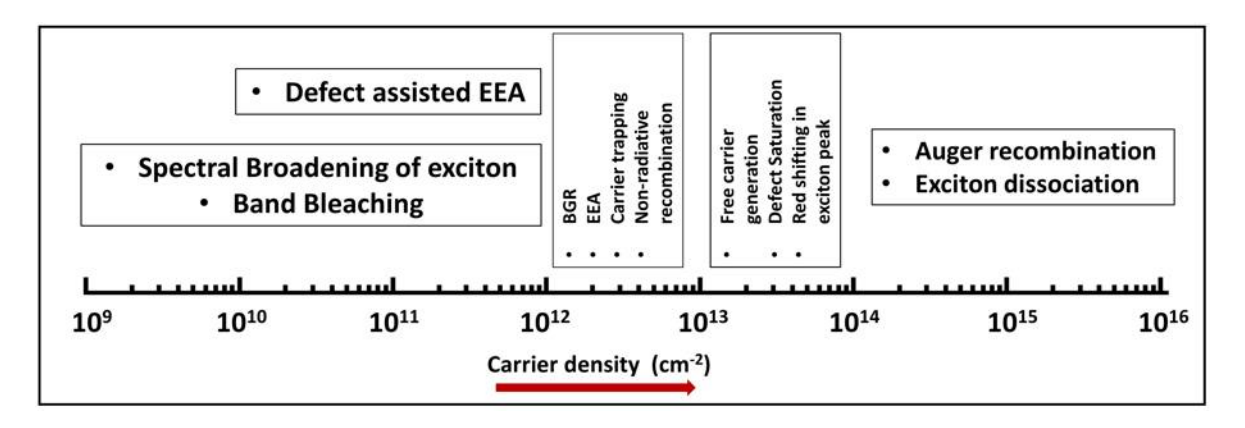


FIGURE 1.3: Photoexcitation density dependent ultrafast processes that happen in a ML MoS_2 that are dominant in the specific carrier density regime. Note that, these processes depend on material, pump fluence, and pump wavelengths.

Time line for all these processes and photoexcitation density dependency are shown in Fig.1.2 and Fig.1.3, respectively. Note that, all time and density dependency are material, pump fluence, and pump wavelength dependent [27–43, 50–55]. Let us look at some of the ultrafast events that occur after photoexcitation using an ultrashort laser pulse in details before we look at the carrier dynamics in ML MoS₂.

1.1.1 Thermalization of Photoexcited Carriers

As mentioned before, upon photoexcitation of the carriers from the valence band to the conduction band and the thermalization of carriers, the temperature of electrons, holes, and phonons can be different from each other. As a result, they will undergo various scattering processes and tend to thermalize among themselves and with the lattice. This is also affected by the band structure and excitation energy. The phonon spectrum and spin-orbit coupling of electrons also play a big role in the thermalization of photoexcited carriers, specifically in TMDC materials. For example, the split spin degeneracy in the valence band slows down the hole scattering through acoustic phonon interaction [56]. This leads to slower hole thermalization than electrons.

1.1.2 Exciton Formation

When an electron and a hole are created in the valence and conduction band after photoexcitation, they can interact via Coulomb interaction. If conditions are favorable, such interaction can produce an exciton. Such exciton formation is expected to be different in low-dimensional materials when compared to that of its bulk counterpart. Since 2D material like ML MoS₂ is atomically thin, electronic excitation will be confined within the 2D structure which is similar to a very thin quantum well. These properties will differentiate the excitons in bulk from that of ML. Due to the quantum confinement effect, there will be a stronger spatial overlap between electron and hole orbitals in the \hat{z} direction (perpendicular to the layer surface) in a 2D material. Furthermore, since screening is not available in \hat{z} direction, the electric field line between electron and hole will penetrate through air (Fig.1.4) [21]. These effects will increase the Coulomb interaction and hence the exciton binding energy. Indeed, the exciton binding energy can be as large as 0.5 eV in TMDC materials.

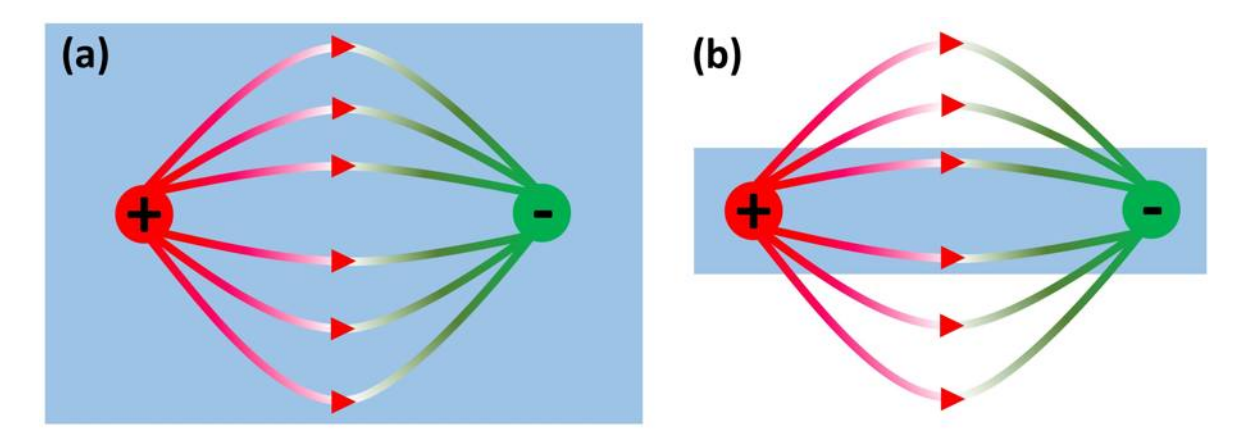


FIGURE 1.4: Exciton formation in (*a*) bulk semiconductor and (*b*) 2D semiconductor.

1.1.3 Carrier Trapping into Defect States

Defect energy states are created as a result of various defects in the material, such as point defects, vacancy states, stoichiometry defects, Frankel defects, Schottky defects, etc. In the case of ML MoS₂, these defect states can be formed during the growth or exfoliation processes. Most of the defect states are caused by S-vacancies. In its natural form, ML MoS₂ can also include additional S-atoms, which also cause defect states. After photoexcitation, some of the electrons and holes will be trapped in the defect states present in the material. The rate of carrier recombination in these defect states is proportional to the energy separation from the band edges. There are two types of defect states reported in ML MoS₂, termed (1) fast-defect states and (2) slow-defect states [36, 37]. When carriers are thermalized after photoexcitation, most of the holes which are then followed by electrons are caught in the fast-defect states within the first few picoseconds. During this time, a small number of holes are also trapped in the slow-defect states. When all of the holes have been captured and all of the fast-defect states have been filled by electrons, the remaining electrons will be trapped by the slow-defect states. Carrier trapping by fast and slow-defect states after thermalization is schematically shown in Fig.1.5.

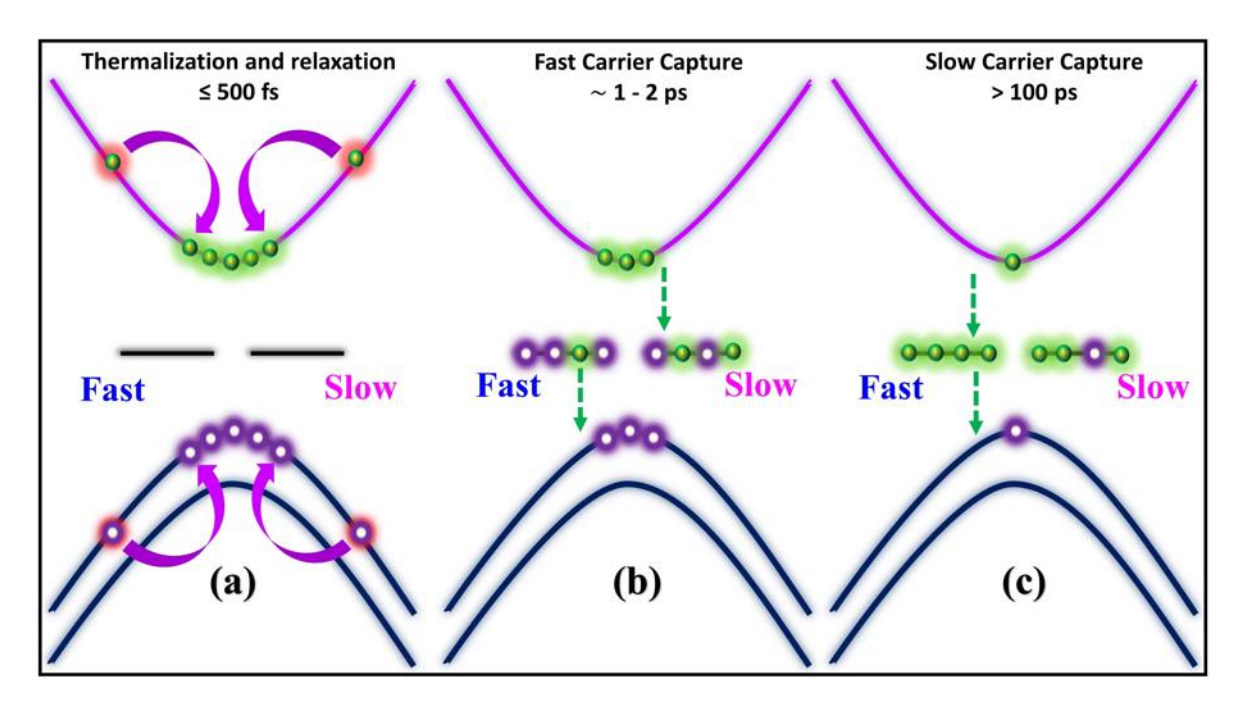


FIGURE 1.5: (*a*) The thermalization of carriers upon excitation by an ultrashort pulse, (*b*) fast trapping of holes and electrons by fast-defect states, and (*c*) slow capture of carriers by slow-defect states.

1.1.4 Auger Scattering & Defect-assisted Auger Scattering

Auger scattering is a type of non-radiative recombination wherein an electron and a hole recombine and transmit their energy to a third carrier, which then gets excited to a higher energy state. At high excitation carrier densities, this scattering process has a strong impact on the carrier lifetime, the recombination processes in a material, and the radiative efficiency. In the case of TMDC materials, the defect states also play a critical role in the Auger scattering processes giving rise to defect-assisted Auger recombination. In this process, electron and hole recombination is aided by defect states [36, 37]. A pictorial representation of defect-assisted Auger processes is shown in Fig.1.6. Auger and defect-assisted Auger is stronger in a ML MoS₂ due to the strong Coulomb interaction [36].

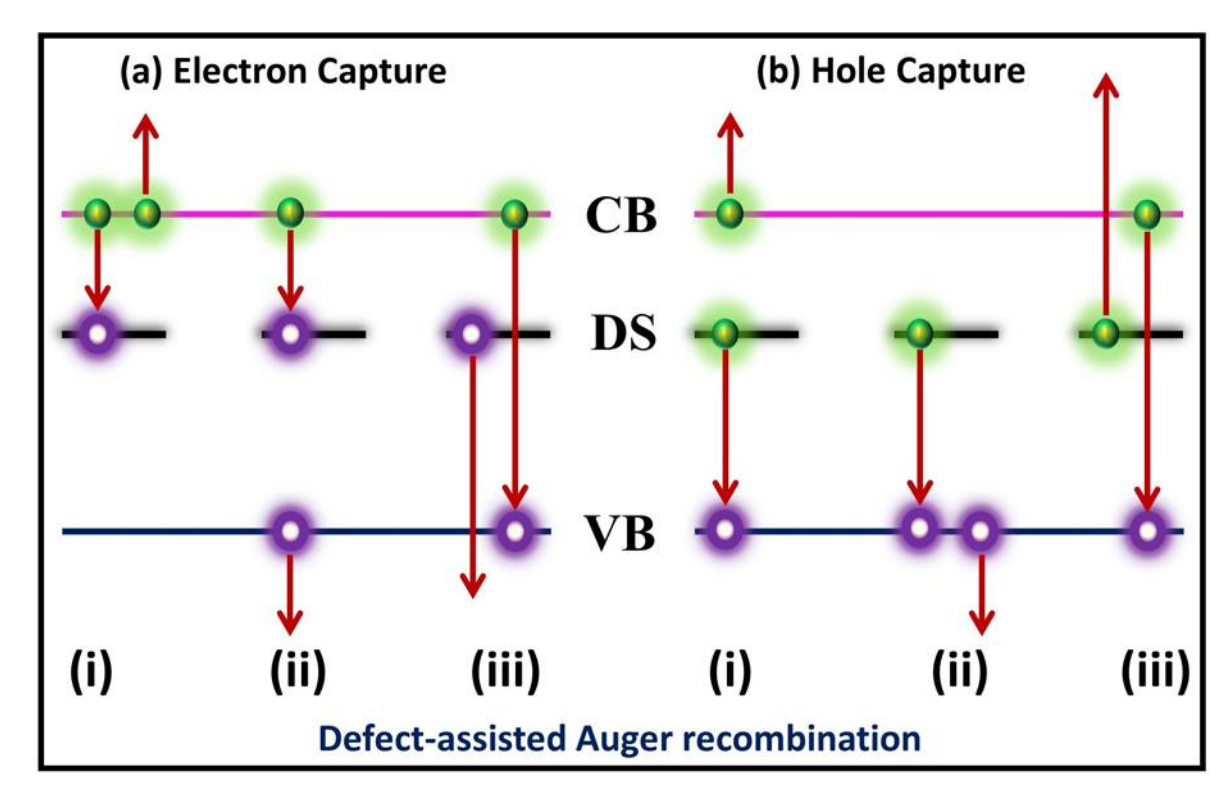


FIGURE 1.6: (*a*) An electron or (*b*) a hole is captured by the defect states. In each, three different capture processes are shown.

1.1.5 Exciton-Exciton Annihilation (EEA) and Defect-assisted EEA

In some materials where the Coulomb interaction is strong, electrons and holes couple to produce excitons. These excitons will dominate the relaxation process after excitation as long as the excited carrier density is less than the Mott density. A Auger like scattering is predicted to occur between two excitons rather than three free particles in this situation. As a result, EEA, a four-body process where one pair of electron-hole transmits their energy and momentum to the other pair, will happen [29, 33]. This process is extremely efficient in low-dimensional materials such as quantum dots [57, 58], graphene nanoribbons [59], polymer chains [60, 61], carbon nanotubes [62], etc. A schematic of the EEA process in ML MoS₂ is shown in Fig.1.7. EEA can occur in two ways: direct Föster resonance energy transfer (FRET) and multistep diffusion. For ML MoS₂, EEA for the A and B-exciton happens via FRET, and EEA of C-exciton occurs via diffusion [29]. EEA can also occur with the assistance of defect states where an exciton is annihilated by Auger recombination [36, 63].

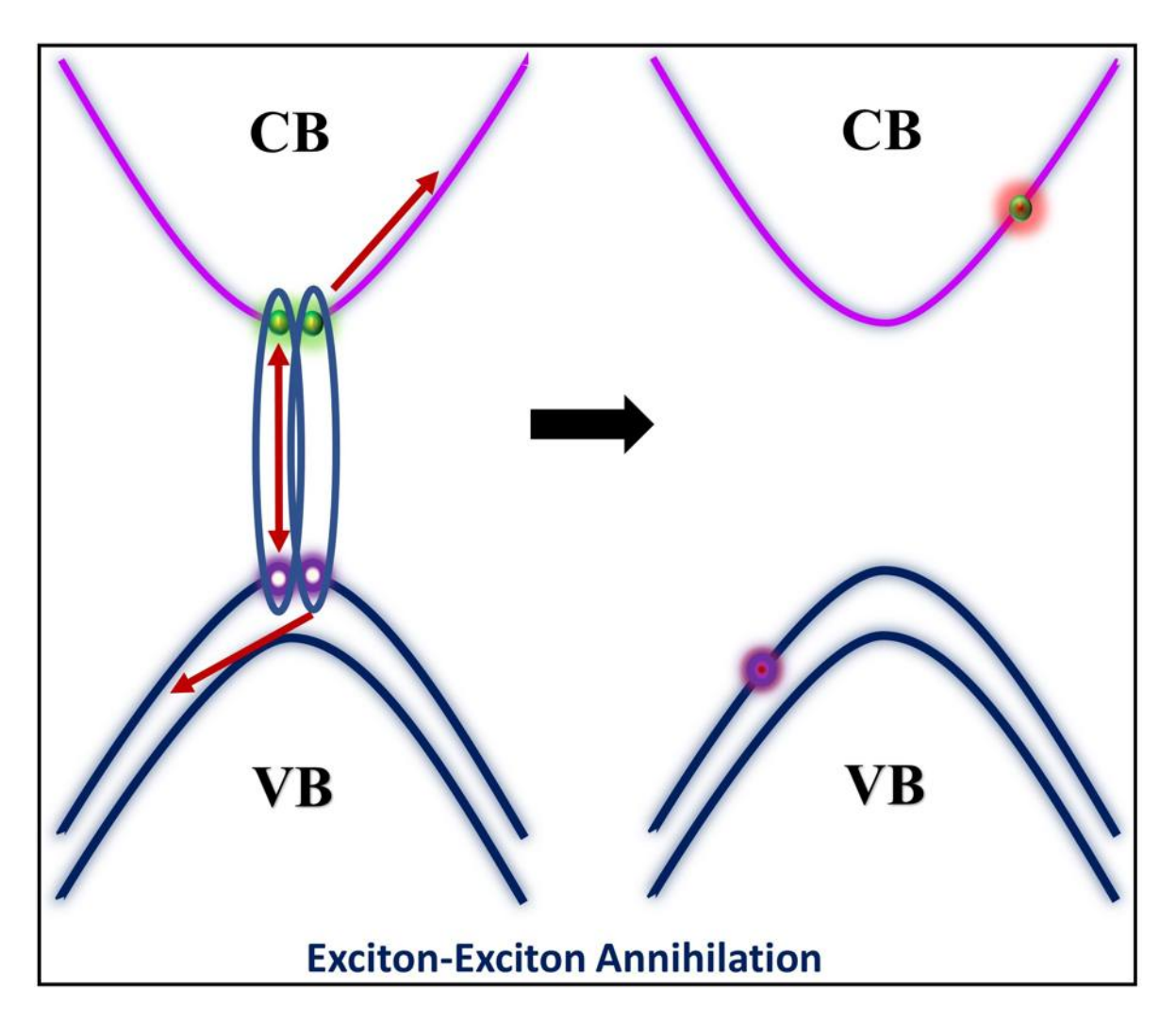


FIGURE 1.7: Exciton-exciton annihilation in a ML MoS₂ showing two excitons participating in the recombination process. One exciton will recombine and transfer its energy to another exciton taking the electron and hole to higher excited states.

This mechanism is influenced by the density of excitons and becomes efficient when exciton density is more than $\sim 10^{12}~\rm cm^{-2}$ [33]. According to recent research, the EEA rate in single layer TMDC is higher than its multilayer equivalent [33, 64]. This EEA process has a strong impact on the performance of optoelectronic devices. It is responsible for the unwanted efficiency loss in photoluminescence (PL), whereas energy conversion necessitates the formation of electron-hole pairs upon exciton annihilation [64, 65]. EEA can also be employed for optical up-conversion in 2D TMDCs [66].

1.1.6 Hot-Carrier Cooling

Hot carriers are those with kinetic energy k_BT greater than the conduction band or the valence band energies and it follows a Boltzmann distribution. They are formed as a result of photoexcited non-equilibrium carriers being thermalized by carrier-carrier scattering, the EEA process, Auger, and defect-assisted Auger scattering processes. They eventually reach equilibrium with the lattice due to carrier-phonon scattering and Auger scattering. Hot-carrier cooling is a complex process involving carrier-carrier, carrier-phonon, and phonon-phonon interactions, all of which are influenced by the band structure of the semiconductor. In every material, the dynamics of the hot carriers are critical for its applications. In ML MoS₂, this process is crucial as, during the cooling and thermalization of the hot carriers, a large number of non-equilibrium hot-phonons are generated [38, 39, 51]. These hot-phonons will create a bottleneck process where hot-phonons are reabsorbed by the carriers and excited to higher energy states prolonging the carrier cooling process [54, 67]. In Fig.1.8(c), a schematic representation of hot-carrier cooling is shown.

1.2 Ultrafast Modification of Optical Response of Materials

Following carrier excitation, the band structure of the material will change based on the photoexcited carrier density and the distribution of carriers in the excited state. Such carrier redistribution compared to ground state leads to change in the optical response of the material through band bleaching, bandgap renormalization (BGR), and exciton state modifications.

1.2.1 Band Filling and Band Bleaching

Due to the fermionic nature of the carriers, once an energy level is occupied by a carrier, no other carrier can occupy that same energy level. As a result, further

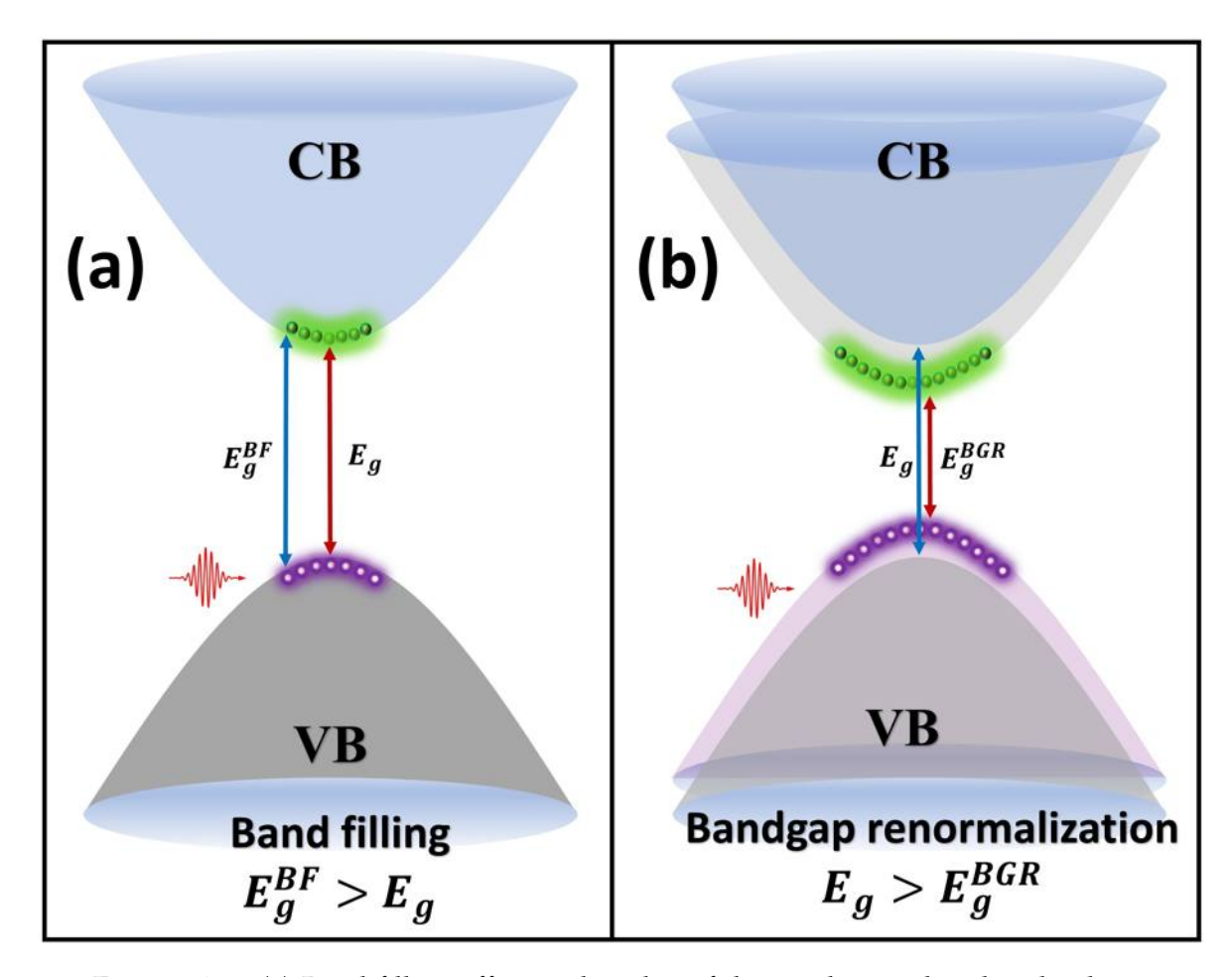


FIGURE 1.8: (a) Band filling effect at the edge of the conduction band and valence band due to photoexcitation. In this case, the original bandgap (E_g) is lower than the new bandgap (E_g^{BF}). (b) The BGR effect at the band edge when excitation density is high. In this case, $E_g > E_g^{BGR}$.

excitation of carriers to the same level will be prevented. Under thermalized condition, the excited electrons will occupy states near the edge of the conduction band (bottom), while the holes will occupy states near the band edge of the valence band (top). Now if the material is illuminated with a light of a wavelength that corresponds to the bandgap, the absorption at these wavelengths will be less. The filling of the band that leads to a decrease in the absorption coefficient is referred to as the "band-filling effect". As a result, the bandgap of the material is effectively assumed to have increased as schematically shown in Fig.1.8(a). Similarly reduction of electrons in the valance band due to its excitation to other excited states by a pump pulse will also reduce absorption at an excitonic state called as band bleaching. The band filling and band bleaching effect play a strong role in modifying the optical response

when excited carrier densities are lower than the Mott density [31, 68, 69].

1.2.2 Bandgap Renormalization (BGR)

When electrons are excited from valence band to conduction band, they thermalize and occupy the bottom of the conduction band. During this process, their wave functions will overlap if the excited carrier density is high enough. Furthermore, due to the Coulomb interaction, the same charges will repel each other, and the same spins avoid each other due to Pauli's exclusion principle. This lowers the energy of the conduction band edge by forming tails of the density of states at the band edge. Due to holes, a similar effect will also occur at the valence band maxima. These changes will decrease in band gap resulting in the bandgap renormalization effect (Fig.1.8(b)). Due to the strong many-body Coulomb interaction in MoS₂ samples, the BGR effect is large [69].

1.2.3 Exciton Peak Shift and it's Broadening

Depending on the excited carrier density, band filling, band bleaching or BGR will occur whilst carriers are excited from valence band to conduction band. Hence the linewidth of the exciton broadens, and the peak of the exciton shifts due to Coulomb interaction, Pauli's exclusion principle, and wave function overlapping [70–73]. Bera *et al.* [70] and Katsch *et al.* [72] showed that BGR can lead to exciton peak shift and linewidth broadening. The linewidth broadening is found to be dominant in presence of exciton-exciton and exciton-phonon interactions [72, 73], while peak shift of the exciton will occur when excitation density is higher than Mott density due to the electron-hole plasma [70].

1.3 Applications of Monolayer MoS₂

As discussed earlier, TMDCs feature an adjustable bandgap, high exciton binding energy, and strong PL, making them a viable candidate for solar cells, photodetectors, light-emitting diodes, and photo-transistors [3, 4, 20]. For example, the direct bandgap (~ 1.82 eV), high optical absorption coefficient ($\sim 5 \times 10^7$ m⁻¹ in the visible range) which is an order greater than that of GaAs and Si [74] (when normalized to corresponding thickness). The ML MoS₂ shows a strong mobility (~ 200 -400 cm² V⁻¹s⁻¹) [75], high current on/off ratio ($\sim 10^7$ – 10^8) [7], and strong PL emission efficiency [3, 4]. Thus ML have all been widely investigated for various electronics and optoelectronic applications. In this section, some of the these applications of ML MoS₂ are discussed. These studies that are carried out and reported in this thesis are useful for all these applications.

- Valleytronics: It is a technology that uses the valley degrees of freedom to store, alter, and transport data. Different quantum manipulation technologies, such as quantum computation employing valley qubits, can also be achieved via valleytronics. The most essential motive for valleytronics is its applicability in low-energy information storage and processing, such as data transfer without Ohmic heating owing to charge transfer. Valleytronics can be accomplished in materials with multivalley in the first Brillouin zone. Since ML MoS₂ has these qualities, it can be employed in this technology [11, 76].
- **Spintronics:** Internal degrees of freedom, such as carrier spin, are employed in this technology to store, alter, and transfer data. Less energy is lost in this technology, resulting in low power usage. Spin-orbit coupling is a fundamental pre-requisite for spintronics because it allows spin degrees of freedom to adapt to their orbital surroundings. As a result, spin splitting occurs in the electronic band structure where inversion asymmetry exists. All of these features are possessed by 2D MoS₂, making this an excellent choice for spintronics applications [12].

- Electronics: The difficulties that are faced by the semiconductor industries to overcome the limit of Moore's law, can be resolved by employing 2D TMDCs, which can confine carriers to a physical limit of 1 nm. These materials also have a high carrier mobility and are very easy to manufacture. As a result, these materials can be employed to create transistors that can transcend physical restrictions [9, 77]. Since transistors are the basic building blocks of the memory devices, ML materials can be used to make high storage in a compact form. A 2D semiconductor (MoS₂) microprocessor has also been proposed recently [13]. This device is built up of 115 transistors, which comprises all of the fundamental microprocessor building components.
- **Supercapacitor:** Energy storage technologies based on superconductors play an important role in traditional energy domains. They are all confronted with technological challenges that must be overcome fast to meet the growing demand for superior clean energy technology. 2D MoS₂ may assist in improving various properties of these energy storage devices due to its thin structure, wide surface area, and high surface stability, making it a promising material for building a supercapacitor [15, 16].
- **Solar Cells:** One of the most significant milestones for the future of energy harvesting is the development of low-cost, printable, high-performance, and stable solar cells. 2D MoS₂ is one such material that meets all of the criteria for a viable alternative to silicon-based solar cells due to its increased photovoltaic performance and stability in its original form or heterostructure with other 2D TMDCs [78, 79].
- **Biomedical Applications:** Due to the adjustable optical and electrical properties of TMDCs, high surface-to-volume ratio, and outstanding biocompatibility [80], these materials can also be employed in biomedical applications. Extensive research is being conducted to improve these materials for many biomedical applications. These materials have applications in cancer therapy, tissue engineering, drug delivery, wound repair, antimicrobial, bioimaging,

and other fields [80–82]. It is anticipated that these materials will have a strong basis and will play a key role in next-generation biomedicine.

- **Sensors:** As with biomedical applications, 2D TMDCs are also usable in sensors. (1) Electrochemical sensors: These sensors detect glucose, hydrogen, DNAs, proteins, and other molecules [7]. (2) Fluorescence Sensor: These sensors can also detect viruses, proteins, metal ions, and DNA. Here, fluorescence is employed as a probing approach in these sensors [83, 84]. Besides these, ML MoS₂ can also be used in various optoelectronic applications [85, 86].
- Optoelectronic application: 2D TMDCs have transformed laser technology in recent years. Saturable absorbers for ultrafast lasers can be created using these materials that are efficient and cost-effective. This is because of their broad absorption spectrum, low fluence saturation, and quick recovery period. The first TMDC material utilized as a saturable absorber is MoS₂. The first mode-locked laser operated utilizing TMDC was also demonstrated using MoS₂ [14].
 - (1) Mode locker: Wang *et al.* demonstrated a broadband saturable absorber using MoS₂ and achieved Q-switching with a pulse-width of 410 ns [87]. Besides this, a heterostructure of MoS₂ showed better Q-switching and mode-locking when compared to bulk MoS₂ [43].
 - (2) Optical parametric amplification: An OPA was also demonstrated using a single layer MoS₂ where amplification was achieved by bypassing phase matching conditions where a ultrabroad amplification bandwidth was achieved [44].
 - (3) Photodetector: photodetectors based on MoS₂ hybrid structures were also demonstrated [46]. Here, it was shown that the MoS₂ hybrid could be a better option for photodetectors and optoelectronic building block with high responsivity, faster response time with better stability under room temperature when exposed to atmosphere.

1.4 Organization of the Thesis

In this thesis, ultrafast dynamics of the photoexcited charge carriers were studied at A and B-exciton as well as at C-exciton states of a ML MoS₂. These studies are carried out in a degenerate pump-probe configuration which involves pumping and probing the carriers at the individual excitonic states. All these studies are carried out at carrier densities above Mott density where charge carrier dynamics have not been well understood. The excitation carrier density used in these studies is in between $\sim 6.6 \times 10^{13}~\text{cm}^{-2}$ to $\sim 6.7 \times 10^{14}$ cm⁻². In Chapter 2, various characterizations of a ML MoS₂ and bulk MoS₂ that is useful for understanding their transient optical response are described. Chapter 3 focuses on several transient detection techniques used to evaluate changes in the optical response of the sample as well as various noises that can affect the signal detection. This chapter also describes a highly sensitive detection technique that can be employed when transient measurements were performed using a low-repetition rate laser system. In Chapter 4, carrier dynamics studies performed near A-exciton have been presented. In Chapter 5, a comparative study of the carrier dynamics near A, B, and C-excitons is reported under similar excitation densities. Chapter 6 reports a comparative study of the transient carrier dynamics of a multilayer and ML MoS₂ under similar excitation densities at A-exciton. Finally, in the Chapter 7, summary of the study, conclusion, and future scopes are presented.

Chapter 2

Experimental Technique and Basic Characterization of 2D Samples

MoS₂ is widely available in nature in the form of Molybdenite ore. A single layer MoS₂ can be separated from the bulk MoS₂ using different methods like mechanical exfoliation using scotch tape [6], chemical exfoliation by using different chemicals [88]. This also can be done through chemical vapor deposition (CVD) [89], sulfurization of Mo and Mo-based oxides [89], thermal decomposition of (NH₄)₂MoS₄ [90], vapor-solid growth from MoS₂ powder [91], etc. Among these preparation methods, using CVD, a large area single thickness sample can be prepared. Besides these, using CVD method contamination can be avoided which is not possible during exfoliation and other preparation methods. The monolayer and multilayer under-study in this thesis were grown by CVD technique [92]. The microscopic optical image of the sample shows several well-separated as well as conjoined flakes with well-defined grain boundaries. Few multilayer flakes are also observed at some areas of the substrate which are well separated from other flakes.

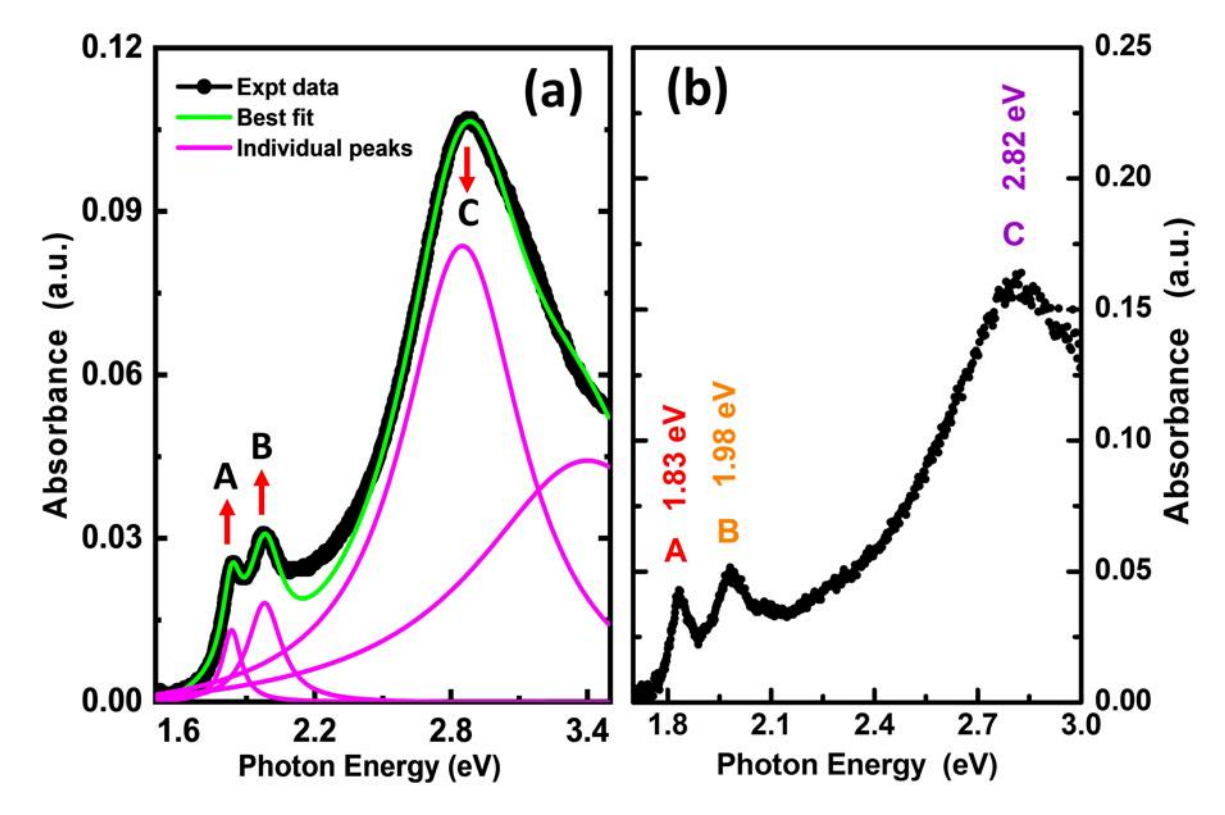


FIGURE 2.1: (a) Absorbance spectrum of ML MoS₂ sample recorded using a UV-Vis spectrometer and fitted with four Lorentzian peaks corresponding to transition energy of A, B, C-excitons, and a higher energy transition peak. Green line represents the best fit to the absorbance spectrum and the magenta lines represent individual contributions. (b) The measured microscopic absorption spectrum of the flake used for transient measurements.

2.1 Optical Characterization

Before performing the transient optical response measurements, it is essential to study the linear optical properties of the sample. The large area absorption spectrum is shown in the Fig.2.1(a). The spectrum was measured with a UV-Vis-NIR spectrometer (Shimadzu UV-3101PC). This spectrum shows three distinct peaks which correspond to the A, B, and C-excitonic transitions. Among them, the A and B-excitonic peaks are due to exciton formed between the conduction band and the dual valance band caused by splitting of the bands near the band edge [3]. C-exciton peak is due to the transition between the valance band and the conduction band in the band nesting region [30]. Fig.2.1(a) also shows the best fit to the absorption data with four Lorentzian peaks. The peak photon energies of these A, B, and C-exciton

are 1.83 eV, 1.98 eV, and 2.86 eV, respectively. The corresponding spectral widths are 0.11 eV, 0.18 eV, and 0.68 eV, respectively. Note that the absorption coefficient at the peak of B-exciton and C-exciton is \sim 1.24 times and \sim 4.28 times than that of at A-exciton. The average spectrum of the flakes is most likely to give the spectrum of a ML since most of the substrate is covered with ML except at few places where multilayered flakes were observed.

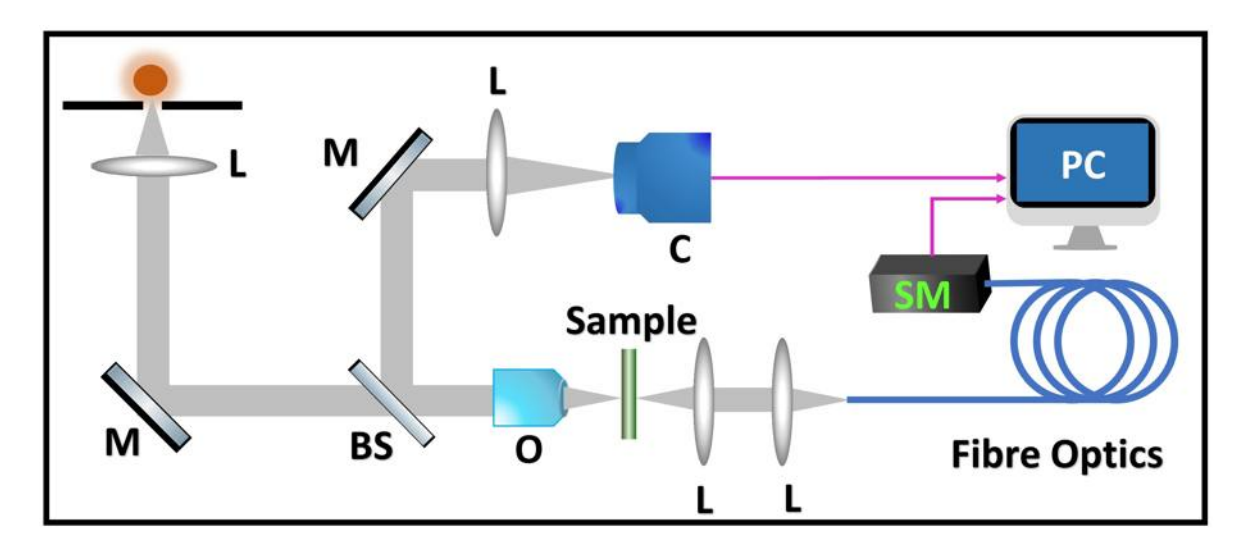


FIGURE 2.2: Schematic of the microscopic absorption spectrometer setup developed for the measurement on samples smaller than 100 μ m. BS: Beam Splitter, C: CCD camera, L: Lens, M: Mirror, O: Objective, SM: Spectrometer.

To measure the absorption spectrum of a single ML sample, a microscopic setup was developed using a 50X objective, a white light source, collection optics, and a fiber spectrometer which is shown in Fig.2.2. In this setup, transmission of the bare substrate was recorded which act as background transmission. Then, using a CCD camera, white light is focused on the monolayer flake to measure its transmission. Subtracting the background from the transmitted light through the flake and substrate, transmission only through the flake is calculated from which absorbance is determined using Beer-Lambert law. The measured absorption spectrum of a single ML flake on which transient measurements were performed is shown in Fig.2.1(b). The absorption spectrum shows three excitonic peaks, A, B, and C at 1.84 eV, 1.98 eV, and 2.87 eV, respectively.

2.2 Stability Measurements

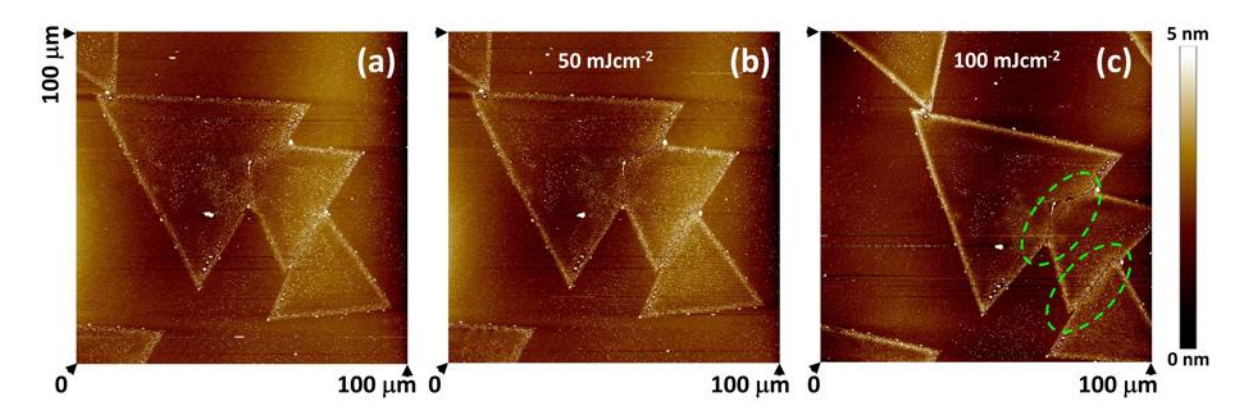


FIGURE 2.3: AFM topography images of few monolayer flakes after being exposed to 672 nm femtosecond laser beam at different fluences: (a) before exposure, (b) exposure to 50 mJcm⁻² and (c) 100 mJcm⁻². Dotted ellipses show the regime where structural modifications were observed.

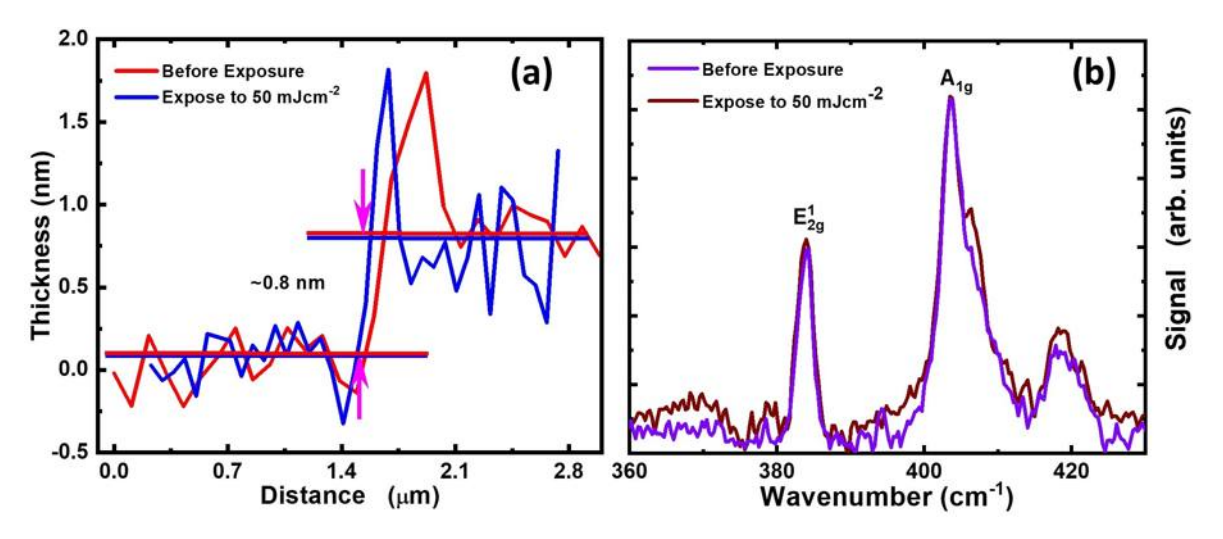


FIGURE 2.4: Damage threshold measurements of the ML MoS₂ flake: (a) AFM line profile of the flake before and after exposure to 50 mJcm^{-2} , and (b) Raman scattering of the same flake before and after exposure to 50 mJcm^{-2} pump fluence.

Before carrier dynamics measurements, it is also essential to confirm that the sample is stable even at much higher excitation conditions than that used in the transient experiments. Changji Pan *et al.* investigated the impact of high-density laser irradiation on the MoS_2 flakes [53]. They have shown that structural changes in MoS_2 occur when exposed to fluences of the order of 150 mJcm⁻². Exposure to even higher fluences, like 400 mJcm⁻² resulted in the development of nanoridges

and nanocracks in the MoS₂ flakes [53]. In order to check the stability of the present sample to 672 nm irradiation, we have exposed the ML MoS₂ flakes to different increasing fluences for about 10 min at each fluence. Following each exposure, the AFM image of the same flake was recorded. Fig.2.3 shows the AFM topographic images of few of these ML MoS₂ flakes after being exposed to different fluences. The topography of the flake remained the same even after exposing the sample to fluences up to 100 mJcm^{-2} . These structural characterizations as well as Raman measurements before and after exposure clearly show that the sample is stable for exposure to even higher fluences than that used in the transient measurements. Only when exposed to about 100 mJcm^{-2} , the AFM image showed a widening of the gap near the grain boundaries of the flakes. Still topography of the ML MoS₂ away from the edges and grain boundaries remained the same. Thus even at 100 mJcm⁻², the damage is occurring at the edges and grain boundaries of the flake. Hence from the measurements in ML MoS₂ flake, it can be safely said that the flakes are intact at the maximum pump fluence used in the current studies. In the current transient measurements, the used maximum pump fluence is 12.2 mJcm⁻² which is almost ten times less than the pump fluence at which only the grain boundary of the samples damages. Moreover, the experiments were also performed at a location well away from the edges and grain boundaries (Fig.2.5(a) and Fig.2.5(b)).

Further, stability study on the ML MoS₂ sample is verified using AFM line profile and Raman scattering measurements. To establish that the flakes were stable even at much higher fluences, AFM and Raman measurements before exposure and after exposure to 50 mJcm⁻² fluence were performed. Both the thickness as well as the Raman features are found to remain nearly the same. Hence, the stability of the ML flake is confirmed.

2.3 Selection of Flakes and AFM Images

To perform measurements on a selected MoS₂ flake, we use a 50X long working distance objective, a white light source, and a CCD camera. Using this optical

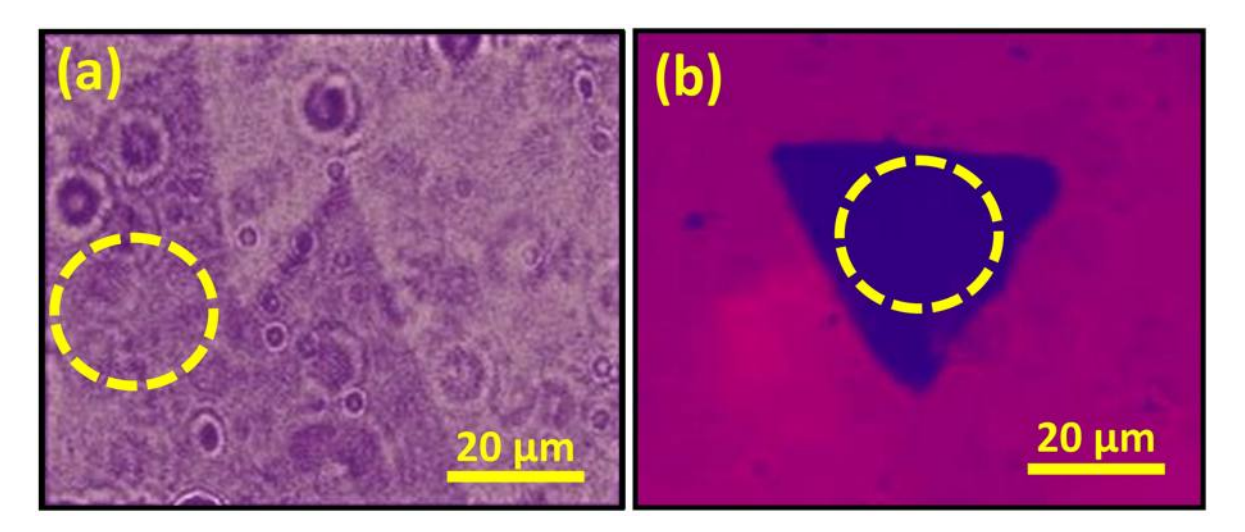


FIGURE 2.5: Optical image of (*a*) ML MoS₂ flake and (*b*) multilayer MoS₂ flake captured in a microscopic setup developed in the pump-probe setup.

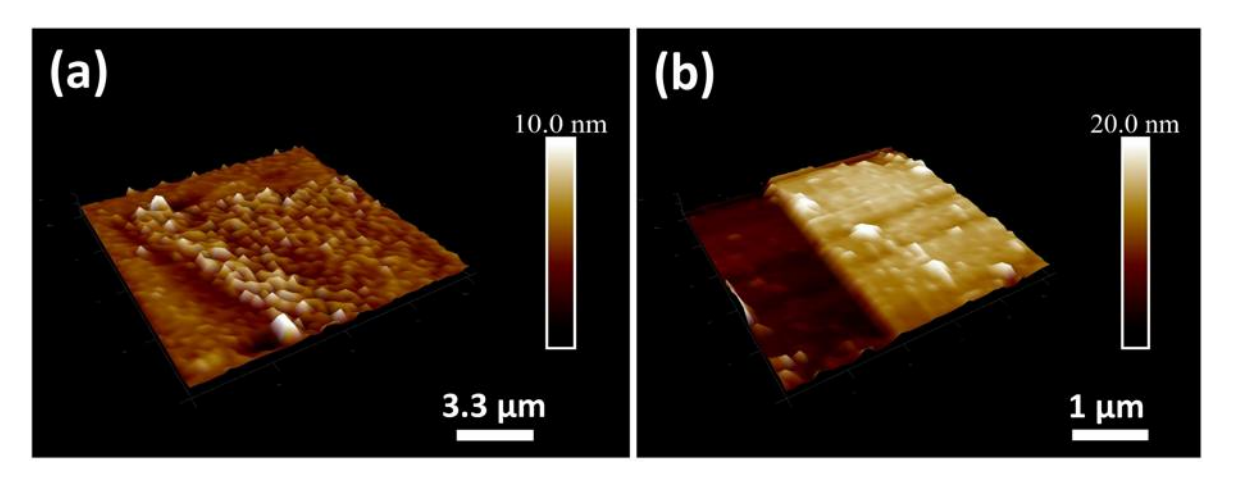


FIGURE 2.6: AFM topographic image of (*a*) ML MoS₂ flake and (*b*) multilayer MoS₂ flake. These AFM scans are taken at one corner of the flakes.

microscope arrangement in the pump-probe setup, the MoS_2 flakes were viewed. Among the various flakes, a specific ML and multilayer flake were selected for the transient measurements which are shown in Fig.2.5(a) and Fig.2.5(b), respectively. The dotted circle in both the images shows the area where pump-probe measurements were performed. The AFM topographic image of the ML and multilayer MoS_2 flakes across one edge are shown in Fig.2.6(a) and Fig.2.6(b), respectively.

To confirm that the used flake for the measurements is a ML, AFM and Raman measurements were performed. The thickness of the flake was estimated by

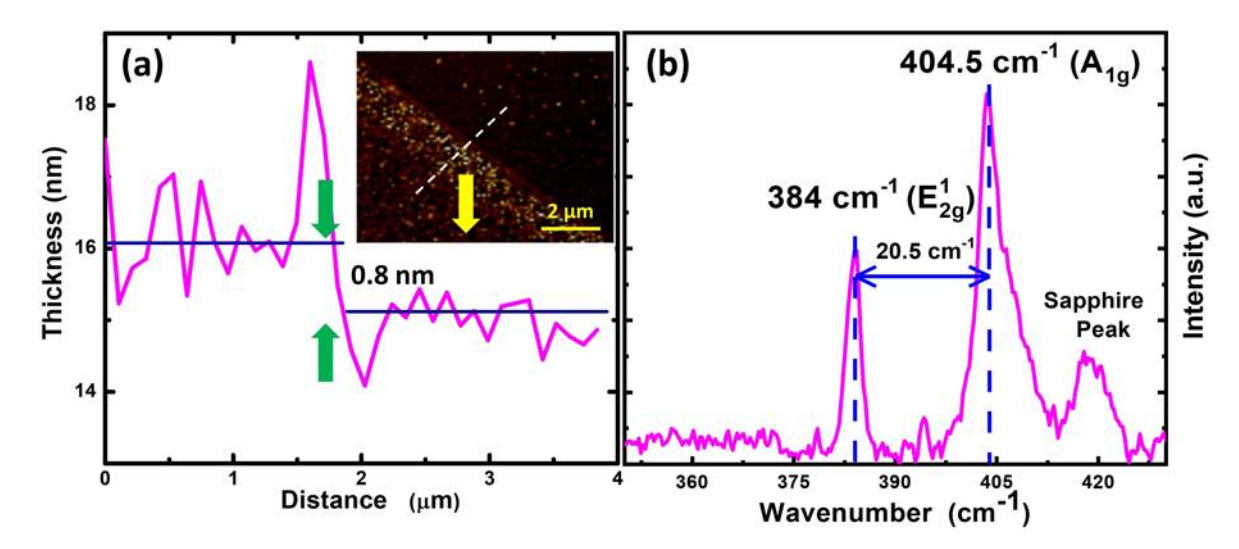


FIGURE 2.7: (a) AFM line profile of the ML flake at one edge for the thickness measurement with the AFM topography of the flake in the inset and (b) Raman spectrum of the ML MoS₂ flake used in the transient transmission measurement.

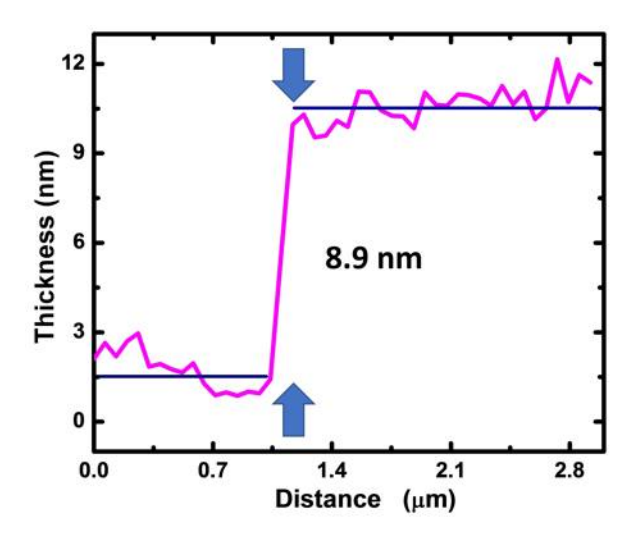


FIGURE 2.8: AFM line profile of the bulk MoS₂ flakes used in carrier dynamics studies for thickness measurement.

performing AFM topography scanning measurements at several locations. A representative topography scan of the same is shown in the inset of Fig.2.7(a), which shows the thickness variation across an edge of the flake. This measurement confirms that the sample used for the transient measurements is a ML with thickness ~ 0.8 nm [3, 54]. Raman spectrum of this flake has been recorded and shown in

Fig.2.7(b) which shows two peaks at 384 cm⁻¹ and 404.5 cm⁻¹ corresponding to inplane mode (E_{2g}^1) and out-of-plane mode (A_{1g}) peaks, respectively. The wavenumber difference between these two peaks is 20.5 cm⁻¹. These Raman data confirm that the flake used in the transient measurement is a ML MoS₂ flake [41, 93]. To confirm the number of layers present in the bulk MoS₂ sample, the AFM line profile of the flake is shown in Fig.2.8 which was also measured at one edge of it. From this line profile, the thickness of the bulk flake is found to be \sim 8.9 nm. When compared to the thickness of ML MoS₂, it is an 11 layers flake.

2.4 Summary

In this chapter, various optical and physical properties of the used flakes have been presented. From the absorption profile of the ML MoS₂ flake, three excitonic peaks has been confirmed. These excitonic peaks are found to remain the same when measurements were carried out on a single flake as well as over a large area average spectrum. This indicates that most of the flakes were monolayer in the sample. From AFM line profile and Raman scattering, the flake on which transient measurements were carried out was confirmed to be a monolayer. Further, damage threshold measurements are performed using AFM topography scanning and Raman scattering which confirm that the sample is stable within the fluence range used in the experiment.

Chapter 3

Augmentation of Experimental Setup

Ultrafast optical pump-probe spectroscopy is a powerful tool to explore carrier dynamics in materials. The simplest version of this approach involves changing the carrier distribution in the sample with an intense laser pulse, known as pump, with a temporal pulse-width much less than the material's response time that is of interest. Excitation with such laser pulse modifies the optical response of the material [94–97]. On the other hand, a less intense pulsed laser, known as probe, is used to measure the changes induced by the pump pulse in the sample. By adjusting the delay between the pump and probe pulses, the carrier dynamics in the sample is studied. Due to the availability of optical pulses of temporal width as small as a few tens of attoseconds, any process in the material longer than this pulse-width can be studied. A key benefit of this technique is that we do not require any fast photodetector for measuring the ultrafast response.

In this chapter, various pump-probe techniques that are employed during the measurements are discussed. Furthermore, different types of noises that can affect the signal are discussed. A lock-in amplifier based phase-sensitive detection technique is described. In addition[†], certain noises that can affect the signal-to-noise

[†]This work is published by the author of this thesis as "Filtering noise in time and frequency domain for ultrafast pump–probe performed using low-repetition rate lasers", **Durga Prasad Khatua**, Sabina Gurung, Asha Singh, Salahuddin Khan, Tarun Kumar Sharma, and J. Jayabalan, Review of Scientific Instruments 91, 103901 (2020) and reproduced with the permission of AIP publishing.

(S/N) ratio when the same detection technique is used with a low-repetition rate laser system, is discussed.

3.1 Transient Pump-Probe Setup

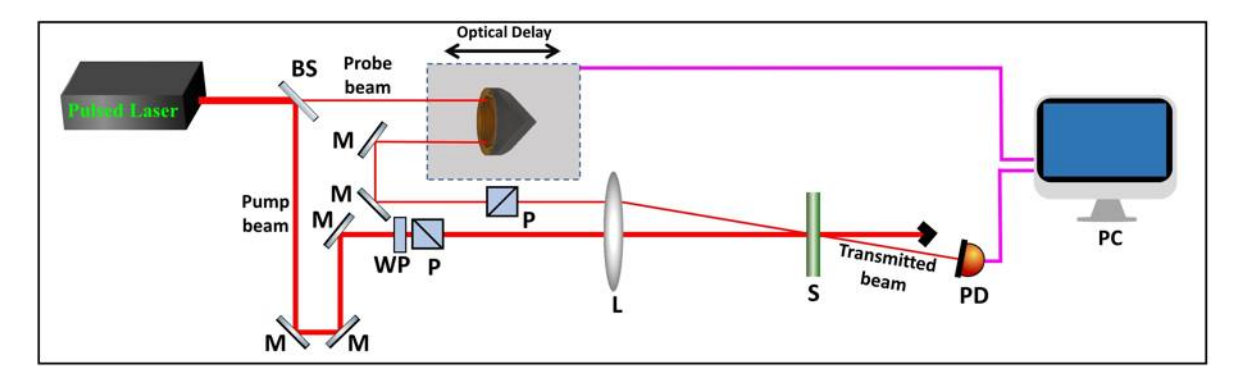


FIGURE 3.1: Schematic of a typical transient pump-probe setup. BS: Beam splitter, M: Mirror, P: Polarizer, L: Lens, S: Sample, PD: Photodetector, WP: Wave plate, and PC: Personal Computer.

The ultrafast optical response investigations are generally made with a beam from a pulsed laser with a pulse-width smaller than the reaction time of the material under study. The schematic of a typical transient transmission setup is shown in Fig.3.1. First, the beam is divided into two parts using a beam splitter (BS). The beam splitting ratio is chosen such that one of the beams has much higher power than the other beam. The stronger pump beam is employed to disturb the sample's state, while the weaker beam probes the altered states. Typically, a pump to probe intensity ratio of at least 10:1 is maintained. By utilizing mirrors, both beams are directed to travel through distinct optical pathways. The total optical path length traveled by these beams is adjusted such that they reach the sample at the same time. Using a lens, these beams are then focused on the same spatial point on the sample. The probe spot diameter should be smaller than the pump diameter at the sample so that the probed regime is uniformly modified by the pump pulse. One of the beams is made to travel through a prism or recto-reflector deployed on a translation stage that serves as an optical delay line before overlapping at the sample place. The time delay between the pump and probe pulses can be controlled by adjusting the stage location. During the transient measurements, the transmitted pump beam is dumped using a beam block.

To find out zero delay and to confirm spatial overlap between the pump and probe pulses, autocorrelation technique is used using second harmonic generation in a BBO crystal. Using this autocorrelation technique, the pulse-width of the laser and also the instrument response function can be measured. After the interaction of the probe pulse with sample, it is detected using a photodetector. Depending on the sample properties, the reflected or transmitted probe beam is used for carrier dynamics studies. The change in the optical response of the sample measured as a function of the pump-probe delay gives information on the evolution of the photogenerated carriers excited in the sample.

Transient transmission measurements can be performed on materials that transmit a detectable probe beam. The transmitted probe beam is detected using a photodetector. The schematic shown in Fig.3.1 is a transient transmission or transient absorption setup.

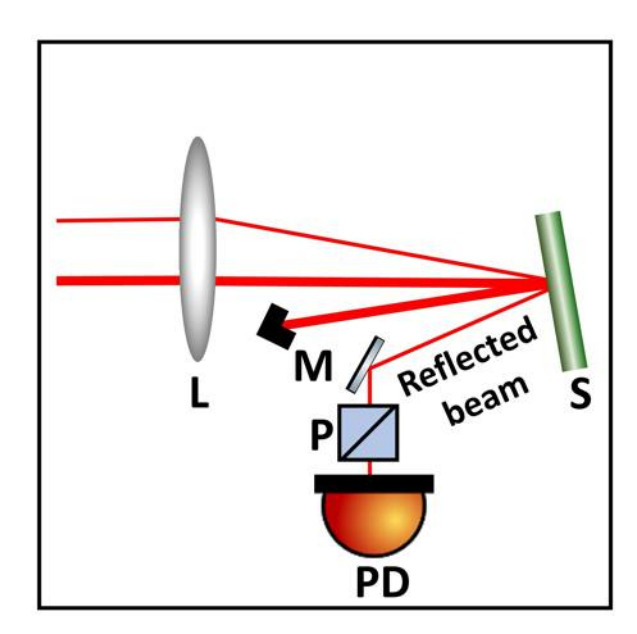


FIGURE 3.2: Schematic of the detection portion of a typical transient reflectivity setup.

For materials through which laser beam can't be transmitted, transient reflection setup is used for the carrier dynamics measurements. Fig.3.2 shows the section

of the pump-probe setup which is utilized for the detection of the change in reflectivity of the sample. To reduce scattered pump beam entering the detector, the pump and probe beams are modified to have orthogonal polarization using appropriate waveplates and polarizers. After reflection, a polarizer that passes the probe beam is also used. This polarizer will improve the S/N ratio in case of degenerate pump-probe by blocking reflected scattered pump light from the sample. For transient spin measurements, additional waveplates and polarizers can be introduced in this same setup for measuring the transient spin dynamics by changing the polarization of the laser pulse.

3.2 Phase-Sensitive Detection Technique

When a material is irradiated with a light pulse, it will absorb part of the light leading to excitation of carriers to their higher energy states. Excited carriers will relax to the ground state through various scattering and recombination processes. Due to the absorption of intense short pulsed light, the absorption coefficient and refractive index of the material gets modified thus the optical properties of the material are different in the excited state from that of the ground state. When the probe pulse falls on the same spot as that of the pump, its reflected or transmitted energy will change depending on the changes in the optical response of the material. To correctly understand the carrier dynamics, it is essential to keep the change induced by the pump to be as minimum as possible [96]. So that, it will not change the property of the sample permanently or damage the material. Due to this, the typical change in transmission or reflectivity of the sample is expected to be very small ($\sim 10^{-3}$ %) to $\sim 10^{-7}$ %). Hence, such measurements need a high S/N ratio [98, 99]. During measurements, different types of noises can contribute to and reduce the S/N ratio. Typical sources of optical noise in such measurements are the fluctuations in the average power of the laser used in the measurement and any other background light which is being detected by the photodetector [100, 101]. In addition to these optical noises, the photodetector or the electronics used for the detection can pickup electrical noises from various sources [102–104]. Since the AC power supply has a frequency of 50 Hz, electronic noise in that frequency will also be generated in the signal. Further ordinary laboratory light sources would produce light at a frequency of 100 Hz (double of 50 Hz). The 1/f electrical noise will dominate at low frequencies. High-frequency switches and RF sources will produce electrical pickup noise at high-frequencies. Although such noises can cause random fluctuations in the signal at any given instant of time, a spectral analysis of the noise would show that most of the noise sources will contribute at different frequencies and their harmonics. Hence, it is necessary to handle these noise sources while measuring the transient processes in a material.

One of the commonly used technique for achieving a high S/N ratio in the pump-probe measurement is the phase-sensitive detection technique which uses a lock-in amplifier [105, 106]. The first step in this technique is to choose a frequency where noise is minimum. In most of the laboratories, such low-noise regime can be found in the kHz range. The main idea of phase-sensitive detection is achieved by modulating the pump beam at the frequency where noise is the lowest. The signal is then measured at the modulation frequency, thus separating extraneous disturbances at various frequencies, resulting in an excellent S/N ratio [106, 107]. Most of the femtosecond oscillators operate at high-repetition rates (for example \sim 80 MHz). Mechanical choppers or electro-optic modulators operating at a few kHz or tens of kHz can be employed in such instances to get a satisfactory S/N ratio in the measurements. The output per pulse energy of most femtosecond oscillators is very low, and the pulse-to-pulse spacing is likewise quite short (12.5 ns for a 80 MHz system). A phase-sensitive detection technique can easily give a S/N ratio of the order of 10^6 to 10^7 .

A schematic of the setup with phase-sensitive detection scheme is shown in Fig.3.3. In this technique, the pump beam is time modulated by up to a few kHz using a mechanical chopper or a few tens of kHz using electro-optic modulators. The reflected or transmitted probe beam is then detected by a photodetector and lock-in amplifier combination. The reference signal is sent by the chopper to the lock-in amplifier for detection at the chopper frequency. The changes in the probe beam cause by the pump beam will be at the chopper frequency. As mentioned

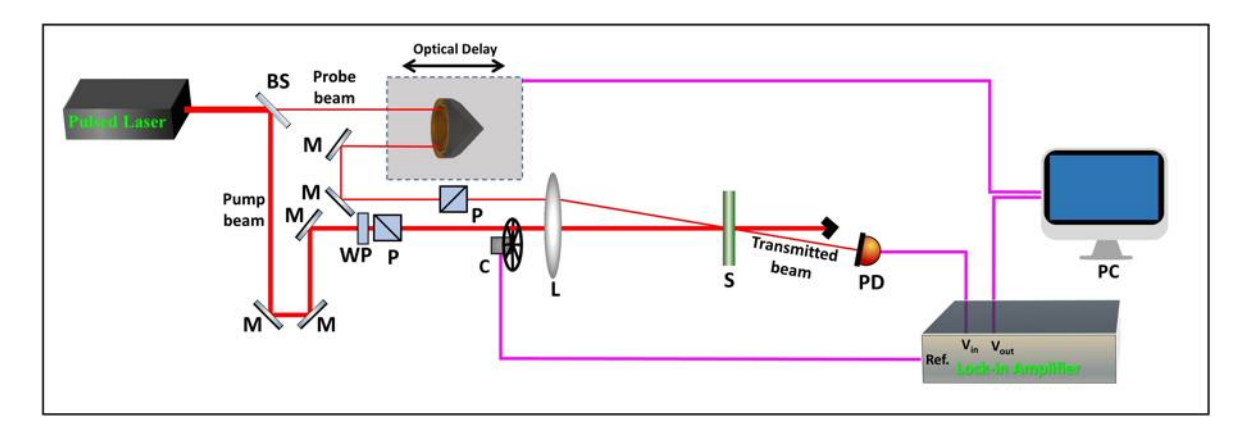


FIGURE 3.3: Schematic of a typical transient absorption setup with phase-sensitive detection scheme. BS: Beam splitter, M: Mirror, P: Polarizer, L: Lens, S: Sample, PD: Photodetector, WP: Wave plate, C: Chopper, LIA: Lock-in amplifier, and PC: Personal Computer.

before, the other electrical and optical noises will have different frequencies since at the beginning of the experiments, the chopper frequency is chosen where noise is low. Now the lock-in amplifier detects the amplitude and phase of the signal at the chopper frequency thus isolating the signal from noise. Once again, the signal from the lock-in amplifier is detected with respect to the delay between the pump and the probe pulse to measure the transient response of the sample.

3.2.1 Theoretical Background: Phase-Sensitive Detection at High-Repetition Rate Laser

Let's consider a standard transient pump-probe measurement performed on a sample using time-synchronized pump and probe pulses (Fig.3.3). In such measurements, the change in the absorption/reflectivity of the sample is first measured at a given delay between the pump and probe pulses and this measurement is then repeated at several other delays to obtain the complete temporal response of the material [101, 108]. Let us consider a situation in which the laser source used in the measurement is highly stable and has a sufficiently high pulse repetition rate. If the response time of the photodetector being used is slow compared to the pulse-to-pulse separation, then the output voltage of the photodetector will be a constant

which is proportional to the average power of the laser beam being detected. Let P_{in} be the average power of the probe beam falling on the front side of the sample (for simplicity reflection losses are neglected in this analysis). The output voltage of the photodetector detecting the transmitted power through the sample can be written as,

$$V_O(t) = CTP_{in} + Re \left[\sum_{\omega_N} V_N(\omega_N) e^{-i\omega_N t} \right], \tag{3.1}$$

where C is a constant which depends on the sensitivity of the photodetector and

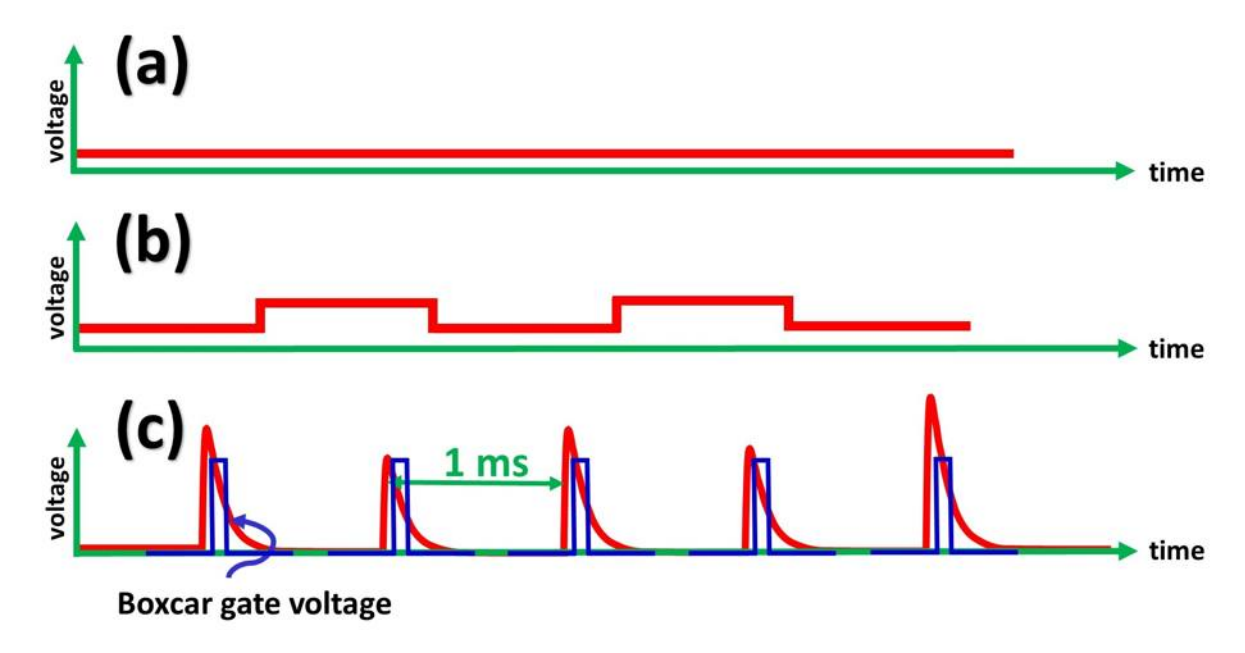


FIGURE 3.4: (*a*) Output voltage of a photodetector when only the probe beam is transmitting through the sample and under no pump condition. (*b*) Output voltage of a photodetector when both pump and probe are transmitting through the sample. (*c*) Output voltage of a 1 kHz pulsed laser system and triggering of the boxcar showing the gate voltage where the transient signal will be measured.

filters that are being used, T is the transmission of the sample. The second term accounts for the systematic and random electrical and optical noises in the measurement expressed in the frequency domain. $V_N(\omega_N)$ is the amplitude of the noise at frequency ω_N . If there was no noise, the detected signal should be a constant as shown in Fig.3.4(a). When the sample is excited by the pump pulse, its optical response changes. For sufficiently small excitation conditions, the change in the

absorption coefficient will be proportional to the third-order nonlinear absorption coefficient [95, 109]. Considering an instantaneously responding sample having a relaxation time much longer than the pulse-width, the absorption coefficient after excitation by the pump pulse can be written as,

$$\alpha(E_P, \tau) = \alpha_0 + \beta(\tau)E_P, \tag{3.2}$$

where α_0 is the linear absorption coefficient, E_P is the energy of the pump pulse, β is related to the third-order nonlinear absorption coefficient with a dimension of α/E_P , and τ is the time between the excitation of the pump pulse and arrival of the probe pulse. It is the temporal evolution of β which finally reveals the carrier dynamics in the sample. For a sufficiently small induced change in the optical response ($\alpha_0 >> \beta E_P$), the transmission of the sample in presence of the pump pulse is given by,

$$T = e^{-\alpha d}, (3.3)$$

$$\approx T_0 \left[1 - \beta(\tau) E_P d \right], \tag{3.4}$$

where T_0 is the linear transmission of the sample having thickness d and is equal to $\exp(-\alpha_0 d)$. The change in the transmission of the sample ($\Delta T = T - T_0$) induced by the pump pulse is given by,

$$\Delta T(\tau) = -T_0 \beta(\tau) E_P d. \tag{3.5}$$

If the pump beam is modulated at a frequency Ω_c , the transmission of the sample will also change at that frequency between $T_0(1 - \beta E_P d)$ (when the pump pulse is falling on the sample) and T_0 (when the pump is blocked). To get a good S/N ratio, the Ω_c has to be chosen such that the electrical and optical noises in the lab are least at this frequency. Thus, the output voltage of the photodetector when the pump beam is modulated is given by,

$$V_O(t) = CT_0 \left[1 - \beta(\tau) E_P \mathcal{G}(t) d \right] P_{in} + Re \left[\sum_{\omega_N} V_N(\omega_N) e^{-i\omega_N t} \right]. \tag{3.6}$$

Here, G(t) is the pump beam modulating function. This output voltage is the same as shown in Fig.3.4(b). Assuming a square wave modulation of the pump pulse, which is typical for the mechanical chopping of the pump beam, the modulating function G(t) can be expressed as a sum of infinite sinusoidal waves given by [110],

$$\mathcal{G}(t) = \frac{4}{\pi} \sum_{k=1}^{\infty} \frac{\sin[(2k-1)\Omega_c t]}{2k-1}.$$
 (3.7)

In a phase-sensitive detection technique, the output of the photodetector is connected to the input of a lock-in amplifier. Using the chopper frequency as the reference signal, the lock-in amplifier will measure the amplitude of the voltage at Ω_c . Substituting Eq.3.7 in Eq.3.6, the output of the lock-in amplifier, V_L , at the frequency Ω_c can be obtained and is given by,

$$V_L(\tau) = -\frac{4C}{\pi} T_0 \beta(\tau) E_P P_{in} d. \tag{3.8}$$

As mentioned earlier, Ω_c is chosen such that there is negligible noise at that frequency, hence $V_N(\Omega_c) \approx 0$. Using Eq.3.5 and Eq.3.8, the transient transmission at the delay, τ , can be written as,

$$\frac{\Delta T(\tau)}{T_0} = \frac{\pi}{4C} \frac{V_L(\tau)}{P_{in} T_0}.$$
(3.9)

A direct measurement of transmitted probe power through the sample using the same photodetector under similar conditions by blocking the pump beam would produce a constant voltage, $V_0 = CT_0P_{in}$, at the output of the photodetector. Using this, Eq.3.9 can now be written as,

$$\frac{\Delta T(\tau)}{T_0} = \frac{\pi}{4} \frac{V_L(\tau)}{V_0}.$$
 (3.10)

Thus, by using the output of the lock-in amplifier (V_L) at various delays and V_0 , the transient transmission through the sample could be measured with a high S/N ratio.

3.3 Low-Repetition Rate Laser System: Noises and High Sensitive Detection Technique

When working with pulsed laser systems with high-repetition rates for example 80 MHz, conventional photodetectors with microsecond response time will give a DC output. An excellent S/N ratio for the transient measurements can then be obtained by chopping the pump beam at a few kHz, which is well away from the laser repetition rate and most of the other sources of noise [109, 111]. However, many samples require greater pump pulse energies to generate adequate probing change, as well as a long pulse-to-pulse separation to allow enough time for the sample to relax.

Femtosecond amplifier systems can deliver much higher energies and usually operate at 1 kHz, corresponding to a pulse-to-pulse separation of 1 ms. When a pump-probe measurement is performed with such beams, the difference between the chopper frequency and laser repetition rate is very small. Further, when the chopper frequency is less than 1 kHz, additional 1/f noise, as well as other undesired electrical and optical noises add up reducing the S/N ratio. When lowrepetition rate lasers are used for pump-probe measurements, the true signal arrives at the photodetector for a very short duration, while the photodetector generates an unwanted signal from dark current, stray light, and other electrical noises for the rest of the time (much longer than the signal duration). The undesired build up of noise can be reduced by measuring the signal just during the moment of pulse arrival and discarding the remaining of the signal from the detector. In such cases, a boxcar could be used for the isolation of signal from noise in time domain. Boxcar is an electrical instrument that can detect the signal from the photodetector at a desired time and create a similar DC voltage at its output for a set period of time. The boxcar can be triggered with a voltage pulse, and a delay between the trigger and signal measurement duration can be controlled by modifying the signal detection duration, the time at which the signal has to be detected from the trigger pulse as shown in Fig.3.4(c). The signal measured by boxcar can also be averaged.

Here, a new detection approach that takes the advantages of both the boxcar and lock-in amplifier equipment strengths is discussed, and it is demonstrated to be particularly beneficial in pump-probe experiments using a low-repetition rate (1 kHz) laser system.

3.3.1 Experimental Details

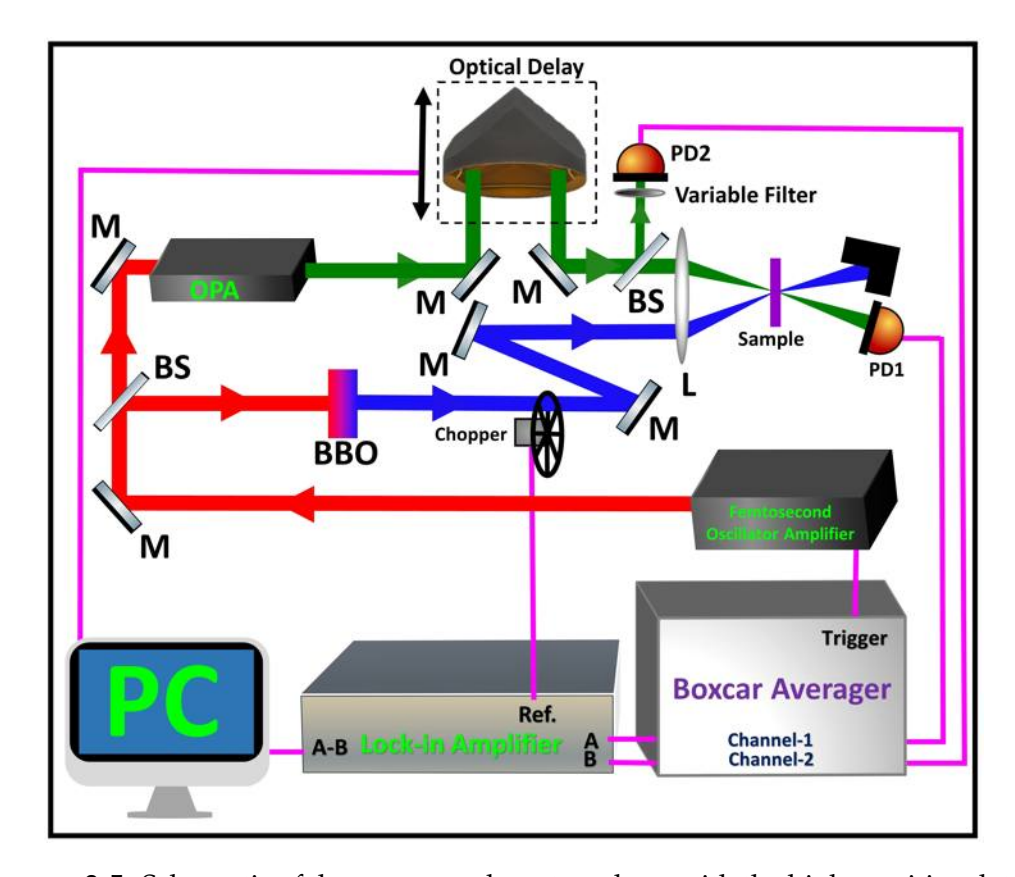


FIGURE 3.5: Schematic of the pump-probe setup along with the high sensitive detection system which combines the advantages both of boxcar and lock-in amplifier. M: Mirror, BS: Beam Splitter, BBO:Beta Barium Borate crystal, and PD:Photodetector.

For the demonstration of this detection technique, pump-probe measurement was carried out on a silver nanoparticle film by exciting at 400 nm and probing at 408 nm. Fig.3.5 shows the schematic diagram of the experimental setup along with the details of the detection scheme. The schematic of the pump-probe setup remains the same as that shown in Fig.3.3 except for the detection of reference, but with a

very different detection scheme which also incorporates a boxcar. The femtosecond oscillator-amplifier system delivers 35 femtosecond, 800 nm pulses at 1 kHz repetition rate. Using a BBO crystal, a portion of the 800 nm amplifier output was frequency-doubled to produce the 400 nm pump pulse. An OPA was pumped using another portion of the amplifier output. The typical standard deviation of the laser pulse-to-pulse energy fluctuation normalized to the average is nearly 3.4%. The output of the OPA when operated at 408 nm was used as the probe beam. The pump and probe pulses were spatially overlapped on the sample using a lens. The temporal delay between the pump and probe pulses is controlled by passing the probe beam through a optical delay line. The transmitted probe power is measured using a normal photodetector (PD_1). The peak change in the voltage pulse generated by the photodetector is proportional to the pulse energy. Due to the design of the PD_1 , this voltage pulse decays nearly exponentially with a time constant of \sim 20 μ s. Using the trigger from the laser timing circuit and by suitably choosing the delay and width of the gate pulse, a boxcar (Stanford Research System SR200 Series) is made to detect nearly the peak change in the photodetector voltage. All the measurements were carried out by operating the boxcar without any amplification and under no averaging condition (which will spoil the signal while being used with a chopper). The output of the boxcar generates a corresponding constant voltage which is now proportional to the laser pulse power. This output is then connected to the input of a lock-in amplifier (Signal Recovery Model 7265). Under no averaging condition, the boxcar output will be a constant voltage that changes at every 1 ms due to the 1 kHz repetition rate of the laser. If the laser pulse-to-pulse energy fluctuation is negligible, the output of the boxcar will be a constant which is now nearly independent of the repetition rate of the laser. Thus by inserting a boxcar in between the output of the PD₁ and lock-in amplifier an experiment performed using a low-repetition rate laser has been converted to a situation which is similar to the constant output obtained from a slow photodetector when exposed to a high-repetition rate laser. In addition, the boxcar can also remove any noise that is time-shifted with respect to the pulse arrival, the sharp electrical pickup noise which occurs due to the pulse switch out process in the laser amplifier. Further, the response time of the photodetector itself would not matter since the boxcar can be made to pick up the signal at a specific

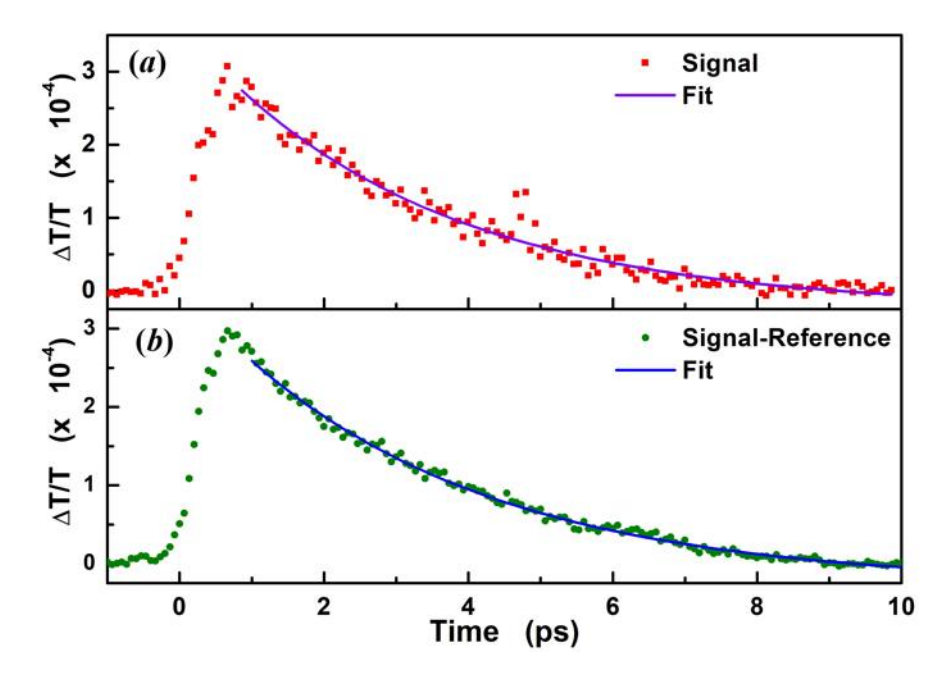


FIGURE 3.6: Measured transient transmission signal of a Ag thin particulate film. (a) The output of PD₁ is detected by boxcar and the output of boxcar is then sensed with lock-in amplifier at chopper frequency, 405 Hz and (b) similar to (a) except that the fluctuation in the signal is further reduced by subtracting a reference probe signal (see the text for details).

time on the output of the photodetector signal.

The pump beam is now chopped mechanically at a certain frequency (Ω_c). If the laser pulse arrives at the chopper when the chopper blade is partially blocking the beam path, the pulse will get cut spatially creating unwanted changes in the pump pulse energy and random beam profile changes. To reduce such noise, the chopper is placed at a location where the diameter of the beam is least. The output of the boxcar is connected to channel-A of the lock-in amplifier. The pump-induced change in the transmission of the sample will modulate the boxcar output at the chopper frequency which can now be detected by the lock-in amplifier as described in section 3.2.

The observed transient transmission of the Ag thin film sample conducted

using the current detection configuration is shown in Fig.3.6(a). The chopper frequency was chosen to be 405 Hz. With the arrival of the pump pulse, the transmission through the sample increases. In Ag nanoparticles, the change in the transmission which is caused by the electron-phonon thermalization recovers in the next few picoseconds [109, 112, 113]. A single exponential fit to the decay part of the signal gives a decay time of 3.3 ± 0.2 ps. Such transient response is typical for metal nanoparticles.

In order to study the statistical variation in the signal among various pumpprobe detection parameters, the signal at the peak of the transient transmission (\approx 0.5 ps) was recorded repeatedly. Then an estimation for the statistical variation (S_D) in percentage is calculated using,

$$S_D = 100 \times \sqrt{\frac{1}{N} \sum_{i=1}^{N} \left(\frac{S_i}{S_{av}} - 1\right)^2},$$
 (3.11)

where N is the number of data points, S_i represents the individual measured data and S_{av} is the average defined by,

$$S_{av} = \frac{1}{N} \sum_{i=1}^{N} S_i. {(3.12)}$$

Since the data is normalized to the average, a lower value of S_D implies a good S/N ratio. The S_D estimated for the signal measured at the peak of $\Delta T/T$ shown in Fig.3.6(a) is 27 (N = 100).

If the pulse-to-pulse power fluctuation in the laser is negligible, the collected data can be considered similar to that of a standard transient transmission measurement performed using a high-repetition rate laser. In general, femtosecond amplifier systems have much lower pulse-to-pulse energy stability than oscillators. Thus, the transient signal measured using this low-repetition rate oscillator-amplifier-OPA system will have additional noise due to pulse-to-pulse energy fluctuation. In the following, we show, first theoretically and then experimentally the effect of such pulse-to-pulse energy variation on the S/N ratio and a method to counter it.

Let the average pulse energy of the probe pulse at the input of the sample be E_{in} with a random pulse-to-pulse energy fluctuation, ΔE_{in} . The value of ΔE_{in} would change at every 1 ms in a 1 kHz repetition rate system. The distribution of ΔE_{in} for an ensemble of pulses would be a Gaussian, which is typical for the type of laser used in the present measurement. The voltage output of the boxcar channel which is detecting the transmitted probe pulse through the sample using PD₁ is,

$$V_O^B(t) = C^B T \left[E_{in} + \Delta E^{in} \mathcal{H}(t) \right] + Re \left[\sum_{\omega_N} V_N^B(\omega_N) e^{-i\omega_N t} \right], \tag{3.13}$$

where C^B is a constant which depends on the sensitivity of the PD₁ and gain in the boxcar. V_N^B is the amplitude of electrical and optical noise at frequency ω_N . Once again, for small change in the transmission of the sample in presence of the pump pulse (E_P) modulated by a function $\mathcal{G}(t)$, the output of the boxcar can be written as,

$$V_{O}^{B}(t) = C^{B}T_{0} \left[1 - \beta(\tau)E_{P}\mathcal{G}(t)d\right] \left[E_{in} + \Delta E_{in}\mathcal{H}(t)\right] + Re\left[\sum_{\omega_{N}} V_{N}^{B}(\omega_{N})e^{-i\omega_{N}t}\right].$$
(3.14)

Here, $\mathcal{H}(t)$ is a unit step function which repeats with the arrival of probe the pulse.

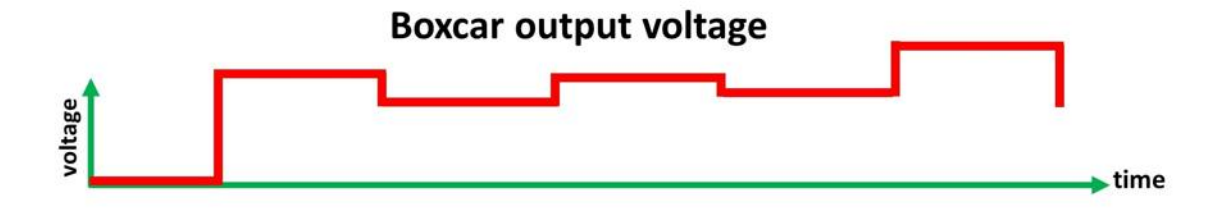


FIGURE 3.7: Output voltage of boxcar when the gated laser pulse is measured.

Since ΔE_{in} varies randomly depending on the energy of each probe pulse, the product of ΔE_{in} and $\mathcal{H}(t)$ will be composed of several frequencies and can also have a component at the chopper frequency. The output voltage of a typical boxcar is shown in Fig.3.7.

For sufficiently small fluctuations in the probe energy $\Delta E_{in} << E_{in}$, the term containing the product of β and ΔE_{in} in Eq.3.14 can be neglected when compared to the other terms. Thus the output of the lock-in amplifier which is now detecting the boxcar output in channel-A can be written as,

$$V_L^B(\tau) = -\frac{4C^B}{\pi} E_{in} T_0 \beta(\tau) E_P d + \Delta E_{in} \mathcal{F}(t) C^B T_0, \tag{3.15}$$

where $\mathcal{F}(t)$ is the amplitude of Fourier transform of $\Delta E_{in}\mathcal{H}(t)$ at the chopping frequency and it depends on time because of the slow variations in laser pulse energy. Note that the second term in the Eq.3.15 does not depend on the $\beta(\tau)$ of the sample, however, depends directly on the pulse-to-pulse fluctuation. Thus, due to shot-to-shot energy fluctuation in the probe, additional noise (given by the second term in Eq.3.15) will get added to the required signal, the first term. The $\Delta T/T$ presented in Fig.3.6 will have fluctuations caused by the random probe energy variation.

For removing this noise a small part of the probe beam can be reflected before it enters the sample and can be detected using another photodetector (PD₂). The output of this reference photodetector can also be processed by another channel of the boxcar. The output of the boxcar can then be written as,

$$V_O^{B2}(t) = C^{B2}T_f R \left[E_{in} + \Delta E_{in} \mathcal{H}(t) \right] + Re \left[\sum_{\omega_N} V_N^{B2}(\omega_N) e^{-i\omega_N t} \right], \tag{3.16}$$

where C^{B2} is a constant which depends on the sensitivity of the second reference photodetector, PD₂, and gain of the boxcar. R is the reflectance of the beam splitter used for obtaining the reference beam and T_f is the transmission of the filter used before PD₂. Using a variable filter, T_f was chosen such that $C^{B2}RT_f = C^BT_0$ (one can also change the gain in the boxcar channel by detecting the output of PD₂). This can be easily done directly by monitoring the boxcar outputs $V_O^B(t)$ and $V_O^{B2}(t)$ in an oscilloscope and making them almost equal. This voltage $V_O^{B2}(t)$ is then subtracted from the boxcar output of PD₁ ($V_O^B(t)$) electronically before feeding into the lockin amplifier. Most of the commercial lock-in amplifiers do come with a provision for such subtraction (channel B) of voltage which could be directly used for this

subtraction purpose. The output voltage after subtraction (A-B) can be written as,

$$V_O^D(t) = -C^B T_0 \beta(\tau) E_P \mathcal{G}(t) d \left[E_{in} + \Delta E_{in} \mathcal{H}(t) \right]$$

$$+ Re \left[\sum_{\omega_N} (V_N^B - V_N^{B2}) e^{-i\omega_N t} \right].$$
(3.17)

The output of the lock-in amplifier which is now detecting the $V_{\mathcal{O}}^{D}(t)$ using the chopper frequency as a reference will be,

$$V_L^B(\tau) = -\frac{4C^B}{\pi} E_{in} T_0 \beta(\tau) E_P d. \tag{3.18}$$

A direct measurement of transmitted probe pulse energy through the sample using PD₁ under similar conditions through the boxcar by blocking the pump beam would produce a constant voltage, $V_D^B = C^B T_0 E_{in}$, at the output of the boxcar. Now using Eq.3.5 and the measured V_D^B , the transient transmission through the sample can be estimated by,

$$\frac{\Delta T(\tau)}{T} = \frac{\pi}{4} \frac{V_L^B(\tau)}{V_D^B}.$$
 (3.19)

It is important to note that in the present technique, usage of an identical balanced detector is not essential as done in several earlier reports. Normal photodetectors can be used for measuring the reference and signal to reduce the noise due to probe energy fluctuations. Only the DC output of the boxcar needs to be made equal $(V_O^B(t) = V_O^{B2}(t))$.

Fig.3.6(b) shows the measured transient transmission signal of the metal thin film sample performed by the A-B configuration. A single exponential fit to the decay part of this signal gives a decay time of 3.5 ± 0.1 ps. The S_D of the signal measured at the peak change in the present case is 10, which is nearly one-third of that when the signal measured without subtraction of the boxcar output of PD₂ from that of PD₁.

TABLE 3.1: The dependence of S_D and peak-to-peak variation in the signal at different chopper frequencies Ω_c around 333 Hz.

$\overline{\Omega_{c}}$	S _D (%)	Peak-to-Peak fluctuation (%)
230	15.5	95.3
280	13.9	56.6
333	2.9	14.5
380	11.5	44.6
420	11.6	61.2

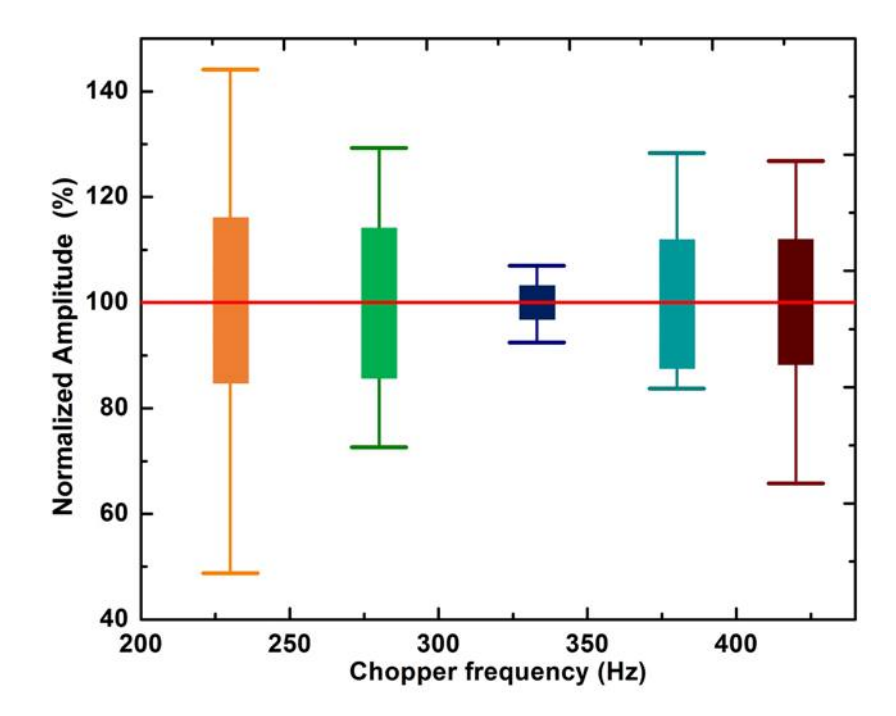


FIGURE 3.8: The dependence of the fluctuations in the normalized signal measured at peak position in A-B configuration on the chopping frequencies around 333 Hz. The height of the rectangular box represents the S_D and the maximum and minimum signal values in the data set are also shown as bar.

To further reduce the statistical fluctuations in the measurements, chopper frequency dependent studies were carried out on the same sample. The transient signal at the delay where the peak occurs is recorded repeatedly in the A-B configuration (N is \sim 100) at various chopper frequencies. The statistical variations in the peak signal as given by Eq.3.11 was estimated at each chopper frequency and are given in Table.3.1. Further apart from S_D , it is also important to know about the maximum and the minimum signal obtained of the measured data to understand

TABLE 3.2: The dependence of S_D and peak-to-peak variation in the signal at different chopper frequencies which are factors of 1 kHz.

$\overline{\Omega_{c}}$	S _D (%)	Peak-to-Peak fluctuation (%)
200	12.0	52.8
250	9.8	46.2
333	2.9	14.5
500	12.0	58.0

the stability in the measured signal. Fig.3.8 shows the variation of S_D on the chopping frequencies as a solid rectangle. Fig.3.8 also shows the measured maximum and minimum signal values among the data set at each chopper frequency as bars. Clearly, the S_D is least for the chopper frequency 333 Hz. As the chopper frequency deviates away from 333 Hz, we find that the S_D and the peak-to-peak variation in the signal also increase.

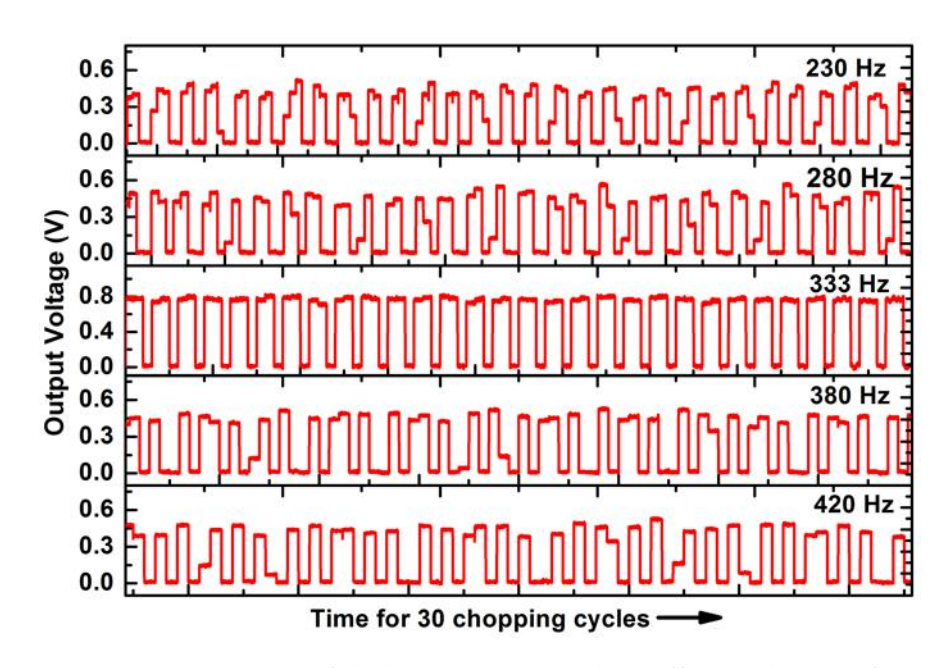


FIGURE 3.9: Output voltage of the boxcar measured at different chopper frequencies close to 333 Hz. The time in the horizontal axis at each chopper frequency is chosen such that there are 30 chopping cycles in view.

When the laser pulse repetition rate is very large compared to the chopper frequency, the number of laser pulses blocked or unblocked in each cycle would remain nearly the same. On the other hand, when the laser repetition rate and the chopper frequency are close, an temporal aliasing process can lead to frequent

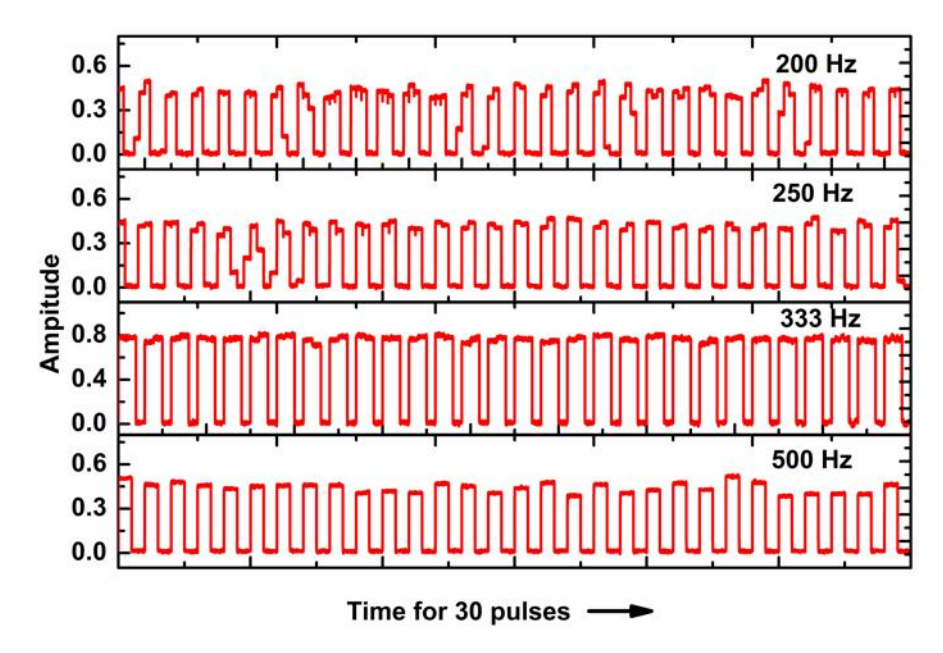


FIGURE 3.10: Output voltage of the boxcar measured at chopper frequencies which are harmonics of 1 kHz. The time in the horizontal axis at each chopper frequency is chosen such that there are 30 chopping cycles in view.

changes in the number of pump pulses that are getting passed through the chopper. To measure the effect of chopper on the pump pulses, we have directly measured the energy of the pump pulses after passing through the chopper. Fig.3.9 shows the output of the boxcar measuring the output of the photodetector detecting the modulated pump pulses passing through the chopper for 30 cycles. Here zero amplitude means that the chopper had blocked the pulse while the higher amplitudes correspond to the energy of the pulses passing through the chopper. Clearly, the pump pulses are getting partially blocked by the chopper at frequencies other than 333 Hz. These phenomena can also be explained as follows. Chopper frequency 333 Hz is nearly a factor of the laser repetition rate, 1 kHz. Thus in each chopper cycle, two pulses are passed and one pulse is blocked and the process repeats (the reverse, two pulses are blocked and one pulse is passed is also possible depending on the starting time of the chopper). On the other hand, if the chopper frequency is such that it is not a factor of laser repetition rate then frequently the chopper blade would be in a partially closed or partially open condition during the pulse arrival. Such partial cutting of pump pulse would lead to strong changes in the pump energy as well as spatial shape distortion of the beam profile at the sample place. Since the transient signal is proportional to the pump pulse energy (see Eq.3.18), these variations would cause the signal to fluctuate. Thus, 333 Hz is one of the possible factors of 1 kHz which can have the least fluctuation in the signal as well as the least variation in peak-to-peak energy. Hence, to avoid such chopping generated modulations in the pump pulse, it is essential to choose a chopper frequency which is a factor of the laser repetition rate.

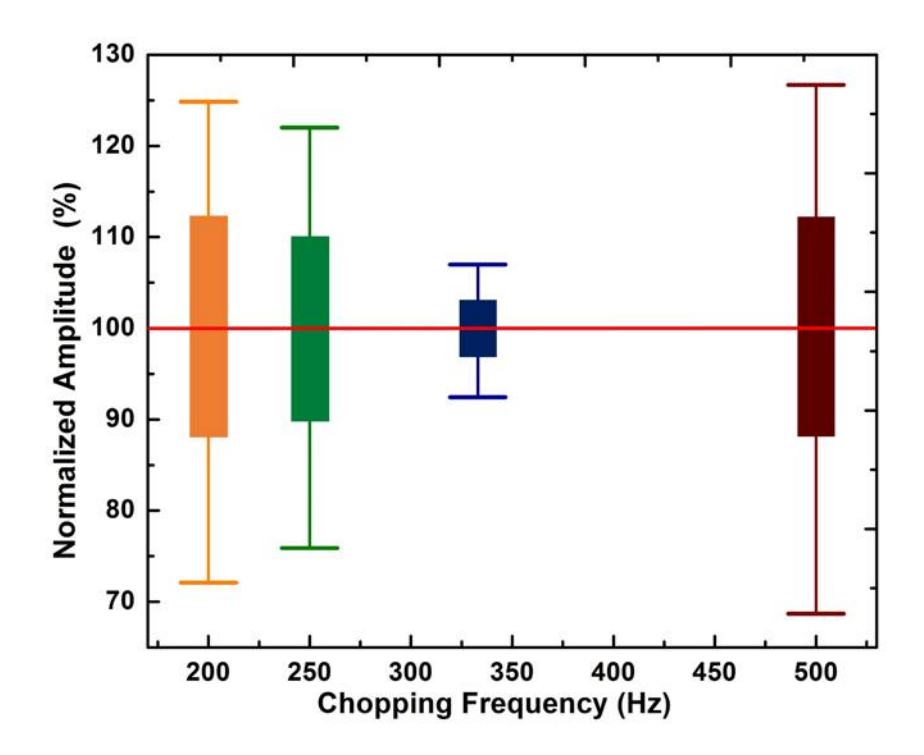


FIGURE 3.11: The dependence of the fluctuations in the normalized signal measured at peak position in A-B configuration on the chopping frequencies which are factors of 1 kHz. The height of the rectangular box represents the S_D and the maximum and minimum signal values in the data set are also shown as bar.

We have also performed similar measurements at all the chopper frequencies which are factors of 1 kHz in the A-B configuration. The statistical variation in the peak signal is given in Table.3.2. Fig.3.11 shows the dependence of S_D and the measured maximum and minimum signal values on the harmonic chopping frequencies which are factors of 1 kHz. Fig.3.10 shows the output of the boxcar voltage at chopper frequencies which are harmonics of 1 kHz repetition rate of the laser. Once again, the S_D at the chopper frequency 333 Hz is the least. Although the chopper

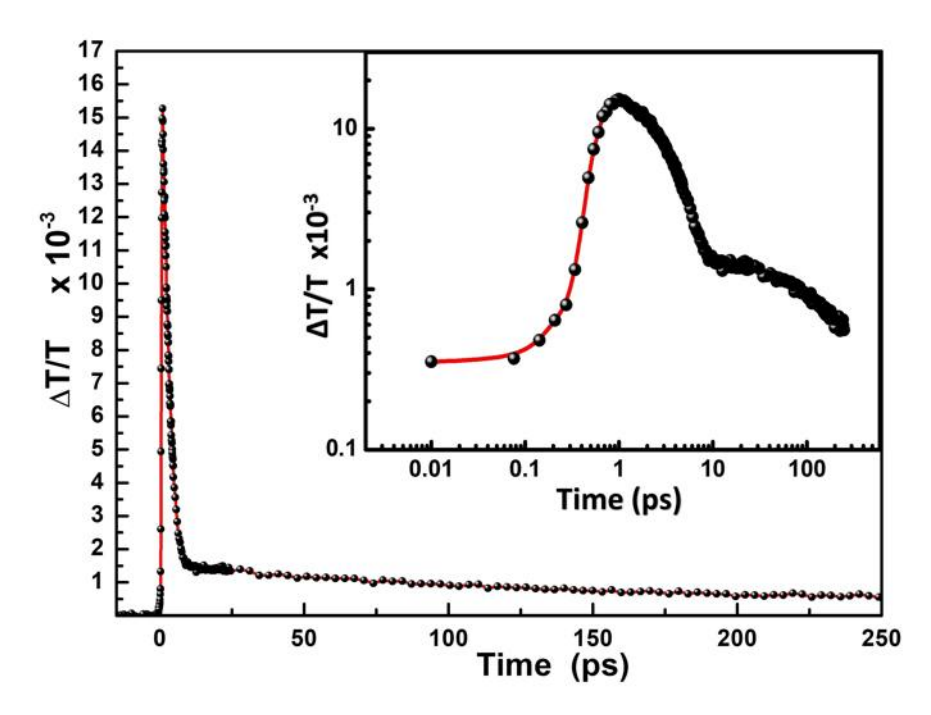


FIGURE 3.12: A typical transient absorption signal measured with 333 Hz chopping. Inset shows the same curve in log-log scale.

frequencies, 200 Hz, 250 Hz, and 500 Hz are factors of 1 kHz still the noise at these frequencies are much higher than that of 333 Hz. The pump-probe measurements performed at very low chopper frequencies like 50 or 100 Hz (factors of 1 kHz) will result in increasing the shot-to-shot fluctuations leading to an even lower S/N ratio. The AC power supply frequency which is being used in the experiment is 50 Hz and the on-off frequency of most of the laboratory light sources driven by this AC power supply is 100 Hz. Thus, because of any kind of stray light present in the lab, it is well known that 50 Hz, 100 Hz, and their higher harmonics are all not suitable for chopping frequencies. When chopped at these frequencies, the lock-in amplifier will sense these electronic noises or the other light which are being detected by the photodetectors. Since the chopping frequencies 200 Hz, 250 Hz, and 500 Hz are all higher harmonics of 50 Hz and 100 Hz, the signal detected at these frequencies will have higher noise compared to that at 333 Hz. Several earlier reports used 500 Hz or various other chopping frequencies for the measurement of pump-probe signal with 1 kHz system [114]. Our result suggests that when 1 kHz laser system is used, for the best S/N ratio, the pump should be chopped at 333 Hz.

Further, even in the case where only a lock-in amplifier is used in the measurement, the chopping has to be done at 333 Hz. Although the technique reported here takes care of the fluctuations in data caused by the probe energy variation, still the variations in pump energy would cause the signal to vary (Eq.3.18). Fig.3.12 shows the transient absorption signal measured on a silver nanoparticle sample under fully optimized conditions and averaged over 8 measurements at each delay. In such a long delay range, a second slow decay in the transient signal which is due to the phonon-phonon interaction can also be clearly identified (see the inset of Fig.3.12) [109, 112]. Further, we also find that the gain in the boxcar could also be used to increase the signal without much change in the S/N ratio.

3.4 Pump-Probe Setup Developed for Transient Measurements in 2D MoS₂

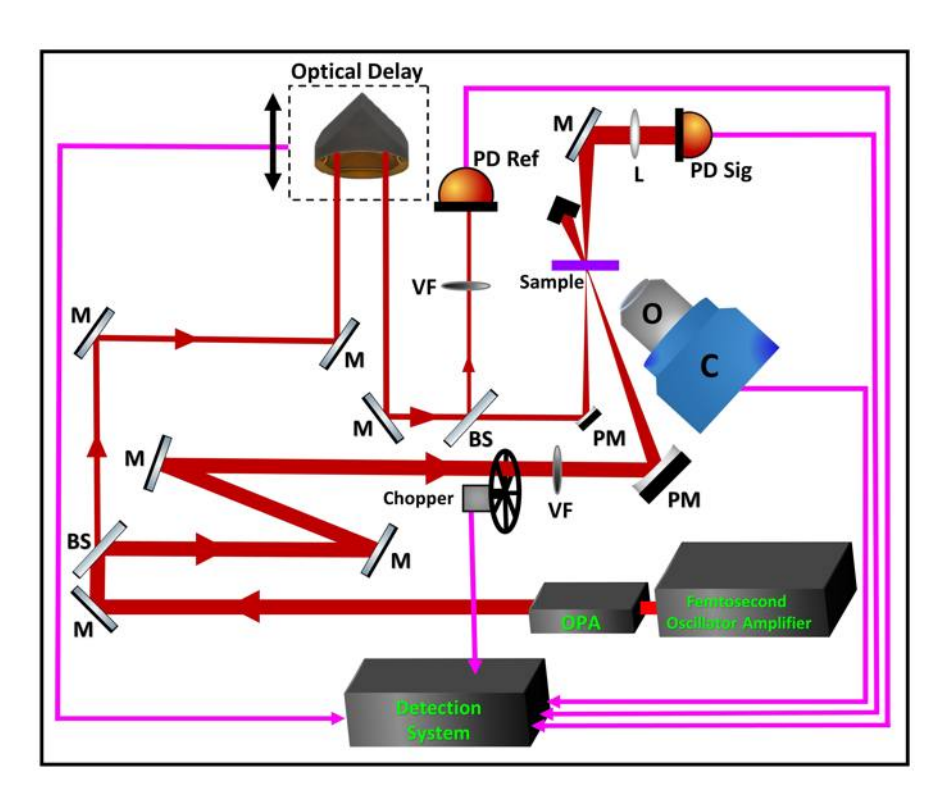


FIGURE 3.13: Schematic of the pump-probe setup developed for the transient measurements in the 2D MoS₂ samples. BS: Beam Splitter, C: CCD camera, L: Lens, M: Mirror, O: Objective, PD: Photodiode, PM: Parabolic Mirror, and VF: Variable Filter.

The above discussed pump-probe setup was developed for the measurements on large samples (more than hundreds of micrometer size) using the Oscillator-Amplifier-OPA system with a lens as the focusing element. Since we have to work with a single-layer MoS₂ flake which has dimensions in between 20 μ m to 100 μ m, we have to develop a setup which can measure the transient signal of such small ML MoS₂ flakes. Again, there are some physical processes that can happen within 100 fs time scale for which the pulse-width of the pulses have to be reduced at the sample location. For this purpose, we have developed a pump-probe setup with mostly reflective optics. Fig.3.13 shows the schematic of the setup developed for the transient measurements in 2D MoS₂. In this setup, two parabolic mirrors are used to focus the pump and probe beams on the sample. The full width at half maximum (FWHM) of the pump and probe beams at the sample place were measured to be nearly 24 μ m and 72 μ m, respectively. The pulse-width at the sample place was measured using the second-harmonic autocorrelation technique and is ~ 60 fs. Besides this, another setup was developed using a 50X objective, a CCD camera, and a white light source to view and identify the flakes for performing the transient measurements. This setup was used to identify whether the pump and probe beams are focused on the correct MoS₂ flake. This pump-probe setup along with the detection scheme developed for low-repetition rate laser was used for the measurement of the transient response of the 2D MoS₂ samples.

3.5 Summary

In this chapter, various pump-probe setups that can be used in a typical carrier dynamics measurement along with the types of noises that can affect the measurements were discussed. A phase-sensitive detection technique which is commonly used in the detection of small changes in a sample induced by pump pulse with a high S/N ratio along with suitable theoretical background is described. Additional sources of noise that reduce the S/N ratio during the pump-probe measurement with low-repetition rate laser system are discussed. A high sensitive detection

technique has been demonstrated which can be used for high S/N ratio with low-repetition rate laser. In this detection scheme, advantages of both boxcar and lock-in amplifier are combined for improving the S/N ratio. A theoretical model was developed to explain the process of signal detection. The pump-probe setup developed for the transient measurements in the small MoS_2 samples is also discussed.

Chapter 4

Ultrafast Carrier Dynamics in a Two-Dimensional MoS₂ Monolayer near A-exciton

Understanding the behavior of the carriers in ML MoS₂ under various excitation conditions is essential for utilizing it in further applications. As discussed in the chapter 1, ML MoS₂ possesses three excitonic transition energies corresponding to A, B, and C-excitons in the visible region. Among these, A-exciton has the lowest transition energy. As a result, any carriers excited in the ML MoS₂ will relax to the A-exciton state and finally recombine with the holes resulting an intense photoluminescence [4, 54]. Thus, studies carried out to understand the formation, dissociation, and carrier dynamics at A-exciton state are crucial for the optoelectronic applications of ML MoS₂.

While studying the transient response, the relaxation process that happens during the first few picoseconds of an excited carrier is essential to understand the subsequent evolution of carrier dynamics and the properties of materials. Several groups have measured the initial ultrafast response of MoS₂ at excited charge density (N_{ex}) in the range of $\sim 10^{10}$ cm⁻² to $\sim 10^{14}$ cm⁻² or equivalently pump fluence ranging from $\sim 0.3~\mu \text{Jcm}^{-2}$ to $\sim 1.5~\text{mJcm}^{-2}$, [27–33, 35–42, 50–55, 63]. Although,

there are overlaps among the regimes in which various processes are anticipated to occur, the relaxation in the initial few picoseconds of time can be categorized roughly into three regimes. For N_{ex} in the range of 10^{10} cm⁻² to $\sim 10^{11}$ cm⁻², the initial rapid decline of the observed optical response is ascribed to the relaxation of excitons via defect states [27, 28] and Auger-based recombination assisted by defect states [34–37]. At excitation densities in the range, $\sim 10^{11}~\rm cm^{-2}$ to $\sim 10^{13}~\rm cm^{-2}$, exciton-exciton annihilation [29-33], defect recombination [54], and carrier cooling through the emission of phonons [38-42] are found to play a strong role in the relaxation. At excitation densities higher than $\sim 10^{13}~{\rm cm}^{-2}$ known as the Mott density of ML MoS₂ [39, 54], the interaction between carriers becomes weaker due to screening of Coulomb interaction and repulsive interaction. Hence, the exciton-exciton annihilation process becomes insignificant [21, 32, 51, 54, 115]. There are relatively few studies carried out at this high excitation regime [41, 52, 53], but limited to a maximum of 2×10^{14} cm⁻², [50]. These studies reveal that the relaxation of the carrier occurs via carrier-capture by defect states [27, 28, 54], defect-assisted Auger excitation [36, 37], and by hot-photon emission [38, 39].

The contribution of any given physical process to the optical response depends strongly on the excited carrier density. For a thorough knowledge of the material, it is necessary to measure the dependence of various time constants on excitation densities and comprehend the related physical processes. Hence, such ultrafast carrier dynamics studies at high excitation densities are relevant in the case of ML MoS₂ for its applicability in devices that handle high carrier densities [43–46].

In this chapter, we report the work carried out to understand the ultrafast carrier dynamics in a single ML MoS₂ by exciting carriers at A-exciton wavelength at carrier density in the range of $\sim 0.66 \times 10^{14}$ cm⁻² to 4×10^{14} cm⁻². At this experimental condition, though the carriers are excited to the A-exciton state, still the fluence and time dependence of transient absorption show that the excitons are getting dissociated forming hot carriers. It will be shown that an initial fast bandgap renormalization (BGR) is observed which swiftly changes to bleaching within the

first few picoseconds[†]. This BGR effect is ascribed to the free carrier creation by exciton dissociation. When a significant percentage of the carriers recombine and the remaining carriers produce excitons, bleaching of this state takes over changing the sign of the observed transient response. Further, it will also be shown that at later times these carriers relax to form longer lived A-excitons at high excitation fluences indicating a bottlenecking process§. The carrier dynamics of ML MoS₂ are split into two time frames in this chapter. The first is a short time scale, in which the initial BGR, the transition from BGR to band bleaching, and the time scale for the entire process are explained. The second is the long-time scale, in which detailed fitting of the data to uncover the action of BGR, the build-up of band bleaching, and the pump fluence dependence of decay constants are discussed.

4.1 Transient Transmission near A-exciton

The transient transmission response ($\Delta T/T$) of the ML MoS₂ sample near A-exciton wavelength was measured at various pump fluences and is shown in Fig.4.1 (note that we have plotted $-\Delta T/T$ in the y-axis). With the arrival of the pump pulse, the transmission through the sample reduces reaching its maximum change within the duration of the pump beam. As the delay between the pump and the probe pulse increases, the magnitude of change in $\Delta T/T$ ($|\Delta T/T|$) reduces. With a further increase in delay, the change in transmission starts recovering. For a fluence of 1.2 mJcm⁻², the transmission through the sample recovers fully ($\Delta T/T=0$) within the first few picoseconds. As the pump fluence increases the magnitude of the initial negative peak also increases. At higher fluences, although the $\Delta T/T$ recovers to zero, it changes sign and becomes positive, reaching a maximum near about 3 ps. At later times, this positive signal also decays nearly exponentially to zero in tens

[†]This work is published by the author of this thesis as "Ultrafast carrier dynamics in a monolayer MoS₂ at carrier densities well above Mott density", **Durga Prasad Khatua**, Asha Singh, Sabina Gurung, Salahuddin Khan, Manushree Tanwar, Rajesh Kumar, and J. Jayabalan, Journal of Physics Condensed Matter 34, 155401 (2022).

[§]This work is published by the author of this thesis as "Excitation density dependent carrier dynamics in a monolayer MoS₂: exciton dissociation, formation and bottlenecking", **Durga Prasad Khatua**, Asha Singh, Sabina Gurung, and J. Jayabalan, Micro and Nanostructures 165, 207205 (2022).

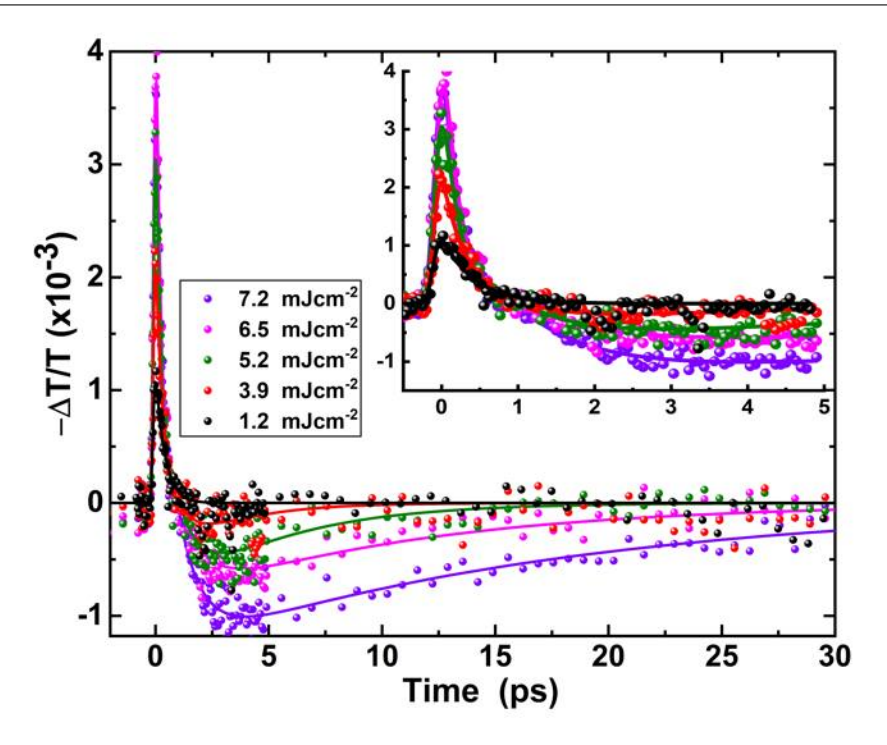


FIGURE 4.1: Fluence dependent transient transmission signal of the selected ML MoS_2 flake at A-exciton peak (note the negative sign of the y-axis). Inset shows the same plot zoomed over the first few picosecond time scale. The corresponding solid color lines are the best fit to the data using Eq.4.2.

of picoseconds time scale. It is evident from this transient data that when carriers are excited near A-exciton, they go through a series of processes before returning to their initial state. Within 1 ps, they respond differently, and physical processes in the sample are altered between 2 ps and 30 ps. As a result, understanding the transient properties requires a close investigation of the carrier's activity in the sample. As a consequence, we split the entire time scale into two categories. The first one will address transient properties that occur within the first few picoseconds. Later, the processes that occur over a long period of time will be discussed.

4.1.1 Transient Transmission of ML MoS₂ within First 5 ps

In Fig.4.2(a), transient response of the ML MoS₂ at first few picoseconds time scale is shown. At lower pump fluences, i.e. $< \sim 4$ mJcm⁻², the $|\Delta T/T|$ nearly recovers to zero by about a few picoseconds. With the increase in the pump fluence,

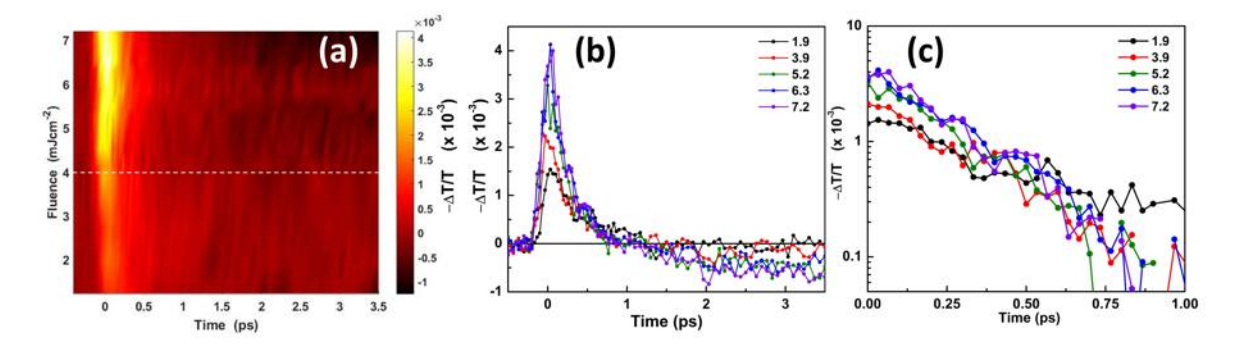


FIGURE 4.2: Transient transmission signal measured on the ML MoS₂ flake at its A-exciton peak at various pump fluences (note the negative sign of the $\Delta T/T$ in the plot): (a) 2D pseudocolor image of the transient transmission data expressed in $\Delta T/T$ as a function of both pump fluence and delay time, (b) some representative plots of transient transmission signals at few fluences. The legend shows the pump fluences in mJcm⁻², and (c) the same transient signal in log scale zoomed at the first one picosecond delay regime.

the maximum change in $|\Delta T/T|$ also increases. At higher fluences (> 4 mJcm⁻²), the $\Delta T/T$ recovers and becomes zero by about 1.2 ps (Fig.4.2(b)). However, with further delay, the sign of $\Delta T/T$ changes. This positive $\Delta T/T$ recovers in tens of picoseconds time scales. Fig.4.2(c) shows the variation of $\Delta T/T$ in the first one picosecond delay time in log scale. The linear variation of the logarithm of $\Delta T/T$ with delay clearly indicates that the decay could well be approximated to a single exponential in this temporal regime. At 1.2 mJcm⁻², the decay time of this fast initial recovery (τ_f) was estimated to be nearly 0.4 ps. To quantitatively understand the dependence of $\Delta T/T$ on fluence, the variation of the peak change in the magnitude of transmission ($(\Delta T/T)_{pk}$) and τ_f were estimated from the time dependence (Fig.4.2(a)). Fig.4.3(a) shows the dependence of $(\Delta T/T)_{pk}$ on the pump fluence. We find that the ($\Delta T/T$)_{pk} increases linearly with the pump fluence indicating that contribution from higher-order nonlinearities or saturation of signal are negligible. Fig.4.3(b) shows the fluence dependence of the τ_f , which is nearly constant and independent of the pump fluence in the present fluence range.

When excited by an ultrafast pulse of photon energy higher than the bandgap, carriers are excited from the filled valence band to the conduction band of MoS₂. As discussed earlier, several groups have studied the initial recovery of the change in the ultrafast optical response of MoS₂ and demonstrated the physical processes

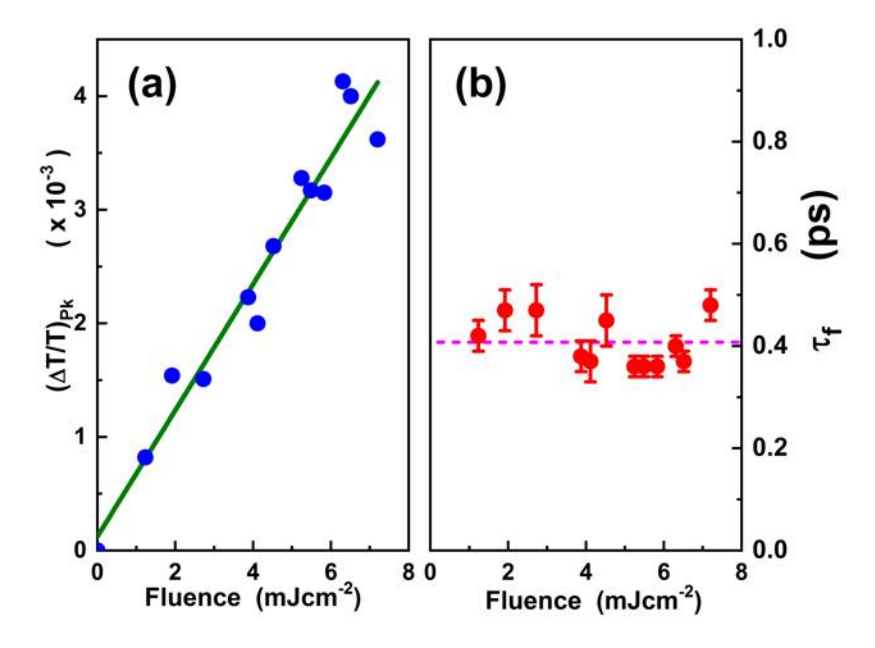


FIGURE 4.3: (a) Variation of the peak change in the magnitude of $\Delta T/T$ with pump fluence extracted from the 2D plot shown in Fig.4.2(a). The linear fit to the experimental points is also shown as a solid line. (b) Shows the fluence dependence of the initial fast decay time. The average decay time is shown as a dotted line.

which produce the observed changes [27–42, 50–55]. Various processes like carrier decay to defect states [27, 28, 54], defect-assisted Auger recombination [34–37], excited-state absorption [51], exciton formation [40–42], exciton-exciton annihilation [29–33], hot-carrier cooling [38, 39], etc. are expected to follow after the excitation of carriers. These processes will lead to band filling [67], bleaching [116], bandgap renormalization [67, 69], valence band broadening [55], exciton peak shift and its broadening [30, 51, 117], etc. These processes modify the optical response of the material at the probe wavelength. The contribution of each of these processes in a given measurement for a given material depends on the wavelength of the pump and probe and also on the pump fluence.

In the present case, we have excited the ML MoS₂ with a wavelength tuned to the A-exciton, thus the pump pulse will directly create primarily A-excitons [51, 69]. Further, N_{ex} is much above the Mott density, hence exciton-exciton annihilation process cannot explain the observed relaxation of the signal [29, 31, 32]. The density of defects in ML MoS₂ is expected to be of the order of 10^{13} cm⁻² - 10^{14} cm⁻², [118–120]. Thus, a portion of the excitons will relax via defect states causing the initial

decay in the signal [27, 54, 67]. However, at the maximum excited carrier densities used in the present experiment (4 \times 10¹⁴ cm⁻²), defect states should have been saturated. Further, if the carriers excited to the conduction band are further getting excited by the pump, it should have shown a nonlinear variation in the fluence dependence of $(\Delta T/T)_{pk}$. Wang et al. and Brasington et al. observed excitation of carriers from defect states to deep into the conduction band [36, 121]. However, at the maximum excited carrier densities used in the present experiment (4 \times $10^{14}\,$ cm⁻²), defect states should have been saturated increasing the life time of carriers. This is due to the fact that the number of defects in the sample is expected to be lower than that of the excited carriers at these fluences. On the other hand, the linear relation between fluence and $(\Delta T/T)_{vk}$ in the experiment, as shown in Fig.4.3(a), clearly shows that there is no saturation or any higher-order nonlinear process. Hence excited-state absorption or further absorption from defect states cannot fully explain the observed transient signal. Moreover, since carriers are directly excited to A-exciton, further relaxation of carriers by intraband carrier decay cannot also happen in the present case. At high densities, excitons are shown to dissociate to form free carriers [38, 39, 52, 54]. Following such dissociation, the presence of a large number of carriers will lead to the BGR process [55, 116]. This process reduces the bandgap and will increase the absorption at lower wavelengths [55, 116]. In few-layer MoS₂, such dissociation of excitons happens within tens of femtoseconds [52]. Further, in presence of the large number of carriers, once again Auger and defect-assisted Auger process can lift carriers deep into their respective bands, thus creating hot carriers [51]. It is well known that defect-assisted Auger process is expected to show a strong N_{ex} dependence [51]. The time dependence of the density of carriers in the MoS_2 following excitation by a pump pulse is given by [36, 37],

$$N(t) = \frac{N_0}{1 + tN_0\gamma'},$$
where $\gamma = \frac{\alpha\beta n_d^2}{\alpha n_d + \beta n_d}.$
(4.1)

N(t) is the remaining excited carrier density in the sample at any time t, N_0 is the

initial injected carrier density, α and β are the Auger recombination rates for the electrons and holes respectively and n_d is the defect density in the sample. This relation is shown to hold good even when the excited carrier density is more than that of the defects [36, 37]. Using the earlier reported values of α and β and assuming a defect density of 5×10^{13} cm⁻² in ML MoS₂ [118–120], we find that the defect-assisted Auger-based recombination should happen in few tens of femtoseconds time scales. Since the pulse-width of the pump is nearly 60 fs, the exciton dissociation as well as the subsequent excitation of carriers deeper into the conduction band via the Auger process should also be happening within the duration of the pump pulse. Thus, we propose that by the end of the pump pulse, the BGR, some carriers are relaxed, and some amount of hot carriers are also present in the sample. A schematic of the proposed process is shown in Fig.4.4(a).

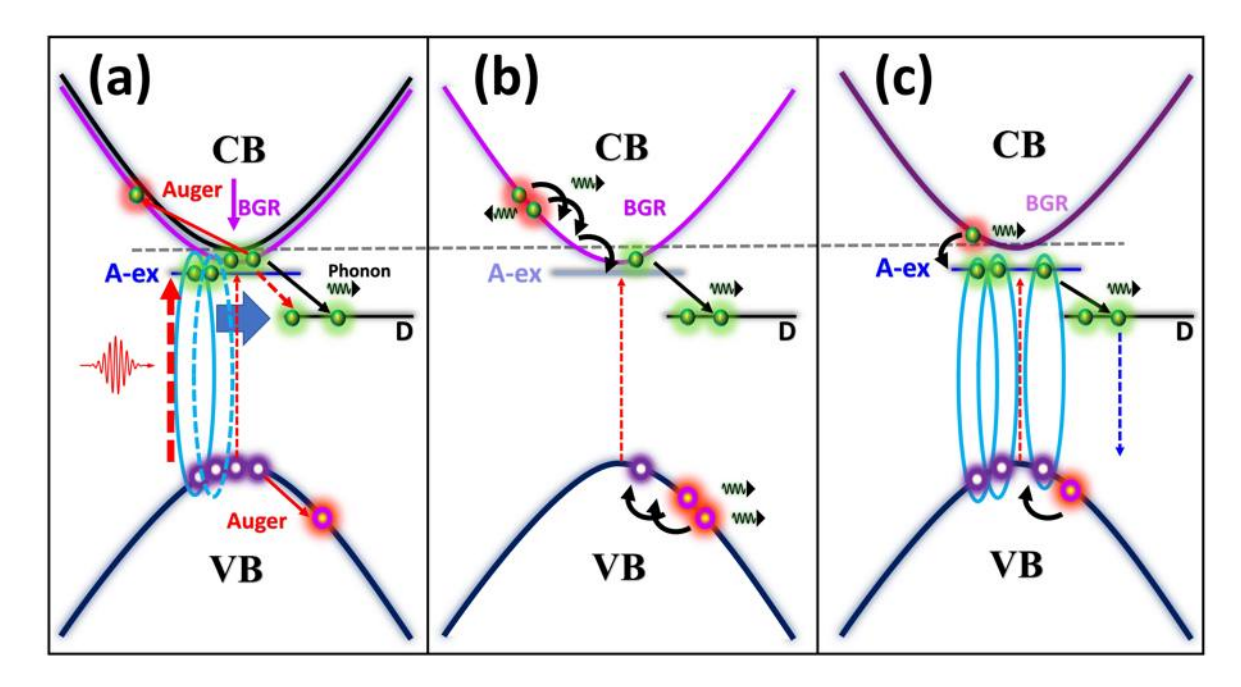


FIGURE 4.4: Schematic of the proposed processes: (a) Exciton dissociation leads to BGR and creation of hot-carrier by Auger and defect-assisted Auger scattering. (b) Cooling of hot carriers leading to formation of exciton and relaxation of carries to defect states which causes the relaxation of the measured $\Delta T/T$. (c) Filling of Aexcitonic state leading to bleaching.

Over time, the hot carriers present in the ML will relax to the edge of their respective band extrema by emission of phonons. Although such relaxation time

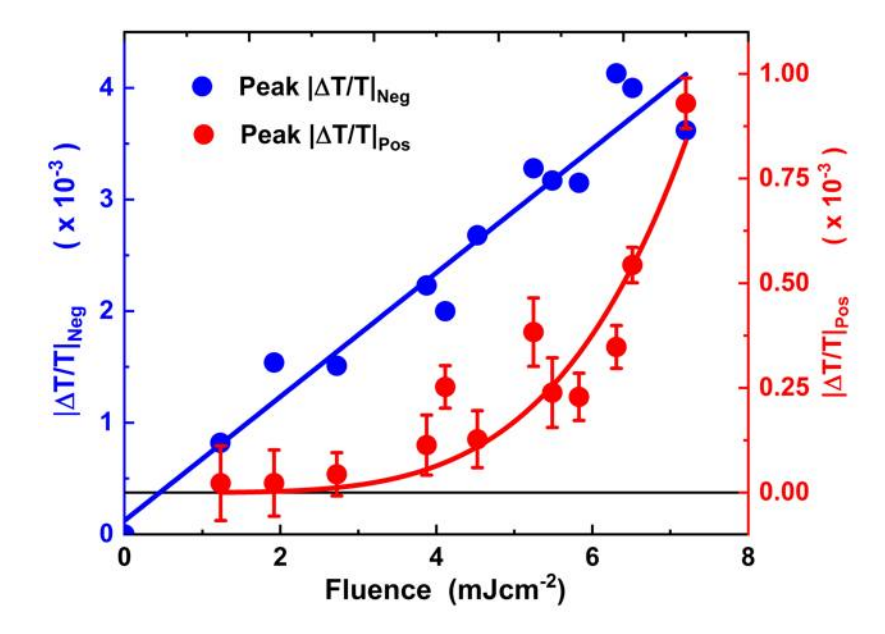


FIGURE 4.5: Fluence dependence of the magnitude of the initial negative peak (Blue dots) with best linear fit to the data represented as a blue solid line. Pump fluence dependency of the positive peak which occurs near three picoseconds delay (Red dots) with a quadratic best fit represented as a red solid line in the time dependence of $\Delta T/T$ with fluence (Fig.4.1) (see text for details).

depends on how deep the carriers are excited into their respective bands, such hotcarrier cooling time is reported to be in the order of few hundreds of femtoseconds [52]. Furthermore, the relaxation of carriers to the defect state is also expected to happen at similar time scales [27, 54]. Due to Auger scattering as well as the relaxation of carriers to the defect states, the overall N_{ex} present in the ML would eventually reduce, and hence, the probability for the formation of exciton will increase gradually. Thus, it is expected that over time, A-excitons will form leading to the bleaching of this state. Such bleaching will give a positive contribution to $\Delta T/T$ at the probe wavelength reducing the effect of BGR. Thus, as the delay between the pump and probe increases, the initial observed negative $\Delta T/T$ will start recovering over time. The relaxation time for hot carriers, formation time for exciton, and relaxation to defect states are all expected to show fluence independent relaxations similar to that observed here (Fig.4.3(b)) [36–39]. Fig.4.4(b) shows a schematic of the processes of the initial relaxation of carriers proposed above.

4.1.2 Transient Transmission of ML MoS₂ in Full-Time Scale

To investigate the carrier dynamics further, variation of the negative peak and positive peak with pump fluence is compared. As discussed before, the variation of the measured magnitude of the initial negative peak, $|\Delta T/T|_{neg}$, is linear with pump fluence. On the other hand, the pump fluence dependence of the magnitude of the later positive peak in $\Delta T/T$, $|\Delta T/T|_{pos}$, which occurs nearly at 3 ps delay, shows very different behavior. The $|\Delta T/T|_{pos}$ remains nearly negligible at lower fluences but starts to increase quite rapidly with increasing fluence. The best fit to the data with a quadratic function, given by $y=ax^2$, with a as a fitting parameter, is also shown in Fig.4.5. Clearly, $|\Delta T/T|_{pos}$ has a strong quadratic dependence on fluence. Based on these observations, we find that there are two different processes which contribute to the overall temporal variations in the observed time dependence of $\Delta T/T$. First, an instantaneous process which contributes negatively to $\Delta T/T$ and it depends linearly on the excitation density. A second delayed process also contributes positively to the $\Delta T/T$ and it depends quadratically on the excitation density.

To further understand the time dependence of $\Delta T/T$, let us look at each time scale separately, such as the relaxation of the first negative peak, the build up time of the positive peak, and the relaxation of the positive peak. For this, we fit the experimental data to an empirical function,

$$\mathcal{F} = \frac{A_0}{2} \left[1 + \mathcal{E} \left(\frac{t}{t_0} \right) \right] \exp \left(-\frac{t}{\tau_s} \right) + B_0 \left[1 - \exp \left(\frac{t - t_d}{\tau_r} \right) \right] \exp \left(-\frac{t - t_d}{\tau_L} \right), \tag{4.2}$$

where \mathcal{E} is the Gaussian error function, t_0 is related to the pulse-width of the laser. A_0 and τ_s are the amplitude and decay time of the initial negative contribution respectively. B_0 is the amplitude of the delayed (by t_d) positive peak, with a rise time of τ_r and decay time of τ_L . The above equation is derived based on the present experimental conditions and observations. The temporal shape of our laser pulse is nearly a Gaussian function. The change in the signal during pump pulse is expected

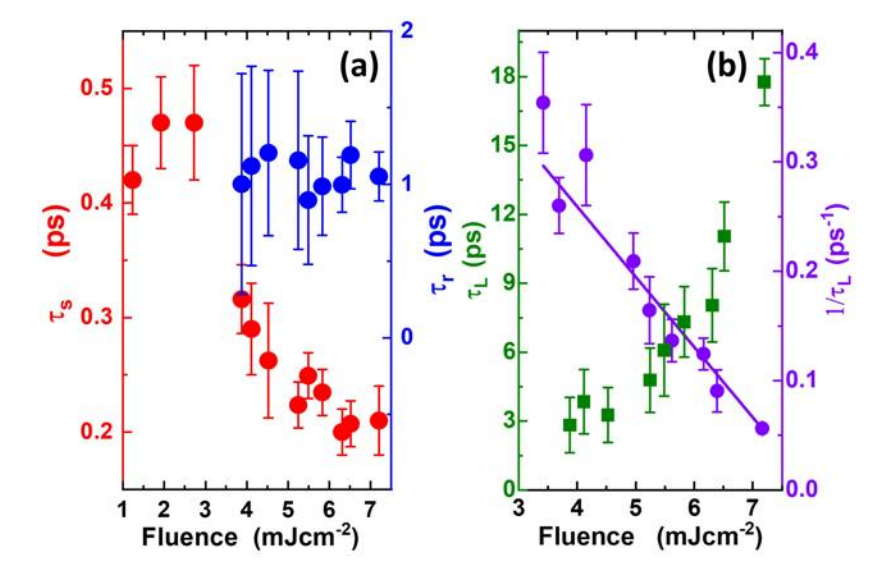


FIGURE 4.6: (a) The fluence dependence of the estimated τ_s (decay time of the initial negative signal) and τ_r (the rise time of the later positive signal). (b) The fluence dependence of the decay time of the positive amplitude, τ_L . The solid line is the linear fit to the $1/\tau_L$ data.

to depend on the number of carriers present in the excited state. This number at a given time depends on the time-integrated intensity of the pump pulse, which is an error function. At the end of the pump pulse, the signal is found to decay nearly exponentially. Based on these two observations, an error function multiplied with an exponential decay function is used to model the initial negative change in transmission. On the other hand, the form of the increase and decay of the later positive change in transmission, suggests an exponentially increasing and decaying function with different time constants for fitting the positive contribution to the $\Delta T/T$ signal. This constitutes the second part of Eq.4.2. This function \mathcal{F} , given by the Eq.4.2 was used to fit the experimental data for each fluence. The obtained best fit to the experimental data at each fluence is also shown in Fig.4.1.

Fig.4.6(a) shows the fluence dependence of the estimated τ_s . At lower fluences, the decay time of the initial negative peak, τ_s , remains nearly at 0.45 ps. As the pump fluence increases, it starts reducing quickly and eventually saturating to about 0.2 ps at higher fluences. We find that the later positive contribution is always time-shifted (t_d) by about 1.1 \pm 0.1 ps. Fig.4.6(a) also shows the fluence dependence

of the estimated rise time of the positive peak, τ_r . Further, since the positive contribution does not appear at lower fluences, τ_r could only be estimated at higher fluences. Clearly, the τ_r remains more or less constant around 1 ps. It is important to note that only with the appearance of the positive contribution to the $\Delta T/T$ at higher pump fluences, the τ_s starts reducing, indicating that they are related.

Let us first look at the origin of the fast recovery of the observed initial negative contribution, which has a response time of τ_s . At low excitation densities, it has been shown earlier that the recovery of the initial change in the optical response can be attributed to the relaxation of carriers to the defect states [27, 28, 54]. The decay time of such relaxations is reported to be in the order of 0.2 ps to 0.6 ps and is also expected to be fluence independent [27, 28, 54, 67]. In the present case, the recovery time observed at low excitation fluences, i.e., below 3 mJcm⁻², shows a nearly constant recovery time of around 0.45 ps. The density of defects in ML MoS₂ is expected to be of the order of 10^{13} cm⁻², [118–120]. As discussed earlier, at higher fluence densities, the number of carriers excited in the ML MoS₂ is expected to be larger than the number of available defect states. Thus, recovery to the defect states would not fully explain the observed recovery of optical response at higher fluences. Further, if the defect states are saturating at higher excitation densities, we should have observed an increase in the recovery time due to the non-availability of states for carriers to decay. This is the opposite of that was observed in the experiment (Fig.4.6). The presence of a large number of excited carriers can lead to Auger-based recombination either directly to the valence band recombination or through defectassisted process [37, 51]. Such Auger-based recombination can lift the carriers deep into their respective bands [51]. As the number of excited carriers reduces in the conduction band due to Auger, the effect of BGR will reduce, leading to the reduction in the observed $\Delta T/T$. It is well known that the auger process is more efficient at higher excitation densities. The reduction in the recovery time, τ_s , at higher fluences indicates that Auger-based relaxation is contributing to the reduction of signal. A schematic for explaining these processes which contribute to the initial negative contribution in $\Delta T/T$ is shown in Fig.4.7(a) and Fig.4.4(a). As mentioned earlier, in the

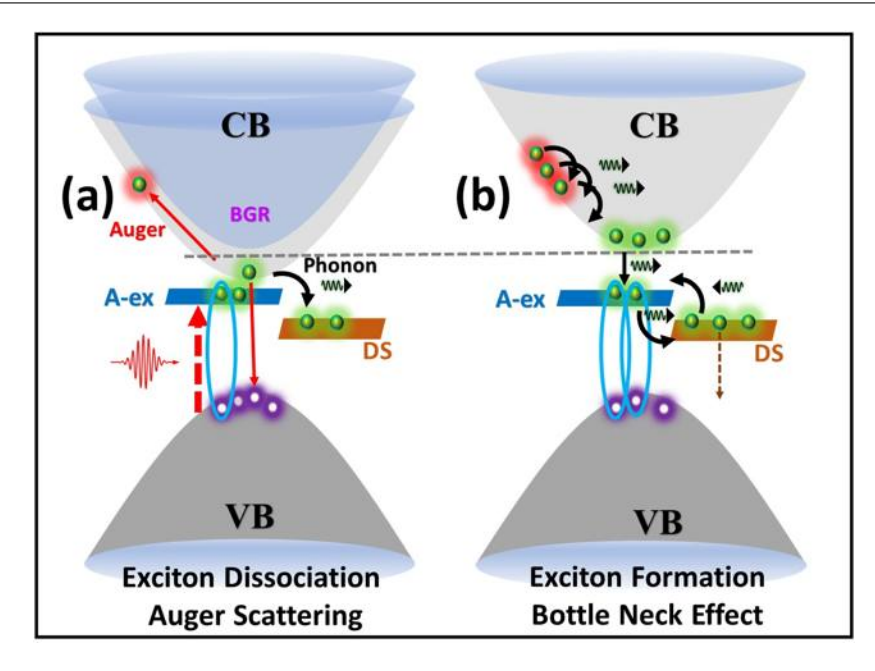


FIGURE 4.7: Schematic of the proposed processes: (a) Excitation of A-excitons (A-ex) by pump, exciton dissociation leads to BGR, and creation of hot-carrier by Auger scattering (CB-Conduction band and VB-Valance band). (b) Cooling of hot carriers leading to the formation of exciton and relaxation of carries to the defect states (DS).

range of excitation densities used in the present case, excitons are expected to dissociate within the pulse-width duration and form free-carriers [38, 39, 49]. Thus, by the end of the pulse, the abundance of carriers in the conduction band would have led to the BGR reducing the transmission at the probing photon energy.

Let us now discuss the origin of the second positive increase in transient transmission. As discussed earlier, the recovery of the initial negative peak is caused by the Auger and defect-assisted Auger processes. These processes excite carriers deep into the conduction band. As these carriers relax to the band edge, eventually excitons will start forming again due to lesser carrier density as compared to the initial excitation conditions [52]. Thus, the number of carriers relax back will directly depend on the number of carriers excited by Auger process. It has been shown earlier by various groups that the number of carriers excited by Auger depends nonlinearly on the excitation carrier density which is also proportional to the energy in the pump pulse [36, 37]. This explains why the observed peak change in the positive $|\Delta T/T|_{pos}$ increases quadratically with pump-fluence. Such formation of A-exciton would lead to bleaching of available states for absorption of the probe leading to an

increase in transmission. The band bleaching will give a positive contribution to the $\Delta T/T$ canceling the negative effect of BGR. Thus, the action of Auger should also be coupled with the bleaching of states at later time. This explains why the reduction of τ_s is associated with increase of positive $\Delta T/T$ signal (Fig.4.1 and Fig.4.6). Exciton formation time and hot-carrier relaxation time in ML MoS₂ are reported to be of the order of few hundreds of femtoseconds to about a picosecond [52]. Since the build up of carriers which corresponds to the τ_r , is happening at 1 ps time scale, we attribute this to the exciton formation time in the present case.

Defect states present in the MoS₂ provides a fast relaxation pathway for the A-excitons [31, 67]. Thus, the life time of A-excitons will depend also on the number of defect states available for them to relax. If the excitation carrier density is much lower than the defect density, then the relaxation time will remain independent of excitation fluence [36, 41]. On the other hand, if the excited carrier density is higher than this density of defect states, these states will get filled up reducing the relaxation rate of excitons [54, 67]. This bottlenecking process will lead to an increase in the life time of A-excitons. Further, if the excitation density is high enough, a large number of phonons will be emitted by the cooling of hot carriers produced by Auger [51]. These phonons will be reabsorbed by the carriers in defect states bringing them back to the A-exciton state (Fig.4.7(b)). This will lead to increase the life time of carriers in the A-exciton state which is also called as bottleneck effect [51, 67]. Similar bottlenecking process is also reported in monolayer WS₂, WSe₂, MoSe₂, MoTe₂/WTe₂ heterostructure [121–123]. The reported maximum defect state density in a CVD-grown ML MoS $_2$ is in the order of $\sim 10^{13}$ cm $^{-2}$, [119, 120]. In the present case, the excitation carrier densities used are higher than the defect state density. Therefore, defect states will eventually saturate increasing the life time of A-excitons [67]. Further, the phonon reabsorption will also contribute to the increase in the life time of carriers in A-exciton. Thus the relaxation time, τ_L will increase as the excitation fluence increases (Fig.4.6(b)). We find that $1/\tau_L$ depends linearly on the fluence which is also shown in Fig.4.6(b). Thus the scattering process involved depends directly on the number of excited carriers. A schematic of the origin of the later positive contribution to $\Delta T/T$ is shown in Fig.4.7(b). Such bottleneck effect will not occur when probed at a higher photon energies. This is due to the fact that carriers at higher energy states will eventually decay to A-exciton [54, 117].

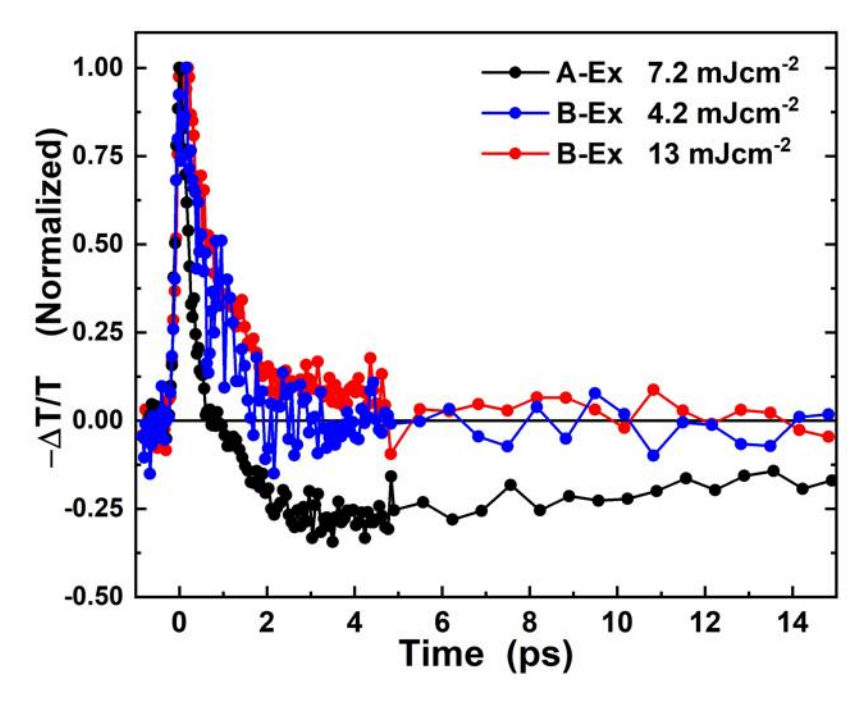


FIGURE 4.8: Degenerate transient transmission signal measured on the same ML MoS₂ flake at its A-exciton (A-Ex) and B-exciton (B-Ex) peaks. Only the measurement at A-excitonic wavelength shows bleaching effect.

A transient measurement at a different wavelength well above the A-exciton like that close to B-exciton can confirm the proposed process. Fig.4.8 shows the normalized transient transmission signal measured on the same MoS_2 flake but at B-exciton wavelength. For comparison, the transient transmission signal measured at A-exciton is also shown along with that of B-excitonic response. The measurement at B-exciton wavelength also showed a negative $\Delta T/T$ which is what expected when BGR is in action [55, 116]. Even at double the fluence than that used for A-exciton measurement, we find that the $\Delta T/T$ measured at B-exciton did not show any positive signal. This indicates that at these fluences, only BGR dominates and bleaching effect does not show up as the carriers are relaxing to the lower most exciton, the A-exciton. Thus, the measurements at B-exciton confirms our proposed model.

4.2 Summary

In this chapter, the ultrafast optical response of ML MoS $_2$ is investigated at the least studied excitation densities in the range of $\sim 0.66 \times 10^{14}$ cm $^{-2}$ to $\sim 4 \times 10^{14}$ cm $^{-2}$ using carrier dynamics measurements. We have shown that the temporal response is considerably different from that seen at lower excitation densities. We have provided a comprehensive analysis of the ultrafast optical response of ML MoS $_2$ at higher excitation densities near the A-exciton transition level. In ultrafast transient studies, it was discovered that excited carriers create an initial BGR effect, which quickly switches to bleaching. This BGR effect is caused by the generation of free carriers by exciton dissociation, which is subsequently followed by Auger and defect-assisted Auger scattering. During this transition period, the majority of the charge carriers recombine, while the remaining form excitons, allowing the formation of A-excitons. The formation of A-excitons leads to bleaching of this state. A longer relaxation process with increasing decay time suggests a bottlenecking process caused by defect state saturation and reabsorption of available phonons. These studies are crucial for the use of MoS $_2$ at high-excitation densities.

Chapter 5

Comparison of Ultrafast Carrier Dynamics near A, B, and C-excitons in Two-Dimensional MoS₂

As discussed in the chapter 1, due to quantum confinement, low dimensionality, and high Coulomb interaction, ML MoS₂ possesses three well distinguishable exciton peaks, A, B, and C, in the visible region with a high binding energy of the order 0.5 eV [20–22]. Due to these excitons, absorption of light in the visible region is up to 20% in a ML [23]. These excitons greatly influence the relaxation and scattering processes in a ML MoS₂. Hence, it is important to study the dynamics of the carriers at the individual excitonic transition energies for its future applications.

As we discussed earlier, several groups have examined the ultrafast carrier dynamics in ML MoS₂ under various excitation conditions. Exciton relaxation via defect states [27, 28], exciton-exciton annihilation [29–33], Auger recombination and defect-assisted Auger recombination [34–37], and carrier cooling by phonon emission [38–42] are all examples of relaxation and scattering mechanisms. The optical response is strongly influenced by these physical processes which in turn strongly depends on the excited carrier density. It is vital to assess the influence on various time constants of excitation densities and to understand the related physical

processes in order to gain a complete understanding of the material. In the case of MoS₂, such ultrafast carrier dynamics investigations at high excitation densities are relevant for its usability in devices that manage high carrier densities [43–46]. However, most of the studies are at A/B-exciton transition energies. Only a few studies have been carried out at the C-exciton transition energy [28, 51, 69]. Futher, all these studies are performed at low excitation densities. Hence, it is important to understand the carrier dynamics at the individual exciton peaks at similar excitation densities. Such comparative study will be helpful in the application of MoS₂ in lasers, OPAs, LED, sensors, etc. [43–46].

In this chapter, carrier dynamics at A, B, and C-excitons of the same flake were examined above Mott density by pumping and probing at the corresponding excitonic states[†]. In this work, the transient measurements are carried out at excitation densities in the range $\sim 6 \times 10^{13}$ cm⁻² to $\sim 6.7 \times 10^{14}$ cm⁻², [48, 49]. It is shown that the excited carriers behave differently at different exciton levels. Bandgap renormalization (BGR) causes an initial negative change in the transient transmission signal at A and B-exciton while only band bleaching was observed at C-exciton. In comparison to the A and B-excitonic cases, the transient signal at C-exciton was found to recover slowly. Although, the transient behavior at A-exciton is presented in detail in the earlier chapter, for comparison with other excitons, the transient response at A-exciton is discussed in brief at appropriate places.

5.1 Transient Transmission of ML MoS₂ near A, B, and C-excitons at Equal Photoexcitation Density

The absorption spectrum (Fig.2.1) of the selected ML MoS₂ flake has its excitonic peaks at photon energies 1.83 eV, 1.98 eV, and 2.86 eV corresponding to A, B, and C-excitons, respectively. The corresponding spectral widths are 0.11 eV, 0.18

[†]This work is published by the author of this thesis as "A comparative study of ultrafast carrier dynamics near A, B, and C-excitons in a monolayer MoS₂ at high excitation densities", **Durga Prasad Khatua**, Asha Singh, Sabina Gurung, Manushree Tanwar, Rajesh Kumar and J. Jayabalan, Optical Materials, 126, 112224 (2022).

eV, and 0.68 eV, respectively. Note that, the absorption coefficient at the peak of B-exciton and C-exciton is \sim 1.24 times and \sim 4.28 times when compared to that of at A-exciton, respectively. Hence, at each wavelength, the fluence was chosen such that the excitation density remains in the similar order depending on the absorption cross-section at that exciton peak.

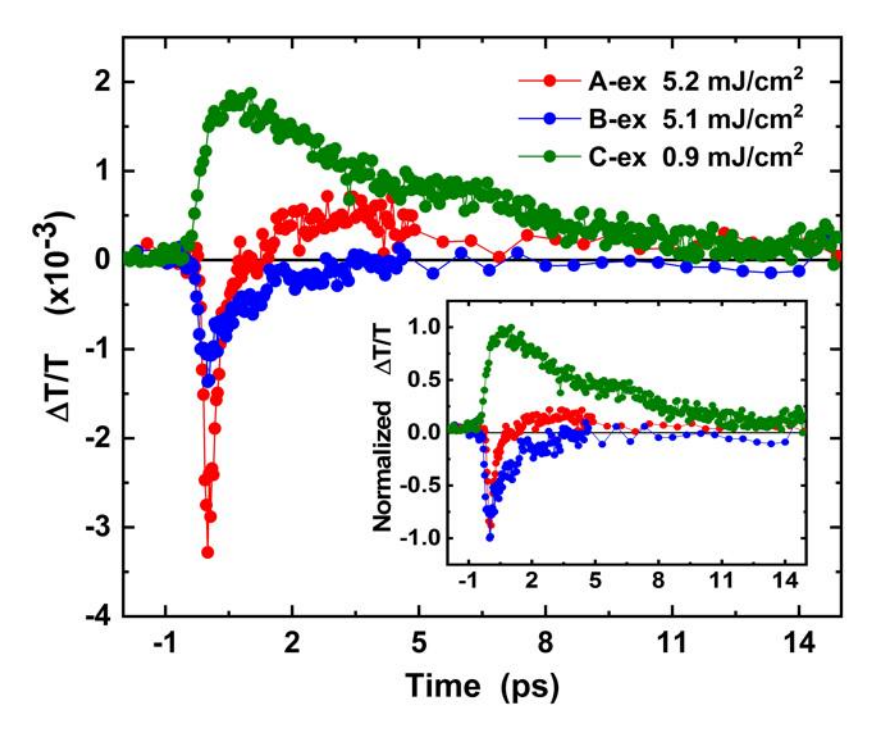


FIGURE 5.1: Transient transmission signal measured on a ML MoS_2 by exciting at 1.83 eV, 1.98 eV, and 3.09 eV which are within the peaks of (a) A-exciton, (b) B-exciton, and (c) C-exciton, respectively. Normalized signals of the same transient transmission signals are shown in the corresponding inset.

Fig.5.1 shows that the transient transmission signal measured on the ML MoS₂ by exciting and probing at three photon energies, 1.83 eV, 1.98 eV, and 3.09 eV which are within the peaks of A, B, and C-excitons, respectively. The carrier density in all the three cases is nearly the same and is $\sim 3 \times 10^{14}$ cm⁻². The measurement at 1.83 eV (A-exciton) shows that with the arrival of the pump, transmission through the sample decreases reaching an initial negative peak in $\Delta T/T$, within the pump pulse duration. With a further delay between the pump and probe pulses, the change in $\Delta T/T$ starts recovering reaching zero near about a picosecond. However, at later times $\Delta T/T$ becomes positive which eventually recovers at tens of picoseconds time scale. The measurement at the B-exciton peak shows a slightly different behavior compared to that performed at the A-exciton peak (Fig.5.1). As

in the case of A-exciton, transmission through the sample decreases with the arrival of the pump pulse which also reaches a maximum within the pump pulse duration. With increasing delay time, this peak also recovers to become zero. However, the positive $\Delta T/T$ observed in the case of A-exciton measurement is not present in the B-exciton case. Fig.5.1 also shows the transient transmission signal measured near the C-exciton case (3.09 eV). When compared to the A and B-exciton cases, the $\Delta T/T$ measured at C-exciton shows a completely different behavior. It is observed that with the arrival of the pump pulse, the transmission through the sample starts increasing ($\Delta T/T$ is positive) reaching a maximum by about \sim 500 fs. Over time, this change in transmission starts recovering eventually reaching zero at a later time. Further, the build up time, as well as the recovery time are found to be much longer when compared to that of the other two cases.

5.2 Fluence Dependent Transient Transmission

Having looked at the behavior of the $\Delta T/T$ at each excitonic state at a given excitation density, let us now look at the fluence-dependence at each of these three photon energies. Fig.5.2(a) shows the fluence-dependence at 1.83 eV photon energy which is at the peak of A-exciton. We find that the magnitude of the peak change in the $\Delta T/T$ ($|\Delta T/T|_{max}$) increases linearly with the fluence (see Table.5.1) [49]. The maximum change in the positive $\Delta T/T$ which occur nearly at 3.5 ps also increases with fluence. However, the rate of increase in the positive peak magnitude, which occurs nearly at 3.5 ps was found to vary non-linearly with the fluence. The $\Delta T/T$ normalized to the negative peak magnitude shows that the recovery time for the initial peak remains nearly the same. To estimate the decay time of the initial fast decay, we use a single exponential decay function given by,

$$F = \mathcal{Q} \exp(-t/\tau) + \mathcal{R}, \tag{5.1}$$

to fit the first 3.5 ps transient transmission data of A-exciton. Here Q is the peak amplitude, τ is the decay time and R is a constant. Table.5.1 also shows the best fit

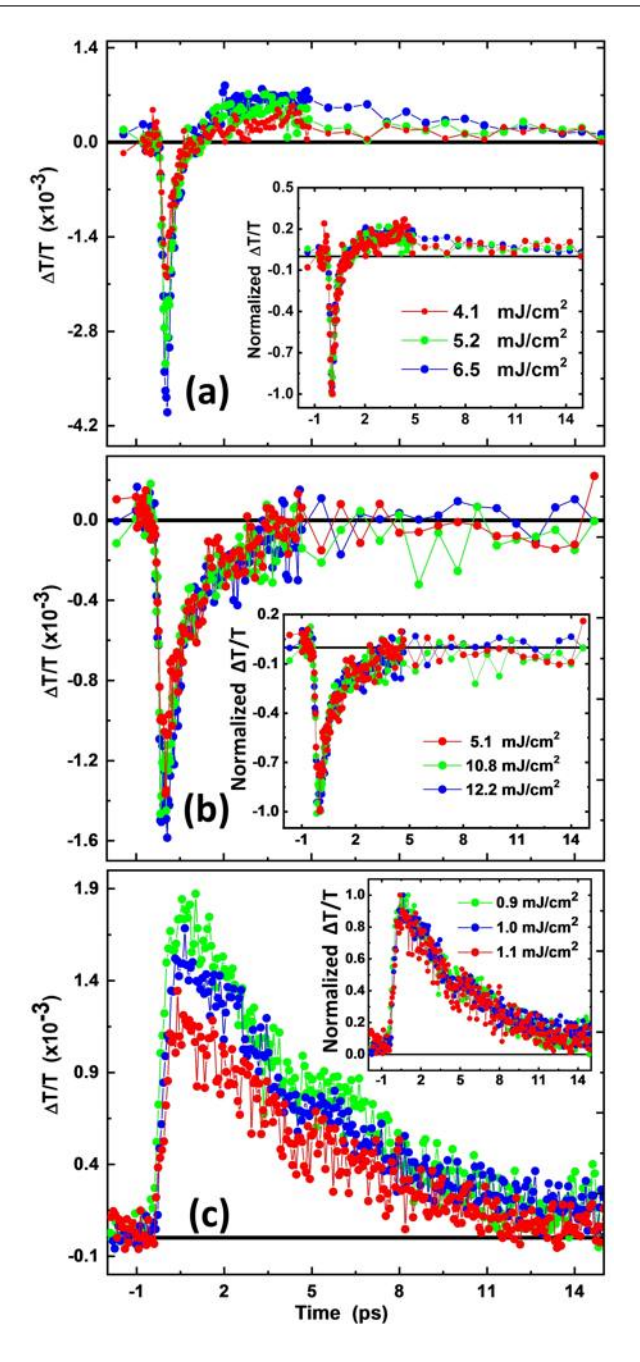


FIGURE 5.2: Pump fluence dependent transient transmission signal measured on ML MoS_2 near (a) A-exciton, (b) B-exciton, and (c) C-exciton. Normalized signals of the same transmission signals are shown in the corresponding insets. Legends show the pump fluences used for these measurements.

parameters of decay time as a function of fluence. Clearly, the decay time remains more or less the same, independent of the fluence. Fluence-dependent transient transmission measurement of the ML MoS₂ sample at B-exciton transition energy is shown in Fig.5.2(b). In B-exciton case, the peak change in the magnitude of $\Delta T/T$ also increases with the increase in fluence (Table.5.1). Further, the recovery time

Fluence (mJcm⁻²) $|\Delta T/T|_{max}$ (x10⁻³) **Excitons** $\tau \pm \Delta \tau$ (ps) 4.1 2.00 0.37 ± 0.04 A 5.2 3.28 0.36 ± 0.02 6.5 4.00 0.37 ± 0.02 5.1 1.37 1.11 ± 0.14 В 10.8 1.47 0.95 ± 0.12 12.2 1.59 0.93 ± 0.10 0.9 1.73 5.45 ± 0.25 C 5.55 ± 0.19 1.0 1.50 1.1 1.28 4.99 ± 0.20

TABLE 5.1: Pump fluence dependent $|\Delta T/T|_{max}$ and decay time of the transient measurements performed at the excitonic peaks.

of $\Delta T/T$ also remains almost constant with fluence. This can be confirmed from the normalized $\Delta T/T$ shown in the inset of Fig.5.2(b). Fig.5.2(c) shows the fluence-dependent $\Delta T/T$ measurement of ML MoS₂ near C-exciton by pumping and probing at the same photon energy, 3.09 eV. Unlike the other two cases, we find that the maximum magnitude achieved by the $\Delta T/T$ reduces with the increase in fluence in the C-exciton case. In Table.5.1, we also show the variation of $|\Delta T/T|_{max}$ as a function of fluence. The normalized transient data shows that the relaxation time period remains the same, independent of fluence, similar to that of the other two cases (Fig.5.2(c)). The function given by Eq.5.1 was also used to fit the decay part of the $\Delta T/T$ data of B and C-exciton cases. Here in both these cases, the constant \mathcal{R} is chosen to be zero. The best fit data for the τ are also given in Table.5.1.

5.3 Model and Explanation of the Processes

Let us now look at the physical processes that can explain the observed transient changes in the transmission. When illuminated by a photon having energy higher than the bandgap of MoS_2 , electrons are excited from the valance band to the conduction band. As mentioned in the introduction, several groups explored the recovery of the changes that introduce an alteration in the optical property of a ML MoS_2 at A and B-excitonic states following excitation by an ultrashort pulse [27–33, 35–42, 50–55, 63]. While carriers are excited to higher energy levels such as

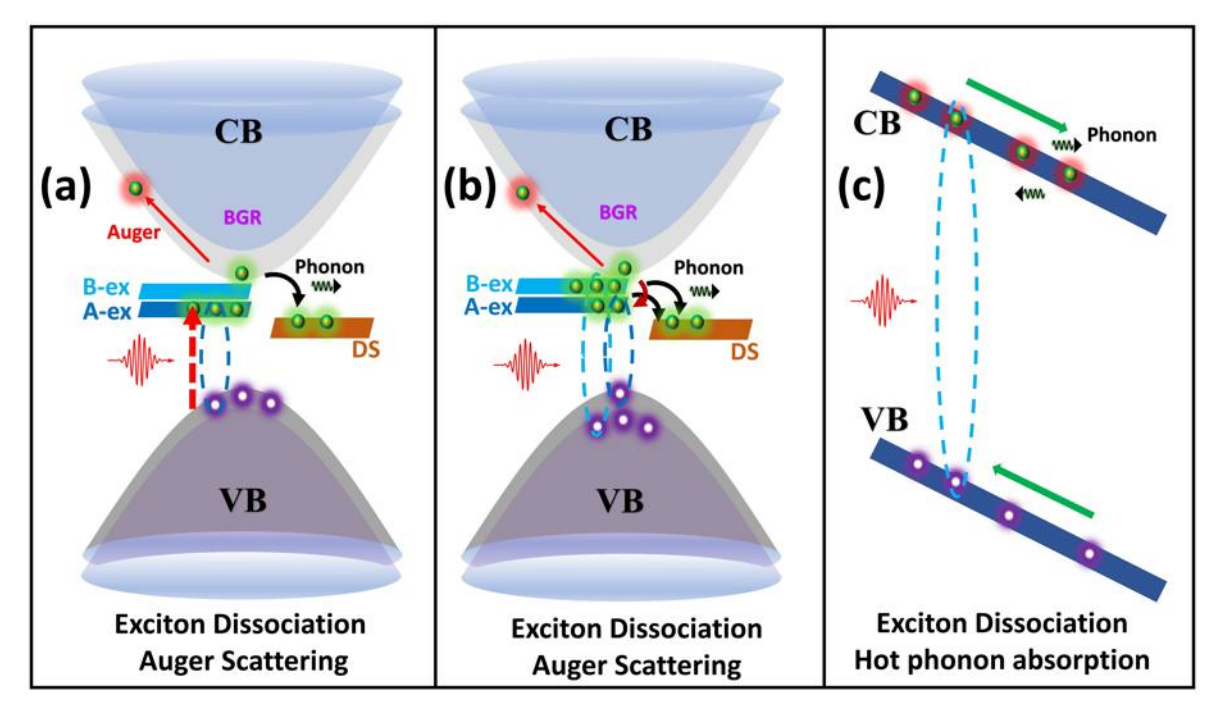


FIGURE 5.3: Schematic of the proposed processes that happen at each exciton photon energy: (*a*) Processes at A-exciton where exciton dissociation and Auger scattering dominate. (*b*) Processes at B-exciton, here also exciton dissociation and Auger scattering dominate. (*c*) Processes at C-exciton where upon excitation carriers move in the opposite direction to achieve minimum energy states. At this excitation energy level, hot phonon reabsorption dominates.

C-exciton, some processes like bottlenecking effect and Auger heating effect are also expected to play a role [40, 51]. These processes will lead to a slower carrier cooling at the C-exciton state [30, 124].

When the pump and probe photon energies are tuned to 1.83 eV, carriers are directly excited to the lowest A-exciton state. The excitation density, N_{ex} , in the present case is higher than Mott density, which is about $\sim 10^{13}$ cm⁻², [39, 49, 54]. At high excitation densities, it has been shown that the excitons can dissociate to form free carriers due to the large exciton density in the material. The generated carriers will create a BGR effect which leads to a reduction in the bandgap causing a decrease in the transmission at this probing wavelength [38, 39, 48, 49]. Further, the presence of the large number of free carriers will also create hot carriers through Auger scattering and defect-assisted Auger scattering [36, 37, 51]. As the density of carriers in the conduction band decreases as a result of Auger scattering, relaxation

to defect states, and BGR, $\Delta T/T$ recovers. At later time, the A-excitons will once again form which will eventually lead to the observed bleaching, the positive $\Delta T/T$ [48]. A schematic of the proposed processes is shown in Fig.5.3(a). When carriers are excited to the B-exciton, the situation is expected to remain nearly the same. The pump pulse would form B-excitons and due to the large density, once again carriers will dissociate leading to the BGR and the negative $\Delta T/T$ [52]. Similar to the case of A-exciton, the initial negative change in $\Delta T/T$ will eventually recover over time due to relaxations. However, the carriers would eventually relax to A-excitonic state rather than staying in the B-excitonic state. Thus, the delayed positive $\Delta T/T$ that is observed in the case of A-exciton measurement would not be observed in the present B-exciton case. Fig.5.3(b) shows the proposed processes [48].

As mentioned before, unlike the A-exciton and B-exciton where the excitons are formed by the holes in the valence bands and electrons in the conduction band, the C-exciton peak is formed in a different way. This peak is due to the transitions between valance band and conduction band in between the Γ and K points at the band nesting region [30, 31]. In this region, conduction band is parallel to that of valence band with a finite slope [30, 31]. Hence, after photo-excitation, both electrons and holes move in opposite directions in the momentum space to achieve a minimum energy state by moving towards the nearest valleys in the conduction and valance bands [30, 31]. Besides this, C-exciton has a higher photon energy when compared to that of A and B-excitons. In this experiment, the excited carrier density is higher than the Mott density. Due to the high availability of vacancy energy states and all the discussed reasons, electrons and holes will form excitons and hence, band bleaching will take place. However, with increasing carrier density, BGR effect will strengthen. Therefore, there will be a competition between the band bleaching and the BGR effect which will eventually lead to decrease in the peak height of the transient transmission signal. At this excitation energy and density, kinetic energy of the carriers is high and hence, relaxation and thermalization of the carriers will happen through the interaction of the carriers with lattice via releasing a large number of hot phonons (Fig.5.3(c)). This non-thermal and high energetic phonons will be reabsorbed by the carriers creating a bottlenecking effect which prolongs the carrier relaxation time [30, 51].

5.4 Summary

Studies on TMDC materials at various excitonic states is crucial due to the increase in its demand in optoelectronic applications. In this chapter, with the transient transmission measurements tuned to each of the three primary absorption peaks in the visible regime, we have shown that the ultrafast carrier dynamics in ML MoS₂ at higher carrier density is completely different from the carrier dynamics studied at lower excitation density. At A and B-exciton states, an initial BGR effect is observed due to the exciton dissociation. At A-exciton level, a change of sign in the transient signal is observed due to band bleaching but, not seen at the B-exciton level even if at higher pump fluence. Ultrafast carrier dynamics at the C-exciton state is completely different from A and B-exciton case where only band bleaching is observed. The rising and relaxation times of the signal at the C-exciton level are also found to be much slower than the other excitons.

Chapter 6

Comparison of Carrier Dynamics in Monolayer and Bulk MoS₂

The usage of bulk and ML MoS₂ in optoelectronics and sensor devices requires a detailed study of the basic of carrier behaviors in the materials. Measurement of carrier relaxation dynamics will give an insight into the transient optical and electronic properties of these samples. As discussed in Chapter 1, MoS₂ has an indirect bandgap in bulk form whereas it is a direct bandgap material in ML form [3, 4]. However, the spin and valley properties of the MoS₂ remain the same in its ML and bulk form specifically at the *K* point of the Brillouin zone [3, 4, 52]. Along with this, the direct bandgap nature at the *K* point is not much affected in bulk and ML case [3, 4, 52]. Different groups have studied the carrier dynamics in bulk and ML MoS₂ sample earlier to understand the carrier behavior in the materials with different excitation and probing conditions [27–42, 50–55]. Nearly all these studies are carried out at low excitation density conditions, which show that the optical and relaxation times are very different in bulk when compared to that of ML.

In this chapter[†], we present the results of the carrier dynamics studied in a ML and a bulk MoS_2 flake in a pump fluence range from 1.2 mJcm⁻² to 7.5 mJcm⁻²

[†]This work is under preparation by the author of this thesis as "Pump fluence dependent carrier dynamics at the A-exciton of MoS₂: Monolayer Vs Bulk", **Durga Prasad Khatua**, Asha Singh, Sabina Gurung, and J. Jayabalan.

by exciting and probing the carriers at A-exciton. AFM measurements were carried out to estimate the number of layers in the selected bulk MoS₂ flake and was identified to contain approximately 11 layers (Fig.2.8). We show that both in ML and bulk cases, a BGR occurs due to exciton dissociation. The initial relaxation time of the transient signal decreases both in bulk and monolayer case with increasing pump fluence. The decrease in relaxation time in the ML is due to the Auger and defect-assisted Auger processes while in the bulk, intervalley scattering also plays an important role along with the Auger and defect-assisted Auger processes. Intervalley scattering will not a play an important role in ML MoS₂ as this process is weaker when carriers are excited to the lowest transition energy level (A-exciton). Furthermore, the peak height of the transient signal gets saturated in bulk at higher pump fluences where it remains linear in ML MoS₂. These studies will be helpful for the application of MoS₂ in various optoelectronic device applications [43–46].

6.1 Transient Measurements near A-exciton

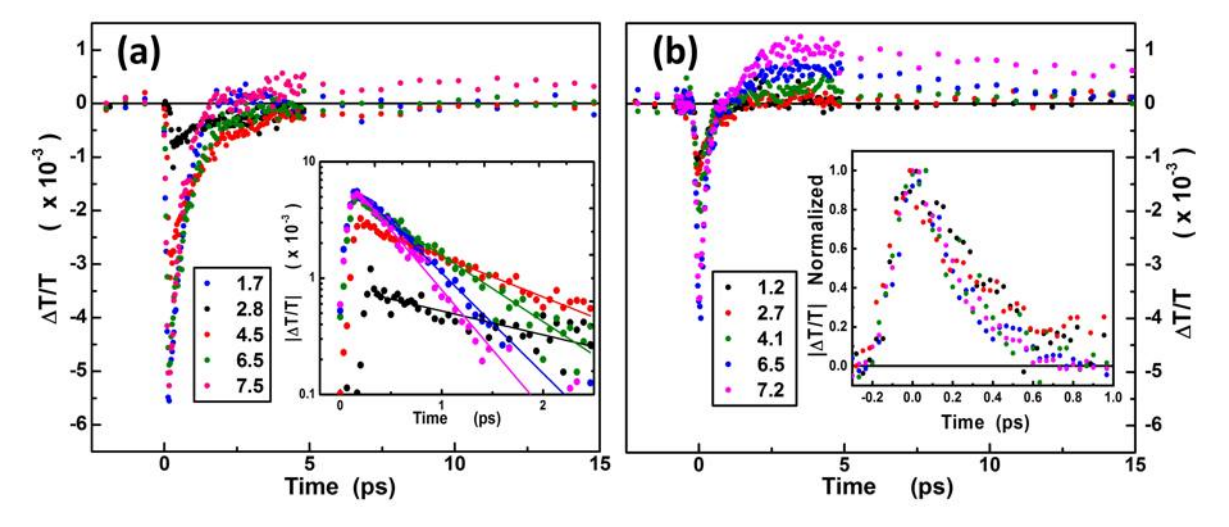


FIGURE 6.1: Pump fluence dependent transient transmission signal recorded by pumping and probing at 672 nm pulsed laser: (a) Bulk MoS₂ flake. In the inset, the $|\Delta T/T|$ is shown in a short time scale with y-axis in natural log scale. (b) ML MoS₂ flake. Inset shows the normalized $|\Delta T/T|$ in short time scale. In both these cases, the legend shows the pump fluence which is in mJcm⁻².

The transient measurements on the bulk were also carried out in the degenerate pump-probe setup which uses the Oscillator-Amplifier-OPA femtosecond laser

system operating at 1 kHz repetition rate. The 672 nm laser beam (A-exciton resonance energy) was selected at the OPA output for these measurements. The microscopic arrangement was used to view the bulk flake and overlap the pump and probe beams on it. Both these pump and probe beams are focused on the samples by using two parabolic mirrors such that the pump pulse fully illuminate the bulk flake while the probe beam is well within it (Fig.3.13). The pulse-width of the pump and probe beams are ~ 60 fs. The detection scheme that was developed for low-repetition rate laser is used to record the transient signals of the flakes [47, 49].

Pump fluence dependent transient transmission signal $(\Delta T/T)$ of the bulk MoS₂ flake is shown in Fig.6.1(a). The transient signal of the sample reduces at the arrival of the pump pulse and attains a negative peak nearly by the end of the pump pulse. This change in the transmission then starts recovering as the delay between the pump and probe beam increases and returns to its original unperturbed transmission value by about 5 ps. As the pump fluence increases, the magnitude of the peak change in the transmission also increases. At higher fluence, the recovery of transmission was found to be faster than that at lower pump fluences. Further, when pump fluence is $< 6.5 \text{ mJcm}^{-2}$, the transient signal recovers completely to zero level by about 5 ps. However, as the fluence is increased beyond 6.5 mJcm^{-2} , $\Delta T/T$ was found to change its sign from negative to positive after about 4 ps. With further delay between the pump and probe pulse, this positive change in transient transmission also reduces back to zero in tens of picoseconds time scales. In the inset of Fig.6.1(a), we show the same transient signal of the bulk MoS₂ flake in the first few picoseconds time scale, while Y-axis is in log scale. The solid lines in the plot are the best linear fit to the data in the 0.3 ps to 2.5 ps range.

In Fig.6.1(b), the transient transmission signal of a ML MoS₂ recorded at the A-exciton state is shown for the same pump fluence range as that of the bulk. As in the bulk case, $\Delta T/T$ signal of the ML MoS₂ starts decreasing with the arrival of the pump pulse showing a negative peak within the laser pulse-width. This peak starts recovering with increasing time. As the fluence increases, the negative peak height of the $\Delta T/T$ also increases. Up to pump fluence, < 4.1 mJcm⁻², the transient signal recovers completely within the first 2 ps (much faster than that of the corresponding

bulk case). However, at higher pump fluences, $\Delta T/T$ changes sign from negative to positive. This positive signal builds up slowly and attains a peak by about 3 ps which is also shorter when compared to that of the bulk case. In the inset of Fig.6.1(b), modulus of the same $\Delta T/T$ signal of ML MoS₂ is shown in short time scale with normalization. From this plot, it can be seen that the relaxation time of the initial negative transient signal decreases at higher pump fluences. Further, it should be noted that in case of the bulk MoS₂, the later positive change in $\Delta T/T$ appears at higher pump fluences when compared to that of the ML MoS₂.

6.2 Fluence Dependence of Peak $\Delta T/T$ and Time Constants

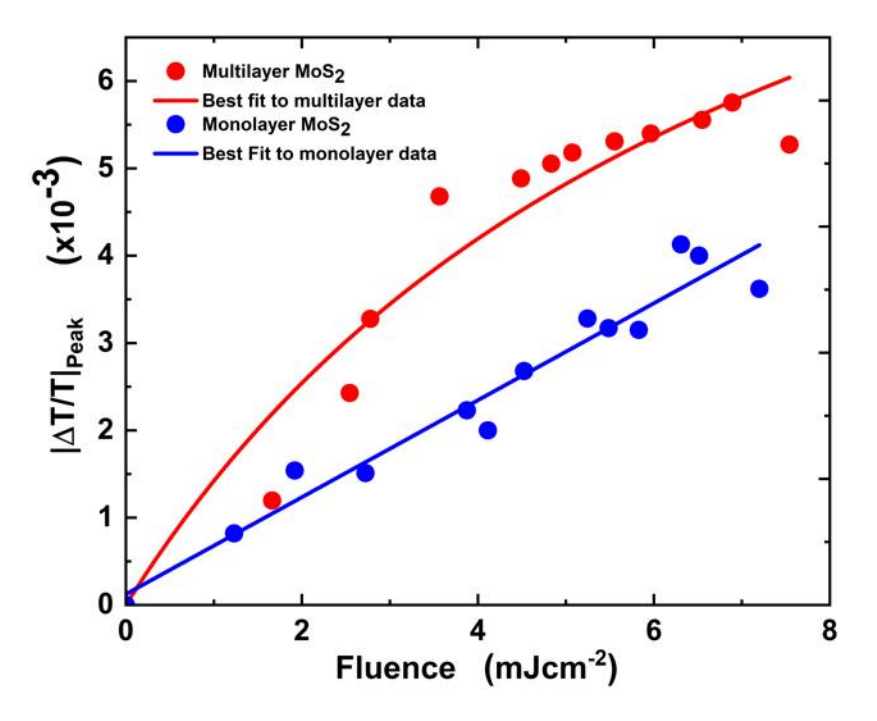


FIGURE 6.2: Pump fluence dependent variation of magnitude of the initial negative peak of $\Delta T/T$ of bulk MoS₂ (red dots) and ML MoS₂ (blue dots). The solid red line is the best fit to the $|\Delta T/T|_{Peak}$ of bulk MoS₂ with Eq.6.1 and the solid blue line is the linear fit to the $|\Delta T/T|_{Peak}$ of ML MoS₂.

Fig.6.2 shows the variation of the magnitude of the initial negative peak height of $\Delta T/T$ ($|\Delta T/T|_{Peak}$) with pump fluence for the bulk MoS₂ (red dots) and

ML MoS₂ (blue dots). In case of bulk MoS₂, initially, the peak height increases rapidly with pump fluence up to 4 mJcm⁻². As pump fluence increases beyond 4 mJcm⁻², the transient signal starts showing saturation. Whereas, variation of the initial peak height of $\Delta T/T$ in ML MoS₂ with pump fluence is different from the bulk and it does not show any saturation in the range of pump fluence used in the measurement. As discussed in the earlier chapters, the peak change in $\Delta T/T$ in the case of ML MoS₂ increases linearly with pump fluence. The solid lines represent the linear fit to the $|\Delta T/T|_{Peak}$ data of ML MoS₂. In bulk case, the data is fitted with a saturation function,

$$y = \frac{\mathcal{M}x}{\mathcal{N}x + \mathcal{O}'},\tag{6.1}$$

where y is the peak of the transient signal, x is the pump fluence, and \mathcal{M} , \mathcal{N} , and \mathcal{O} are constants.

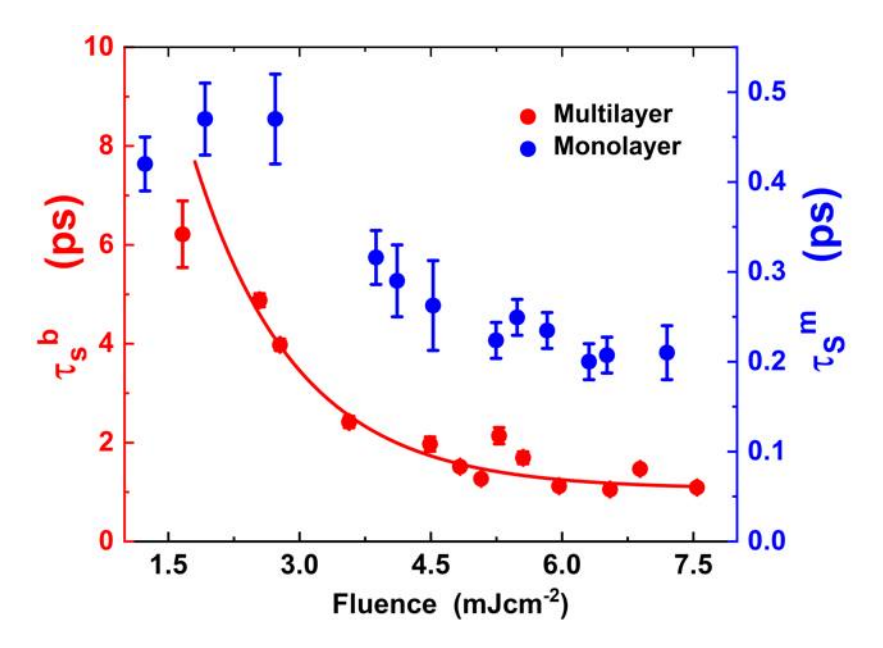


FIGURE 6.3: Pump fluence dependent initial relaxation time of the bulk (red dots) and ML MoS₂ (blue dots) flakes.

In Fig.6.3, pump fluence dependent relaxation time of the initial negative peak of the transient transmission signal of bulk MoS₂ (red dots) is shown. These relaxation times of the initial peak is extracted by fitting the transient data in the

range of 0.3 ps to 2.5 ps after converting to logarithm scale with the equation,

$$\ln\left(\Delta T/T\right) = -t/\tau_s^b + const.,\tag{6.2}$$

which is equivalent to a straight line equation,

$$y = ax + c$$
.

Here, τ_s^b is the decay time period of the initial negative peak and slope $a = -1/\tau_s^b$. This τ_s^b decreases rapidly with increase in pump fluence as shown in inset of Fig.6.1(a). These data points are fitted with an exponential function $\tau_s^b = exp(-kf)$, where, k is a constant and f is the pump fluence which is shown as a solid red line.

To further understand the time dependence of $\Delta T/T$ in ML MoS₂, we fit the experimental data to an empirical function,

$$\mathcal{F} = A_0 \left[1 + \mathcal{E} \left(\frac{t}{t_0} \right) \right] \exp \left(-\frac{t}{\tau_s^m} \right).$$
 (6.3)

For comparison of the initial relaxation time of ML MoS₂ with that of bulk MoS₂, the fast relaxation time, τ_s^m , is also plotted (blue dots) along the fast relaxation time of the bulk MoS₂, τ_s^b , which is shown in Fig.6.3. This shows that initially at lower pump fluences up to 2.7 mJcm⁻², the initial relaxation time remains almost constant at 0.4 ps. As the pump fluence increases beyond 2.7 mJcm⁻², the relaxation time decreases rapidly showing the same trend as that of bulk MoS₂ flake.

6.3 Model and Explanation of the Processes

The band structure of a bulk MoS_2 sample is very different form that of a ML MoS_2 (please see Fig.6.4 for a schematic of the band structure). The bandgap of a ML is 1.83 eV and happens to be at the K valley [3, 4]. If there are two layers of MoS_2 , the conduction band in between Γ and K valley (Q point) starts reducing, reaching an energy value which is lower than that of at K point [3]. Such lowering of energy

makes the two-layer MoS_2 itself an indirect bandgap material. The photoluminescence efficiency of double-layer MoS_2 thus gets reduced by about a factor of ~ 40 when compared to that of a ML MoS_2 [3]. With increasing layer number, the conduction band energy in between Γ and K point reduces even more [3, 37, 125]. After 5 to 6 layers, the changes in bandgap stabilizes resulting in a band structure which is independent of the number of layers. Thus a flake having more than 6 layers can be called a bulk [3, 37]. The flake used in the recent study has about 11 layers. Hence, it is an indirect gap bulk semiconductor flake. It has been shown earlier that in bulk MoS_2 , excitonic resonance energy remains nearly the same at the K point as that of ML MoS_2 which is 1.83 eV [3, 52]. Further, in case of a bulk sample, the binding energy of A-exciton is around ~ 45 meV making exciton dissociation in bulk a lot easier when compared to a ML MoS_2 flake [52, 126].

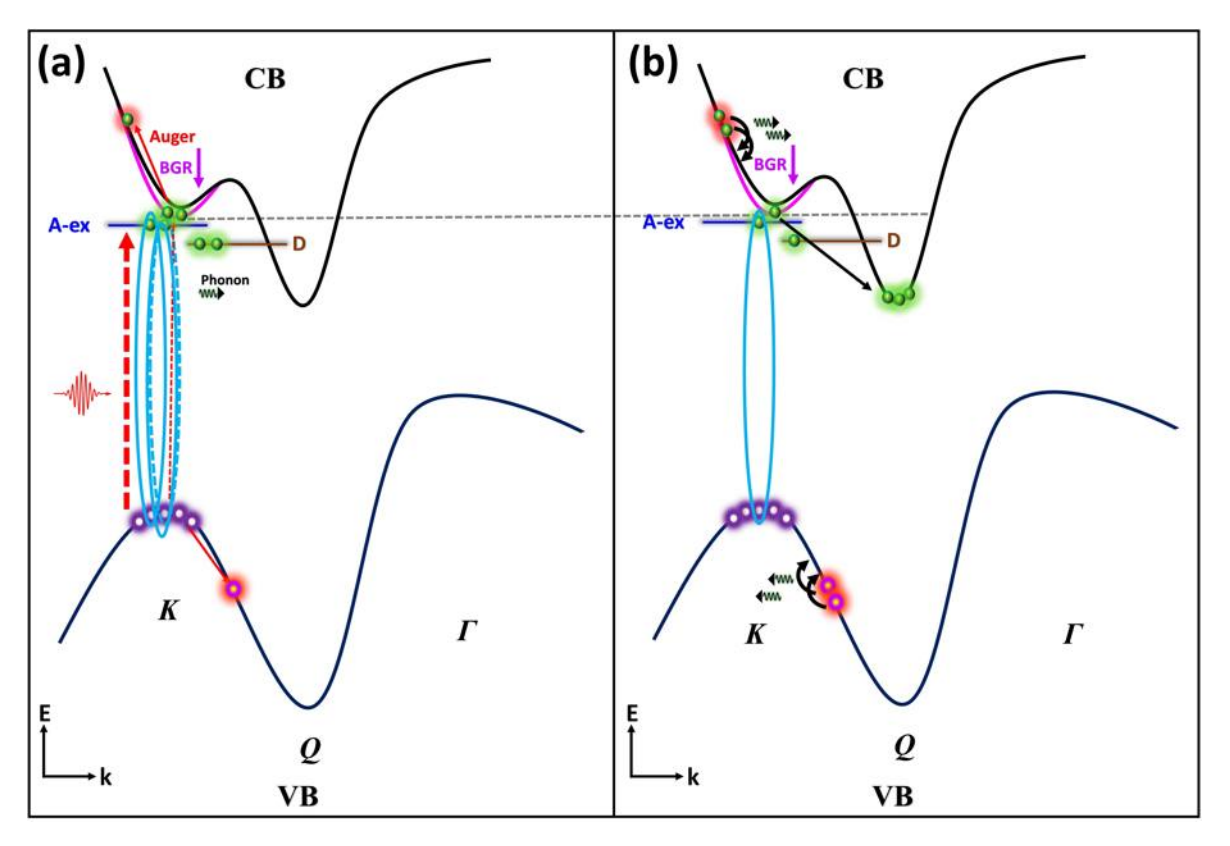


FIGURE 6.4: Schematic of the proposed processes that follow after excitation of carriers at A-exciton transition energy in bulk MoS₂: (*a*) exciton dissociation, Auger processes, (*b*) hot-carrier cooling, intervalley scattering.

Now let us look at the physical processes that drive the transient changes in

optical response of the ML and bulk flakes after excitation by a short-pulse. Different groups have earlier studied carrier dynamics in bulk and ML MoS₂ flakes at the Aexciton transition energy and reported various physical phenomena that dominate for few hundreds of picoseconds after an ultrafast pulse excitation [27–42, 51–54]. The ultrafast optical response of the bulk and ML MoS₂ flakes are also expected to be different from each other due to the difference in the physical processes that are observed. The observed physical phenomena are highly dependent on the excitation photon energy, probing photon energy as well as the type of samples, excitation density, and delay time. Various processes like exciton formation [40-42], exciton dissociation [38, 39, 48, 49], exciton-exciton annihilation [29–33], carrier-capture to defect and trap states [27, 28, 54], Auger and defect-assisted Auger scattering [34– 37], hot-phonon reabsorption [51, 67], and intervalley scattering [127, 128] are likely to happen in both bulk and ML MoS₂ flakes. These processes will lead to band bleaching [116], BGR [67, 69], exciton peak shift and broadening [30, 51, 117], etc. Due to these changes, the optical properties of the material will change which will lead to a change in the transmission of the probe beam.

In the present study, carriers are excited directly at the A-exciton transition energy. Thus in both the cases, the carriers will be excited at the K point. However, the absorption coefficient of a ML MoS₂ is higher than that of bulk MoS₂ by 40%, [129]. Hence, the excited number density will be different in ML sample than that of bulk MoS₂ by about 40%. Thus, it is expected that the excited carrier density in the ML is much higher than that of the bulk. Due to higher excited carrier density, the ML is expected to show a higher $\Delta T/T$. This is opposite to that observed in the experiment. Since the binding energy of excitons in case of bulk is much lower than that of ML, it is expected that exciton dissociation can occur at a much higher rate in bulk when compared to that of ML [38, 39, 52]. Such exciton dissociation will create more free carriers in bulk flake when compared to that of a ML. Thus, a larger BGR is expected in case of bulk when compared to that of ML MoS₂ flake for the same excitation density. The observed higher $|\Delta T/T|_{Peak}$, when compared to that of ML, as shown in Fig.6.2 could be attributed to such difference in the dissociation ability of excitons. Similar to the case of ML, over time the free carriers in

bulk are expected to decay to defect states and also form hot carriers via Auger and defect-assisted Auger processes [27, 28, 37, 54]. However, in addition to that, a large number of electrons are expected to decay to Q valley leaving holes at K valley in tens of femtoseconds time scale [127]. The life time of electrons transported to Q valley is expected to be the order of several picoseconds [127, 128]. Thus, even though there are relaxations to defect states, a large amount of carriers will get retained in the conduction band as free carriers in the case of bulk when compared to that of ML. Further, since carriers are also now at different valleys, the Auger and defectassisted Auger processes are also expected to be much less efficient. In addition, in bulk MoS₂ due to its higher thickness compared to ML, screening of the dielectric is stronger and quantum confinement becomes weaker. This leads to decrease in the strength of Coulomb interaction which in turn leads to weaker Auger scattering process [70, 130]. Hence, the recovery of the transient change in the transmission is expected to be much longer in bulk when compared to that of ML. This explains why the recovery in bulk takes much longer time as observed in the experiment (Fig.6.3). For example, at 2.5 mJcm⁻², the decay time of bulk is ~ 4.8 ps while in the case of ML, it is 0.4 ps. Similarly, at about 7 mJcm⁻² pump fluence, decay time of bulk is about 1 ps while for the case of ML, it is 0.2 ps. Further, intervalley scattering and relaxation of carriers from there would reduce the possibility of formation of Aexcitons. This is the reason why the bleaching of $\Delta T/T$ in bulk MoS₂ case is much weaker and observed only at much larger excitation fluence.

6.4 Summary

The bulk MoS_2 is an indirect bandgap in nature while ML is a direct bandgap material, still both show the same exciton energy and similar spin and valley propertied at the K point of the Brillouin zone. In this chapter, we showed that although, ultrafast response are similar in case of bulk and ML MoS_2 , the magnitude of the observed changes in the optical response, as well as the relaxation times, are found to be very different from each other. These studies were carried out in the pump fluence range 1.2 mJcm⁻² to 7.5 mJcm⁻² which corresponds to the photoexcitation

density $\sim 6.6 \times 10^{13} \ {\rm cm^{-2}}$ to $\sim 4.1 \times 10^{14} \ {\rm cm^{-2}}$ range. In spite of the fact that the bulk has a lower excitation density as compared to ML, it still showed a higher change in $|\Delta T/T|_{Peak}$ when compared to that of ML MoS₂ since the dissociation of excitons is much easier in bulk due to the lower exciton binding energy. Both bulk and ML show Auger and defect-assisted Auger recombination and a positive change in $\Delta T/T$ at later times, the bulk shows a much longer recovery time and a very low positive change. Both of these changes are attributed to the carriers scattered to other valleys in the conduction band which increases the carrier lifetime by reducing exciton formation and reducing the Auger scattering process.

Chapter 7

Conclusions and Future Scope

Monolayer and bulk MoS₂ are very interesting materials for their applications in valleytronics, spintronics, 2D-electronics, optoelectronics, memory devices, and in bio-detection. Due to the two-dimensional nature and quantum confinement, the exciton binding energy in ML MoS₂ is large which leads to strong light-matter interaction at those excitonic wavelengths. Thus, it is important to study carrier dynamics at the excitonic states in ML and bulk MoS₂ to understand the behavior of carriers at different excitation conditions. This thesis provides a detailed measurement and analysis of carrier dynamics in ML MoS₂ sample at excitation energy of A, B, and C-excitons when excited above Mott density. The dynamics in a ML is also compared with the bulk MoS₂ at excitation density well above Mott density. The ultrafast optical response of 2D MoS₂ is specifically investigated at its least studied excitation densities in the range of 1.2 mJcm⁻² to 12.2 mJcm⁻² using transient transmission measurements which transferred to excited carrier density in the range \sim $6.6 \times 10^{13} \ cm^{-2}$ to $\sim 6.7 \times 10^{14} \ cm^{-2}$ which is well above Mott density of a ML MoS₂. These studies will be helpful in application of MoS₂ in various optoelectronic devices that handles high excitation densities.

In this thesis, all carrier dynamics measurements were performed using a 35 fs Oscillator-Amplifier-OPA system operating at 1 kHz and centered at 800 nm. The standard detection schemes that are typically used in high rep-rate lasers (80 MHz) are expected to give a low signal-to-noise ratio. Hence a high-sensitive detection

scheme is developed using a boxcar and a lock-in amplifier which demonstrated to show a better signal-to-noise ratio. A theoretical model has been developed for explaining the experimental observations. Furthermore, a chopper frequencydependent measurement shows that 333 Hz is best suited for the carrier dynamics measurements while using a 1 kHz rep-rate laser. For performing transient measurements on a single flake, a pump-probe setup is developed such that the probe beam size at the sample is much smaller than the size of a single flake as well as the pump beam for homogeneous probing. The detection scheme developed for the low-repetition rate laser and pump-probe setup are then used to study the transient properties of the 2D MoS₂. Furthermore, to perform the carrier dynamics measurements on a selected ML MoS₂ flake, it is necessary to view and identify the flakes before the measurements. For this purpose, a microscope was developed using a 50X objective, a CCD camera, and a white light source in the pump-probe setup. Using this microscope, the absorption spectrum of the selected ML MoS₂ flake was also measured and compared with the averaged absorption spectrum which showed that mostly MoS₂ flakes on the sapphire substrate understudy are monolayer flakes.

Before performing the transient measurements, the thickness of the selected MoS_2 flake was measured using AFM topography image and is found to be ~ 0.8 nm showing that it is a monolayer. This is also confirmed by Raman scattering measurements. The thickness of the selected multilayer MoS_2 flake is measured to be ~ 8.9 nm indicating that there are approximately 11 layers in the sample. From the damaged threshold measurements, it is found that the ML MoS_2 flake is stable up to a fluence of 50 mJcm $^{-2}$.

In this work, all these measurements were performed at excitation densities above the Mott density of the ML MoS₂, where carrier dynamics is not well understood as this is very important for its applicability in devices that handles higher carrier density. Among the three excitonic states, being the lower most energy level, the A-exciton is known to show the strongest photoluminescence. Hence, it has been studied rigorously to understand the carrier dynamics at this resonance energy for its application in future devices. It has been shown that at A-exciton, carrier dynamics of the ML MoS₂ show an initial bandgap renormalization. This is due to the

lowering of the bandgap energy when excitons are dissociated to form free carriers. During this process, direct recombination, trapping, and defect-assisted Auger are also observed. Due to defect-assisted Auger, some carriers are also excited to higher energy states. Eventually, these hot carriers relax to the band edge to form excitons at later pump-probe delay, leading to band bleaching. At this point, the relaxation time of the carriers increases with the pump fluence due to the hot-phonon reabsorption creating a bottlenecking effect.

The carrier dynamics at B-exciton shows that an initial bandgap renormalization occurs similar to that of A-exciton which is due to the exciton dissociation. However, the later band bleaching that is observed at A-exciton does not appear in the case of B-exciton. This is due to the fact that at these transient temperatures, carriers do not live longer in the B-excitonic state and they relax to lower energy levels i.e., the A-excitonic state. Carrier dynamics measurements at C-exciton show a completely different behavior when compared to that of A and B-excitons. In this case, an initial band bleaching appears which is due to the fact that the valance and conduction bands are parallel to each other and the density of states is higher at this transition energy. Besides this, carrier dynamics measurements at C-exciton shows a prolonged relaxation time when compared to that of A and B-exciton case due to the bottlenecking effect. Furthermore, the peak height of the transient signal at C-exciton decreases with pump fluence whereas it increases at A and B-exciton cases. This is explained by the fact that with increasing pump fluence, there is a competition between band bleaching and bandgap renormalization effects.

The carrier dynamics of the ML and bulk MoS₂ sample are also measured at A-exciton transition energy and compared at the excitation densities above the Mott density. It has been shown that as in the case of ML, carrier dynamics in the bulk MoS₂ also shows an initial bandgap renormalization. The peak height of the bulk sample saturates at higher fluences while it remains linear in the case of ML MoS₂. It has also been observed that the initial relaxation time of the transient signal in ML MoS₂ and bulk MoS₂ flakes decreases sharply with increase in pump fluence. However, the relaxation time of the transient signal in bulk is slower as compared to that of a ML flake at the same pump fluence. The main difference in their behavior

could be attributed to the fact that the bulk MoS_2 is an indirect bandgap material whereas ML MoS_2 has a direct bandgap. Further, intervalley scattering is expected to play a dominant role in the case of bulk when compared to that of ML.

To conclude, this thesis provides a detailed understanding of transient optical properties of 2D MoS₂ at carrier densities well above Mott density at the three excitonic resonance energies for its use in optoelectronic devices that work at higher carrier densities. Although A, B, and C excitons were well investigated using probe-wavelength-dependent pump-probe spectroscopy, a full broadband probing would shine more light into the carrier dynamics process. Along with this, a transient signal detection scheme which can provide a high signal-to-noise ratio while working with a low-repetition rate laser system is also reported. All these results obtained through carrier dynamics measurements in ML and bulk MoS₂ samples will be useful for the future use of these samples in OPAs, lasers, LEDs, sensors, and detectors.

Appendix A

Calculation of Carrier Density Generated in the Sample

Consider a laser with repetition rate *R*. Let the average power of the laser beam at the sample place to be *P*, then the energy of a single pulse is,

$$E = P/R. (A.1)$$

For a Gaussian spatial profile beam, fluence of the beam at the sample place is,

$$\mathcal{F} = \frac{4E\ln(2)}{\pi r_{FWHM}^2},\tag{A.2}$$

where r_{FWHM} is the full width at half maximum of the pump beam. Let the transmittance and reflectance of the sample be a and b, respectively, at laser wavelength λ . Then the effective pump fluence that absorbed by the sample is given by,

$$\mathcal{F}_{abs} = (1 - a - b) \times \mathcal{F}. \tag{A.3}$$

Assuming all the absorbed photon generates a single electron-hole pair, the excited number density of electrons or holes per unit area is given by,

$$\mathcal{N} = \mathcal{F}_{abs}/E_{p}. \tag{A.4}$$

Here E_p is the energy of a single photon of the pump. The average laser power, P, was measured using powermeter at the sample place, r_{FWHM} measured using a CCD camera at the sample place, a and b measured using the spectrometer. We have estimated the excited number density of each carriers to be 6.6×10^{13} cm⁻² for an average power of 1.2 mJcm⁻².

Appendix B

Calculation of Auger recombination rate

When photoexcited carrier density is much larger than defect density, the rate equation of Auger recombination process for MoS₂ monolayer sample can be written as [36, 37],

$$\frac{dn}{dt} \approx \frac{dp}{dt} \approx -\frac{\alpha \beta n_d^2}{\alpha n_d + \beta n_d} np.$$
 (B.1)

Here, α and β are Auger scattering rates of electrons and holes, n_d is the defect density, and n and p are photoexcited electron and hole densities. Considering same number of electrons and holes are created in the sample after photoexcitation i.e, n = p, above equation can be written as,

$$\frac{dn}{dt} \approx -\frac{\alpha \beta n_d^2}{\alpha n_d + \beta n_d} n^2.$$
 (B.2)

Considering the initial photoexcited carrier density is N_0 and remaining carrier density in the sample is N(t) at any time t, by simple integration, eq.B.2 can be written as,

$$N(t) = \frac{N_0}{1 + tN_0\gamma'},$$
where $\gamma = \frac{\alpha\beta n_d^2}{\alpha n_d + \beta n_d}.$
(B.3)

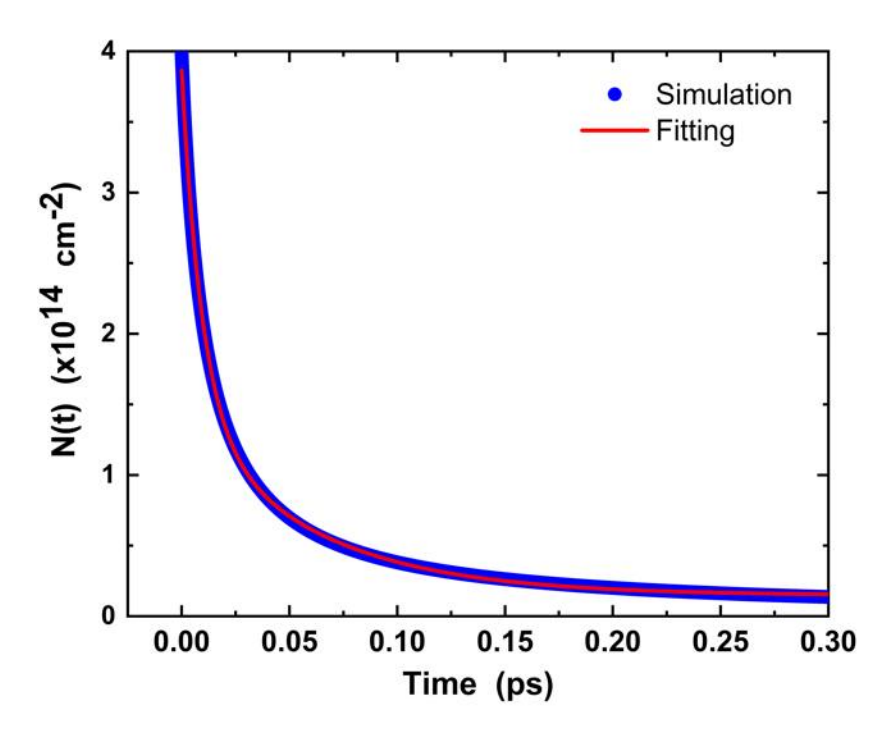


FIGURE B.1: Calculated time dependence of excited carrier density using Eq.B.3. The red line is the fit to the calculated carrier density with double exponential decay function.

Now, by considering the defect density 5×10^{13} cm⁻² and values of α and β which are of the order of 10^{14} cm⁴/s [36, 37], and initial photoexcited carrier density is of the order 10^{14} cm⁻², we calculate the time dependence of carriers in the excited state using Eq.B.3 and is shown in Fig.B.1. To estimate the decay rate, we fit the numerically calculated N(t) with a double exponential decay function,

$$D(t) = Aexp(-t/\tau_A) + Bexp(-t/\tau_B).$$
 (B.4)

The best fit time constants are found to be ~ 10 fs and ~ 60 fs, implying that the Auger processes leads to a faster decay.

- [1] A. K. Geim, "Graphene: status and prospects," *science*, vol. 324, no. 5934, pp. 1530–1534, 2009.
- [2] T. Stauber, N. Peres, and A. Geim, "Optical conductivity of graphene in the visible region of the spectrum," *Phys. Rev. B*, vol. 78, no. 8, p. 085432, 2008.
- [3] K. F. Mak, C. Lee, J. Hone, J. Shan, and T. F. Heinz, "Atomically thin MoS₂: a new direct-gap semiconductor," *Phys. Rev. Lett.*, vol. 105, no. 13, p. 136805, 2010.
- [4] A. Splendiani, L. Sun, Y. Zhang, T. Li, J. Kim, C.-Y. Chim, G. Galli, and F. Wang, "Emerging photoluminescence in monolayer MoS₂," *Nano Lett.*, vol. 10, no. 4, p. 1271, 2010.
- [5] Q. H. Wang, K. Kalantar-Zadeh, A. Kis, J. N. Coleman, and M. S. Strano, "Electronics and optoelectronics of two-dimensional transition metal dichalcogenides," *Nature nanotechnology*, vol. 7, no. 11, pp. 699–712, 2012.
- [6] K. S. Novoselov, A. K. Geim, S. V. Morozov, D.-e. Jiang, Y. Zhang, S. V. Dubonos, I. V. Grigorieva, and A. A. Firsov, "Electric field effect in atomically thin carbon films," *science*, vol. 306, no. 5696, pp. 666–669, 2004.
- [7] N. S. Arul and V. D. Nithya, Two dimensional transition metal dichalcogenides: synthesis, properties, and applications. Springer, 2019.
- [8] M. Chhowalla, H. S. Shin, G. Eda, L.-J. Li, K. P. Loh, and H. Zhang, "The chemistry of two-dimensional layered transition metal dichalcogenide nanosheets," *Nat. Chem.*, vol. 5, no. 4, p. 263, 2013.
- [9] B. Radisavljevic, A. Radenovic, J. Brivio, V. Giacometti, and A. Kis, "Single-layer MoS₂ transistors," *Nat. Nanotechnol.*, vol. 6, no. 3, p. 147, 2011.
- [10] H. Zeng, J. Dai, W. Yao, D. Xiao, and X. Cui, "Valley polarization in MoS₂ monolayers by optical pumping," *Nat. Nanotechnol.*, vol. 7, no. 8, p. 490, 2012.
- [11] J. R. Schaibley, H. Yu, G. Clark, P. Rivera, J. S. Ross, K. L. Seyler, W. Yao, and X. Xu, "Valleytronics in 2D materials," *Nat. Rev. Mater.*, vol. 1, no. 11, pp. 1–15, 2016.

[12] D. Xiao, G.-B. Liu, W. Feng, X. Xu, and W. Yao, "Coupled spin and valley physics in monolayers of MoS₂ and other group-VI dichalcogenides," *Phys. Rev. Lett.*, vol. 108, no. 19, p. 196802, 2012.

- [13] S. Wachter, D. K. Polyushkin, O. Bethge, and T. Mueller, "A microprocessor based on a two-dimensional semiconductor," *Nat. Commun.*, vol. 8, no. 1, pp. 1–6, 2017.
- [14] H. Zhang, S. Lu, J.-l. Zheng, J. Du, S. Wen, D. Tang, and K. Loh, "Molybdenum disulfide (MoS₂) as a broadband saturable absorber for ultra-fast photonics," *Opt. Express*, vol. 22, no. 6, pp. 7249–7260, 2014.
- [15] J. M. Soon and K. P. Loh, "Electrochemical double-layer capacitance of MoS₂ nanowall films," *Electrochem. Solid-State Lett.*, vol. 10, no. 11, p. A250, 2007.
- [16] X. Cao, Y. Shi, W. Shi, X. Rui, Q. Yan, J. Kong, and H. Zhang, "Preparation of MoS₂-coated three-dimensional graphene networks for high-performance anode material in lithium-ion batteries," *small*, vol. 9, no. 20, pp. 3433–3438, 2013.
- [17] Z. Y. Zhu, Y. C. Cheng, and U. Schwingenschlögl, "Giant spin-orbit-induced spin splitting in two-dimensional transition-metal dichalcogenide semiconductors," *Phys. Rev. B*, vol. 84, no. 15, p. 153402, 2011.
- [18] K. Kośmider, J. W. González, and J. Fernández-Rossier, "Large spin splitting in the conduction band of transition metal dichalcogenide monolayers," *Phys. Rev. B*, vol. 88, no. 24, p. 245436, 2013.
- [19] Y. Zhang, H. Li, H. Wang, R. Liu, S.-L. Zhang, and Z.-J. Qiu, "On valence-band splitting in layered MoS₂," *ACS nano*, vol. 9, no. 8, pp. 8514–8519, 2015.
- [20] L. Yuan, T. Wang, T. Zhu, M. Zhou, and L. Huang, "Exciton dynamics, transport, and annihilation in atomically thin two-dimensional semiconductors," *J. Phys. Chem. Lett.*, vol. 8, no. 14, p. 3371, 2017.
- [21] A. Chernikov, T. C. Berkelbach, H. M. Hill, A. Rigosi, Y. Li, O. B. Aslan, D. R. Reichman, M. S. Hybertsen, and T. F. Heinz, "Exciton binding energy and nonhydrogenic rydberg series in monolayer WS₂," *Phys. Rev. Lett.*, vol. 113, no. 7, p. 076802, 2014.
- [22] M. M. Ugeda, A. J. Bradley, S.-F. Shi, H. Felipe, Y. Zhang, D. Y. Qiu, W. Ruan, S.-K. Mo, Z. Hussain, Z.-X. Shen, *et al.*, "Giant bandgap renormalization and excitonic effects in a monolayer transition metal dichalcogenide semiconductor," *Nat. Mater.*, vol. 13, no. 12, p. 1091, 2014.
- [23] Y. Li, A. Chernikov, X. Zhang, A. Rigosi, H. M. Hill, A. M. Van Der Zande, D. A. Chenet, E.-M. Shih, J. Hone, and T. F. Heinz, "Measurement of the optical dielectric function of monolayer transition-metal dichalcogenides: MoS₂, MoSe₂, WS₂, and WSe₂," *Phys. Rev. B*, vol. 90, no. 20, p. 205422, 2014.

[24] D. Y. Qiu, T. Cao, and S. G. Louie, "Nonanalyticity, valley quantum phases, and lightlike exciton dispersion in monolayer transition metal dichalcogenides: Theory and first-principles calculations," *Phys. Rev. Lett.*, vol. 115, no. 17, p. 176801, 2015.

- [25] F. Wu, F. Qu, and A. H. Macdonald, "Exciton band structure of monolayer MoS₂," *Phys. Rev. B*, vol. 91, no. 7, p. 075310, 2015.
- [26] A. Steinhoff, J.-H. Kim, F. Jahnke, M. Rosner, D.-S. Kim, C. Lee, G. H. Han, M. S. Jeong, T. Wehling, and C. Gies, "Efficient excitonic photoluminescence in direct and indirect band gap monolayer MoS₂," *Nano lett.*, vol. 15, no. 10, pp. 6841–6847, 2015.
- [27] S. Cha, J. H. Sung, S. Sim, J. Park, H. Heo, M.-H. Jo, and H. Choi, "1s-intraexcitonic dynamics in monolayer MoS₂ probed by ultrafast mid-infrared spectroscopy," *Nat. Commun.*, vol. 7, no. 1, p. 1, 2016.
- [28] P. Schiettecatte, P. Geiregat, and Z. Hens, "Ultrafast carrier dynamics in few-layer colloidal molybdenum disulfide probed by broadband transient absorption spectroscopy," *J. Phys. Chem. C*, vol. 123, no. 16, p. 10571, 2019.
- [29] K. J. Lee, W. Xin, and C. Guo, "Annihilation mechanism of excitons in a MoS₂ monolayer through direct förster-type energy transfer and multistep diffusion," *Phys. Rev. B*, vol. 101, no. 19, p. 195407, 2020.
- [30] L. Wang, Z. Wang, H.-Y. Wang, G. Grinblat, Y.-L. Huang, D. Wang, X.-H. Ye, X.-B. Li, Q. Bao, A.-S. Wee, *et al.*, "Slow cooling and efficient extraction of C-exciton hot carriers in MoS₂ monolayer," *Nat. Commun.*, vol. 8, no. 1, p. 1, 2017.
- [31] H.-S. Tsai, Y.-H. Huang, P.-C. Tsai, Y.-J. Chen, H. Ahn, S.-Y. Lin, and Y.-J. Lu, "Ultrafast exciton dynamics in scalable monolayer MoS₂ synthesized by metal sulfurization," *ACS omega*, vol. 5, no. 19, p. 10725, 2020.
- [32] D. Sun, Y. Rao, G. A. Reider, G. Chen, Y. You, L. Brézin, A. R. Harutyunyan, and T. F. Heinz, "Observation of rapid exciton–exciton annihilation in monolayer molybdenum disulfide," *Nano Lett.*, vol. 14, no. 10, p. 5625, 2014.
- [33] T. Zhang and J. Wang, "Defect-enhanced exciton-exciton annihilation in monolayer transition metal dichalcogenides at high exciton densities," ACS *Photonics*, 2021.
- [34] C. Zhang, H. Wang, W. Chan, C. Manolatou, and F. Rana, "Absorption of light by excitons and trions in monolayers of metal dichalcogenide MoS₂: Experiments and theory," *Phys. Rev. B*, vol. 89, no. 20, p. 205436, 2014.
- [35] T. C. Berkelbach, M. S. Hybertsen, and D. R. Reichman, "Theory of neutral and charged excitons in monolayer transition metal dichalcogenides," *Phys. Rev. B*, vol. 88, no. 4, p. 045318, 2013.
- [36] H. Wang, C. Zhang, and F. Rana, "Ultrafast dynamics of defect-assisted electron–hole recombination in monolayer MoS₂," *Nano Lett.*, vol. 15, no. 1, p. 339, 2015.

[37] H. Wang, C. Zhang, and F. Rana, "Surface recombination limited lifetimes of photoexcited carriers in few-layer transition metal dichalcogenide MoS₂," *Nano Lett.*, vol. 15, no. 12, p. 8204, 2015.

- [38] Z. Nie, R. Long, L. Sun, C.-C. Huang, J. Zhang, Q. Xiong, D. W. Hewak, Z. Shen, O. V. Prezhdo, and Z.-H. Loh, "Ultrafast carrier thermalization and cooling dynamics in few-layer MoS₂," *ACS nano*, vol. 8, no. 10, p. 10931, 2014.
- [39] Z. Nie, R. Long, J. S. Teguh, C.-C. Huang, D. W. Hewak, E. K. Yeow, Z. Shen, O. V. Prezhdo, and Z.-H. Loh, "Ultrafast electron and hole relaxation pathways in few-layer MoS₂," *J. Phys. Chem. C*, vol. 119, no. 35, p. 20698, 2015.
- [40] Z. Chi, H. Chen, Q. Zhao, and Y.-X. Weng, "Observation of the hot-phonon effect in monolayer MoS₂," *Nanotechnology*, vol. 31, no. 23, p. 235712, 2020.
- [41] K. Yu, J. Wang, J. Chen, and G. P. Wang, "Inhomogeneous photocarrier dynamics and transport in monolayer MoS₂ by ultrafast microscopy," *Nanotechnology*, vol. 30, no. 48, p. 485701, 2019.
- [42] F. Ceballos, Q. Cui, M. Z. Bellus, and H. Zhao, "Exciton formation in monolayer transition metal dichalcogenides," *Nanoscale*, vol. 8, no. 22, p. 11681, 2016.
- [43] G. Zhao, J. Hou, Y. Wu, J. He, and X. Hao, "Preparation of 2D MoS₂/graphene heterostructure through a monolayer intercalation method and its application as an optical modulator in pulsed laser generation," *Adv. Opt. Mater.*, vol. 3, no. 7, p. 937, 2015.
- [44] C. Trovatello, A. Marini, X. Xu, C. Lee, F. Liu, N. Curreli, C. Manzoni, S. D. Conte, K. Yao, A. Ciattoni, *et al.*, "Broadband optical parametric amplification by two-dimensional semiconductors," *arXiv* preprint *arXiv*:1912.10466, 2019.
- [45] S. Butun, S. Tongay, and K. Aydin, "Enhanced light emission from large-area monolayer MoS₂ using plasmonic nanodisc arrays," *Nano Lett.*, vol. 15, no. 4, p. 2700, 2015.
- [46] Y. H. Zhou, H. N. An, C. Gao, Z. Q. Zheng, and B. Wang, "Uv–vis-nir photodetector based on monolayer MoS₂," *Mater. Lett.*, vol. 237, p. 298, 2019.
- [47] D. P. Khatua, S. Gurung, A. Singh, S. Khan, T. K. Sharma, and J. Jayabalan, "Filtering noise in time and frequency domain for ultrafast pump–probe performed using low repetition rate lasers," *Rev. Sci. Instrum.*, vol. 91, no. 10, p. 103901, 2020.
- [48] D. P. Khatua, A. Singh, S. Gurung, and J. Jayabalan, "Excitation density dependent carrier dynamics in a monolayer MoS₂: Exciton dissociation, formation and bottlenecking," *Micro and Nanostructures*, p. 207205, 2022.
- [49] D. P. Khatua, A. Singh, S. Gurung, S. Khan, and J. Jayabalan, "Ultrafast carrier dynamics in a monolayer MoS₂ at carrier densities well above mott density," *J. Phys. Condens. Matter*, vol. 34, no. 15, p. 155401, 2022.

[50] T. Völzer, F. Fennel, T. Korn, and S. Lochbrunner, "Fluence-dependent dynamics of localized excited species in monolayer versus bulk MoS₂," *Phys. Rev. B*, vol. 103, no. 4, p. 045423, 2021.

- [51] W. Wang, N. Sui, X. Chi, Z. Kang, Q. Zhou, L. Li, H. Zhang, J. Gao, and Y. Wang, "Investigation of hot carrier cooling dynamics in monolayer MoS₂," *J. Phys. Chem. Lett.*, vol. 12, no. 2, p. 861, 2021.
- [52] T. Borzda, C. Gadermaier, N. Vujicic, P. Topolovsek, M. Borovsak, T. Mertelj, D. Viola, C. Manzoni, E. A. Pogna, D. Brida, et al., "Charge photogeneration in few-layer MoS₂," Adv. Funct. Mater., vol. 25, no. 22, p. 3351, 2015.
- [53] C. Pan, L. Jiang, J. Sun, Q. Wang, F. Wang, K. Wang, Y. Lu, Y. Wang, L. Qu, and T. Cui, "Ultrafast optical response and ablation mechanisms of molybdenum disulfide under intense femtosecond laser irradiation," *Light Sci. Appl.*, vol. 9, no. 1, p. 1, 2020.
- [54] M. Seo, H. Yamaguchi, A. D. Mohite, S. Boubanga-Tombet, J.-C. Blancon, S. Najmaei, P. M. Ajayan, J. Lou, A. J. Taylor, and R. P. Prasankumar, "Ultrafast optical microscopy of single monolayer molybdenum disulfide flakes," *Sci. Rep.*, vol. 6, no. 1, p. 1, 2016.
- [55] F. Liu, M. E. Ziffer, K. R. Hansen, J. Wang, and X. Zhu, "Direct determination of band-gap renormalization in the photoexcited monolayer MoS₂," *Phys. Rev. Lett.*, vol. 122, no. 24, p. 246803, 2019.
- [56] D. Yadav, M. Trushin, and F. Pauly, "Thermalization of photoexcited carriers in two-dimensional transition metal dichalcogenides and internal quantum efficiency of van der waals heterostructures," *Phys. Rev. Res.*, vol. 2, no. 4, p. 043051, 2020.
- [57] Y. Gao, C. S. Sandeep, J. M. Schins, A. J. Houtepen, and L. D. Siebbeles, "Disorder strongly enhances auger recombination in conductive quantum-dot solids," *Nat. Commun.*, vol. 4, no. 1, pp. 1–7, 2013.
- [58] K. Wei, X. Zheng, X. Cheng, C. Shen, and T. Jiang, "Observation of ultra-fast exciton–exciton annihilation in CsPbBr₃ quantum dots," *Adv. Opt. Mater.*, vol. 4, no. 12, pp. 1993–1997, 2016.
- [59] G. Soavi, S. Dal Conte, C. Manzoni, D. Viola, A. Narita, Y. Hu, X. Feng, U. Hohenester, E. Molinari, D. Prezzi, *et al.*, "Exciton–exciton annihilation and biexciton stimulated emission in graphene nanoribbons," *Nat. Commun.*, vol. 7, no. 1, pp. 1–7, 2016.
- [60] T.-Q. Nguyen, I. B. Martini, J. Liu, and B. J. Schwartz, "Controlling interchain interactions in conjugated polymers: the effects of chain morphology on exciton- exciton annihilation and aggregation in MEH-PPV films," *J. Phys. Chem. B*, vol. 104, no. 2, pp. 237–255, 2000.

[61] E. Engel, K. Leo, and M. Hoffmann, "Ultrafast relaxation and exciton–exciton annihilation in PTCDA thin films at high excitation densities," *Chem. Phys.*, vol. 325, no. 1, pp. 170–177, 2006.

- [62] Y.-Z. Ma, L. Valkunas, S. L. Dexheimer, S. M. Bachilo, and G. R. Fleming, "Femtosecond spectroscopy of optical excitations in single-walled carbon nanotubes: Evidence for exciton-exciton annihilation," *Phys. Rev. Lett.*, vol. 94, no. 15, p. 157402, 2005.
- [63] H. Wang, J. H. Strait, C. Zhang, W. Chan, C. Manolatou, S. Tiwari, and F. Rana, "Fast exciton annihilation by capture of electrons or holes by defects via auger scattering in monolayer metal dichalcogenides," *Phys. Rev. B*, vol. 91, no. 16, p. 165411, 2015.
- [64] L. Yuan and L. Huang, "Exciton dynamics and annihilation in WS₂ 2D semiconductors," *Nanoscale*, vol. 7, no. 16, pp. 7402–7408, 2015.
- [65] P. D. Cunningham, K. M. McCreary, and B. T. Jonker, "Auger recombination in chemical vapor deposition-grown monolayer WS₂," *J. Phys. Chem. Lett.*, vol. 7, no. 24, pp. 5242–5246, 2016.
- [66] K.-Q. Lin, P. E. Faria Junior, J. M. Bauer, B. Peng, B. Monserrat, M. Gmitra, J. Fabian, S. Bange, and J. M. Lupton, "Twist-angle engineering of excitonic quantum interference and optical nonlinearities in stacked 2D semiconductors," *Nat. Commun*, vol. 12, no. 1, pp. 1–7, 2021.
- [67] X. He, M. Chebl, and D.-S. Yang, "Cross-examination of ultrafast structural, interfacial, and carrier dynamics of supported monolayer MoS₂," *Nano Lett.*, vol. 20, no. 3, p. 2026, 2020.
- [68] B. R. Bennett, R. A. Soref, and J. A. Del Alamo, "Carrier-induced change in refractive index of InP, GaAs and InGaAsP," *IEEE J. Quantum Electron.*, vol. 26, no. 1, pp. 113–122, 1990.
- [69] E. A. Pogna, M. Marsili, D. De Fazio, S. Dal Conte, C. Manzoni, D. Sangalli, D. Yoon, A. Lombardo, A. C. Ferrari, A. Marini, *et al.*, "Photo-induced bandgap renormalization governs the ultrafast response of single-layer MoS₂," *ACS nano*, vol. 10, no. 1, p. 1182, 2016.
- [70] S. K. Bera, M. Shrivastava, K. Bramhachari, H. Zhang, A. K. Poonia, D. Mandal, E. M. Miller, M. C. Beard, A. Agarwal, and K. Adarsh, "Atom like interaction and optically tunable giant band-gap renormalization in large-area atomically thin MoS₂," *Phys. Rev. B*, vol. 104, no. 20, p. L201404, 2021.
- [71] D. Tsokkou, X. Yu, K. Sivula, and N. Banerji, "The role of excitons and free charges in the excited-state dynamics of solution-processed few-layer MoS₂ nanoflakes," *J. Phys. Chem. C*, vol. 120, no. 40, pp. 23286–23292, 2016.
- [72] F. Katsch, M. Selig, and A. Knorr, "Exciton-scattering-induced dephasing in two-dimensional semiconductors," *Phys. Rev. Lett.*, vol. 124, no. 25, p. 257402, 2020.

[73] F. Cadiz, E. Courtade, C. Robert, G. Wang, Y. Shen, H. Cai, T. Taniguchi, K. Watanabe, H. Carrere, D. Lagarde, *et al.*, "Excitonic linewidth approaching the homogeneous limit in MoS₂-based van der waals heterostructures," *Phys. Rev. X*, vol. 7, no. 2, p. 021026, 2017.

- [74] G. Eda and S. A. Maier, "Two-dimensional crystals: managing light for opto-electronics," *ACS nano*, vol. 7, no. 7, pp. 5660–5665, 2013.
- [75] K. Kaasbjerg, K. S. Thygesen, and K. W. Jacobsen, "Phonon-limited mobility in n-type single-layer MoS₂ from first principles," *Phys. Rev. B*, vol. 85, no. 11, p. 115317, 2012.
- [76] X. Xu, W. Yao, D. Xiao, and T. F. Heinz, "Spin and pseudospins in layered transition metal dichalcogenides," *Nat. Phys*, vol. 10, no. 5, pp. 343–350, 2014.
- [77] K. Alam and R. K. Lake, "Monolayer MoS₂ transistors beyond the technology road map," *IEEE Trans. Electron Devices*, vol. 59, no. 12, pp. 3250–3254, 2012.
- [78] M.-L. Tsai, S.-H. Su, J.-K. Chang, D.-S. Tsai, C.-H. Chen, C.-I. Wu, L.-J. Li, L.-J. Chen, and J.-H. He, "Monolayer MoS₂ heterojunction solar cells," *ACS nano*, vol. 8, no. 8, pp. 8317–8322, 2014.
- [79] M. Bernardi, M. Palummo, and J. C. Grossman, "Extraordinary sunlight absorption and one nanometer thick photovoltaics using two-dimensional monolayer materials," *Nano Lett.*, vol. 13, no. 8, pp. 3664–3670, 2013.
- [80] S. Zhu, L. Gong, J. Xie, Z. Gu, and Y. Zhao, "Design, synthesis, and surface modification of materials based on transition-metal dichalcogenides for biomedical applications," *Small Methods*, vol. 1, no. 12, p. 1700220, 2017.
- [81] F. Yin, B. Gu, Y. Lin, N. Panwar, S. C. Tjin, J. Qu, S. P. Lau, and K.-T. Yong, "Functionalized 2D nanomaterials for gene delivery applications," *Co-ord. Chem. Rev.*, vol. 347, pp. 77–97, 2017.
- [82] F. Cao, E. Ju, Y. Zhang, Z. Wang, C. Liu, W. Li, Y. Huang, K. Dong, J. Ren, and X. Qu, "An efficient and benign antimicrobial depot based on silver-infused MoS₂," *ACS nano*, vol. 11, no. 5, pp. 4651–4659, 2017.
- [83] J. Shi, J. Lyu, F. Tian, and M. Yang, "A fluorescence turn-on biosensor based on graphene quantum dots (gqds) and molybdenum disulfide (MoS₂) nanosheets for epithelial cell adhesion molecule (epcam) detection," *Biosens. Bioelectron.*, vol. 93, pp. 182–188, 2017.
- [84] X. Liu, L. Li, Y. Wei, Y. Zheng, Q. Xiao, and B. Feng, "Facile synthesis of boronand nitride-doped MoS₂ nanosheets as fluorescent probes for the ultrafast, sensitive, and label-free detection of Hg²⁺," *Analyst*, vol. 140, no. 13, pp. 4654–4661, 2015.
- [85] K. F. Mak and J. Shan, "Photonics and optoelectronics of 2D semiconductor transition metal dichalcogenides," *Nat. Photonics*, vol. 10, no. 4, p. 216, 2016.

[86] O. Lopez-Sanchez, D. Lembke, M. Kayci, A. Radenovic, and A. Kis, "Ultrasensitive photodetectors based on monolayer MoS₂," *Nat. Nanotechnol.*, vol. 8, no. 7, p. 497, 2013.

- [87] S. Wang, H. Yu, H. Zhang, A. Wang, M. Zhao, Y. Chen, L. Mei, and J. Wang, "Broadband few-layer MoS₂ saturable absorbers," *Adv. Mater.*, vol. 26, no. 21, pp. 3538–3544, 2014.
- [88] R. Ganatra and Q. Zhang, "Few-layer MoS₂: a promising layered semiconductor," *ACS nano*, vol. 8, no. 5, pp. 4074–4099, 2014.
- [89] Y.-H. Lee, X.-Q. Zhang, W. Zhang, M.-T. Chang, C.-T. Lin, K.-D. Chang, Y.-C. Yu, J. T.-W. Wang, C.-S. Chang, L.-J. Li, et al., "Synthesis of large-area MoS₂ atomic layers with chemical vapor deposition," *Adv. Mater.*, vol. 24, no. 17, pp. 2320–2325, 2012.
- [90] K.-K. Liu, W. Zhang, Y.-H. Lee, Y.-C. Lin, M.-T. Chang, C.-Y. Su, C.-S. Chang, H. Li, Y. Shi, H. Zhang, *et al.*, "Growth of large-area and highly crystalline MoS₂ thin layers on insulating substrates," *Nano Lett.*, vol. 12, no. 3, pp. 1538–1544, 2012.
- [91] S. Wu, C. Huang, G. Aivazian, J. S. Ross, D. H. Cobden, and X. Xu, "Vaporsolid growth of high optical quality MoS₂ monolayers with near-unity valley polarization," *ACS nano*, vol. 7, no. 3, pp. 2768–2772, 2013.
- [92] "https://2dlayer.com." Procured from 2DLayer, 2 Davis Drive, Durham, NC 27709 USA.
- [93] T. Han, H. Liu, S. Wang, S. Chen, W. Li, X. Yang, M. Cai, and K. Yang, "Probing the optical properties of MoS₂ on SiO₂/Si and sapphire substrates," *Nanomaterials*, vol. 9, no. 5, p. 740, 2019.
- [94] D. H. Auston, D. Bradley, A. Campillo, K. Eisenthal, E. Ippen, D. v. der Linde, and C. Shank, *Ultrashort light pulses: Picosecond techniques and applications*, vol. 18. Springer Science & Business Media, 2013.
- [95] R. L. Sutherland, Handbook of nonlinear optics. CRC press, 2003.
- [96] J. Shah, *Ultrafast spectroscopy of semiconductors and semiconductor nanostructures*, vol. 115. Springer Science & Business Media, 2013.
- [97] F. Rossi and T. Kuhn, "Theory of ultrafast phenomena in photoexcited semi-conductors," *Rev. Mod. Phys.*, vol. 74, no. 3, p. 895, 2002.
- [98] G. C. Cho, W. Kütt, and H. Kurz, "Subpicosecond time-resolved coherent-phonon oscillations in gaas," *Phys. Rev. Lett.*, vol. 65, pp. 764–766, Aug 1990.
- [99] M. Rosker, F. Wise, and C. Tang, "Femtosecond relaxation dynamics of large molecules," *Phys. Rev. Lett.*, vol. 57, no. 3, p. 321, 1986.

[100] D. M. Jonas, M. J. Lang, Y. Nagasawa, T. Joo, and G. R. Fleming, "Pump-probe polarization anisotropy study of femtosecond energy transfer within the photosynthetic reaction center of rhodobacter sphaeroides R26," *J. Phys. Chem.*, vol. 100, no. 30, pp. 12660–12673, 1996.

- [101] R. J. Stevens, A. N. Smith, and P. M. Norris, "Signal analysis and characterization of experimental setup for the transient thermoreflectance technique," *Rev. Sci. Instrum.*, vol. 77, no. 8, p. 084901, 2006.
- [102] I. Flinn, "Extent of the 1/f noise spectrum," *Nature*, vol. 219, no. 5161, pp. 1356–1357, 1968.
- [103] E. Milotti, "1/f noise: a pedagogical review," arXiv preprint physics/0204033, 2002.
- [104] P. P. Regtien and E. Dertien, Sensors for mechatronics. Elsevier, 2018.
- [105] K. Neelakantan, S. Dattagupta, and K. Rajappan, "Signal to noise enhancement of lock-in amplifiers," *Rev. Sci. Instrum.*, vol. 51, p. 251, 1980.
- [106] M. L. Meade, Lock-in amplifiers: principles and applications. No. 1, Mike Meade, 1983.
- [107] D. Van Baak and G. Herold, "Response of a lock-in amplifier to noise," *Am. J. Phys*, vol. 82, no. 8, pp. 785–797, 2014.
- [108] P. M. Norris, A. P. Caffrey, R. J. Stevens, J. M. Klopf, J. T. McLeskey Jr, and A. N. Smith, "Femtosecond pump–probe nondestructive examination of materials," *Rev. Sci. Instrum.*, vol. 74, no. 1, pp. 400–406, 2003.
- [109] J. Jayabalan, A. Singh, R. Chari, S. Khan, H. Srivastava, and S. Oak, "Transient absorption and higher-order nonlinearities in silver nanoplatelets," *Appl. Phys. Lett.*, vol. 94, no. 18, p. 181902, 2009.
- [110] G. B. Arfken and H. J. Weber, "Mathematical methods for physicists," 1999.
- [111] S. Khan, J. Jayabalan, A. Singh, R. Chari, S. Pal, S. Porwal, T. Sharma, and S. Oak, "Coherent oscillations of holes in GaAsP/AlGaAs surface quantum well.," *Pramana: Journal of Physics*, vol. 82, no. 2, 2014.
- [112] O. L. Muskens, N. Del Fatti, and F. Vallée, "Femtosecond response of a single metal nanoparticle," *Nano Lett.*, vol. 6, no. 3, pp. 552–556, 2006.
- [113] A. Singh, S. Gurung, R. Chari, and J. Jayabalan, "Counting the electrons hopping in ultrafast time scales in an Ag–CdTe hybrid nanostructure," *J. Phys. Chem. C*, vol. 123, no. 47, pp. 28584–28592, 2019.
- [114] C. Gonçalves, A. Silva, D. Navas, M. Miranda, F. Silva, H. Crespo, and D. Schmool, "A dual-colour architecture for pump-probe spectroscopy of ultrafast magnetization dynamics in the sub-10-femtosecond range," *Sci. Rep.*, vol. 6, p. 22872, 2016.

[115] E. J. Sie, A. Steinhoff, C. Gies, C. H. Lui, Q. Ma, M. Rosner, G. Schönhoff, F. Jahnke, T. O. Wehling, Y.-H. Lee, et al., "Observation of exciton redshift–blueshift crossover in monolayer WS₂," Nano Lett., vol. 17, no. 7, pp. 4210–4216, 2017.

- [116] A. Chernikov, C. Ruppert, H. M. Hill, A. F. Rigosi, and T. F. Heinz, "Population inversion and giant bandgap renormalization in atomically thin WS₂ layers," *Nat. Photonics*, vol. 9, no. 7, p. 466, 2015.
- [117] S. Sim, J. Park, J.-G. Song, C. In, Y.-S. Lee, H. Kim, and H. Choi, "Exciton dynamics in atomically thin MoS₂: interexcitonic interaction and broadening kinetics," *Phys. Rev. B*, vol. 88, no. 7, p. 075434, 2013.
- [118] H. Qiu, T. Xu, Z. Wang, W. Ren, H. Nan, Z. Ni, Q. Chen, S. Yuan, F. Miao, F. Song, *et al.*, "Hopping transport through defect-induced localized states in molybdenum disulphide," *Nat. Commun.*, vol. 4, no. 1, p. 1, 2013.
- [119] W. Zhou, X. Zou, S. Najmaei, Z. Liu, Y. Shi, J. Kong, J. Lou, P. M. Ajayan, B. I. Yakobson, and J.-C. Idrobo, "Intrinsic structural defects in monolayer molybdenum disulfide," *Nano Lett.*, vol. 13, no. 6, p. 2615, 2013.
- [120] J. Hong, Z. Hu, M. Probert, K. Li, D. Lv, X. Yang, L. Gu, N. Mao, Q. Feng, L. Xie, et al., "Exploring atomic defects in molybdenum disulphide monolayers," *Nat. Commun.*, vol. 6, no. 1, p. 1, 2015.
- [121] A. Brasington, D. Golla, A. Dave, B. Chen, S. Tongay, J. Schaibley, B. J. LeRoy, and A. Sandhu, "Role of defects and phonons in bandgap dynamics of monolayer WS₂ at high carrier densities," *J. Phys. Mater.*, vol. 4, no. 1, p. 015005, 2020.
- [122] A. O. Slobodeniuk and D. M. Basko, "Exciton-phonon relaxation bottleneck and radiative decay of thermal exciton reservoir in two-dimensional materials," *Phys. Rev. B*, vol. 94, no. 20, p. 205423, 2016.
- [123] K. Lee, J. Li, L. Cheng, J. Wang, D. Kumar, Q. Wang, M. Chen, Y. Wu, G. Eda, E. E. Chia, *et al.*, "Sub-picosecond carrier dynamics induced by efficient charge transfer in MoTe₂/WTe₂ van der waals heterostructures," *ACS nano*, vol. 13, no. 8, pp. 9587–9594, 2019.
- [124] Y. Li, J. Shi, H. Chen, Y. Mi, W. Du, X. Sui, C. Jiang, W. Liu, H. Xu, and X. Liu, "Slow cooling of high-energy C excitons is limited by intervalley-transfer in monolayer MoS₂," *Laser Photonics Rev.*, vol. 13, no. 4, p. 1800270, 2019.
- [125] I. N. Yakovkin, "Dirac cones in graphene, interlayer interaction in layered materials, and the band gap in MoS₂," *Crystals*, vol. 6, no. 11, p. 143, 2016.
- [126] B. Evans and P. Young, "Exciton spectra in thin crystals: the diamagnetic effect," *Proc. Phys. Soc.* (1958-1967), vol. 91, no. 2, p. 475, 1967.
- [127] R. Wallauer, J. Reimann, N. Armbrust, J. Güdde, and U. Höfer, "Intervalley scattering in MoS₂ imaged by two-photon photoemission with a high-harmonic probe," *Appl. Phys. Lett.*, vol. 109, no. 16, p. 162102, 2016.

- [128] N. Kumar, J. He, D. He, Y. Wang, and H. Zhao, "Charge carrier dynamics in bulk MoS₂ crystal studied by transient absorption microscopy," *J. Appl. Phys.*, vol. 113, no. 13, p. 133702, 2013.
- [129] A. Castellanos-Gomez, J. Quereda, H. P. van der Meulen, N. Agraït, and G. Rubio-Bollinger, "Spatially resolved optical absorption spectroscopy of single-and few-layer MoS₂ by hyperspectral imaging," *Nanotechnology*, vol. 27, no. 11, p. 115705, 2016.
- [130] S. Sim, H.-S. Shin, D. Lee, J. Lee, M. Cha, K. Lee, and H. Choi, "Opposite behavior of ultrafast dynamics of exciton shift and linewidth broadening in bilayer ReS₂," *Phys. Rev. B*, vol. 103, no. 1, p. 014309, 2021.